

---

LINK BETWEEN PHOTOASSOCIATION AND  
OPTICAL FESHBACH RESONANCES  
THROUGH THE EXAMPLE OF CALCIUM

---

Von der QUEST-Leibniz-Forschungsschule der  
Gottfried Wilhelm Leibniz Universität Hannover  
zur Erlangung des Grades

Doktor der Naturwissenschaften  
Dr. rer. nat.  
genehmigte Dissertation  
von

Dipl.-Phys. Max Georg Günther Kahmann  
geboren am 6. September 1982 in Böblingen

Tag der Promotion: 04. 07. 2014

Referenten: Prof. Dr. Eberhard Tiemann, Prof. Dr. Fritz Riehle

# Zusammenfassung

Im Zuge dieser Arbeit werden die ersten Photoassoziations-Messungen der gebundenen Vibrationsresonanzen zur Modellierung des schmalbandigen Systems  $^1S_0 + ^3P_1$  in Calcium präsentiert. In einem Energiebereich von bis zu  $25 \text{ GHz} \cdot h$  unterhalb der atomaren Asymptote, wurden sechs Photoassoziationsresonanzen in den beiden, zur atomaren  $^3P_1 + ^1S_0$  Asymptote gehörenden, Molekülpotentialen  $\Omega = 0$  und  $\Omega = 1$  spektroskopiert. In beiden angeregten Zuständen  $\Omega = 0$  und  $\Omega = 1$  wurden jeweils zusätzlich die Zeemanaufspaltungen gemessen.

Es wurde ein theoretisches Modell entwickelt, das für beide Molekülpotentiale, neben den Bindungsenergien, die von der Potentialform für grosse Kernabstände abhängt, auch die Zeemanaufspaltung, die von dem Kopplungsverhalten der Drehimpulse abhängt, beschreiben kann. Dieses Modell dient dazu, die entsprechenden Molekülpotentialparameter zu bestimmen und erlaubt Vorhersagen für die Manipulation der atomaren Streulänge durch optische Feshbachresonanzen mit geringen Atomverlusten. Dafür wird im dritten Kapitel ein Modell vorgestellt und experimentell durch Multiphotonenspektroskopie getestet, welches auf Basis der gewonnenen Molekülparameter Vorhersagen für die Streulänge und die zu erwartenden Verluste machen. Da sich die beobachteten Linienbreiten der Resonanzspektren bei hohen Lichtintensitäten nicht durch die bestehenden Modelle erklären lassen, wird im vierten Kapitel eine ausführliche Linienbreitendiskussion über alle Effekte, die in einer Verbreiterung der zu erwartenden Spektren enden können, geführt. Zusätzlich wurden die Anregungsraten experimentell analysiert, was Rückschlüsse auf die Ergebnisse des *coupled channel* Modells, sowie auf die existierenden theoretischen Modelle, zur Beschreibung der Photoassoziation erlaubt. Derart wurden die Vorhersagen, des in dieser Arbeit entwickelten *coupled channel* Modells, bestätigt. Ferner wurde das existierende Photoassoziationsmodell für niedrige Intensitäten bestätigt. Für hohe Intensitäten jedoch wurden erhebliche Abweichungen festgestellt und die möglichen Erweiterungen der Modelle diskutiert.



# Abstract

In this thesis, the first photoassociation (PA) measurements to model the narrow-line system  $^1S_0 + ^3P_1$  are presented. Calcium atoms were optically trapped and cooled. Precisely tunable laser light was produced for a high accurate spectroscopy. The light was irradiated for typically one second to the trapped atoms, and the trap losses were observed from absorption images of the atomic cloud. In an energy range of up to  $25 \text{ GHz} \cdot h$  below the asymptote, we have observed six photoassociation resonances in the two molecular potentials  $\Omega = 0$  and  $\Omega = 1$  corresponding to the  $^3P_1 + ^1S_0$  asymptote. In both the  $\Omega = 0$  and  $1$  excited states we measured the Zeeman splittings.

A theoretical model was developed in order to describe both, the Zeeman splitting, given by the coupling behavior of the angular momenta, and the energy of the bound molecular states in both potentials, given by the potential shapes for long distances of the nuclei. The data allows, to improve our knowledge of the molecular parameters and the dispersion coefficients. This allows predictions for the use of low-loss optical Feshbach resonances, to manipulate the atomic scattering length. Therefore, in the third chapter a model for optical Feshbach resonances is presented, and the theoretical predictions based on the derived molecular potential values are presented and tested experimentally by multi-photon spectroscopy. Since the observed line shapes for high intensities cannot be explained by the theoretical model in the fourth chapter, a detailed line shape discussion follows, including the experimental investigation of the excitation rates, in order to test the coupled channel model presented in chapter two, as well as the existing PA models. The predictions of the coupled channel model have been confirmed, also the PA model for low intensities. For high intensities however, the PA model was not capable and a first discussion for a necessary enhancement is given.



## **Keywords - Schlüsselworte**

- Ultra-cold atoms - Ultrakalte Atome
- Photoassociation spectroscopy - Photoassoziationsspektroskopie
- Optical Feshbach resonances - Optische Feshbachresonanzen
- Scattering length - Streulänge
- Optical length - Optische Länge
- Cold molecules Kalte Moleküle
- Multi-photon photoassociation - Multiphotonenphotoassoziation
- Bragg spectroscopy - Bragg-spektroskopie
- Magnetic storage - Magnetisches Speichern
- Gallagher–Pritchard losses - Gallagher-Pritchard-Verluste
- Calcium - Kalzium



# Contents

<b>1</b>	<b>Introduction</b>	<b>1</b>
<b>2</b>	<b>Photoassociation experiment to determine molecular potentials</b>	<b>11</b>
2.1	Light assisted generation of molecules at the intercombination line . . . . .	13
2.2	Experimental realization . . . . .	14
2.3	Theoretical predictions for the binding energies . . . . .	26
2.4	Experimental results for PA binding energy measurements . . . . .	27
2.5	Comparison of the derived binding energies to the predictions . . . . .	39
2.6	Angular momentum coupling in the Ca molecule . . . . .	39
2.7	Hund's coupling cases . . . . .	40
2.8	Theoretical predictions for the $g$ -factors and molecular state identification . . . . .	42
2.9	Experimental results of the Zeeman splitting measurements . . . . .	44
2.10	Estimated uncertainty of the $g$ -factors . . . . .	47
2.11	Close coupled channel model . . . . .	50
<b>3</b>	<b>Modification of scattering length by optical Feshbach resonances theory and experimental test</b>	<b>57</b>
3.1	Scattering length . . . . .	57
3.2	Optical Feshbach resonances . . . . .	59
3.3	Theoretical model for the influence of light . . . . .	61
3.4	Optical length as indicator for OFR capability . . . . .	63
3.5	Theoretical prediction for the optical length based on the molecular potential . . . . .	63
3.6	Suitability of Ca for optical Feshbach resonances compared to other elements . . . . .	66
3.7	Test of scattering length modification . . . . .	70

<b>4</b>	<b>High intensity photoassociation</b>	<b>79</b>
4.1	Experimental line shape investigation for high PA intensities . . . . .	79
4.2	Line width discussion . . . . .	84
4.3	Experimentally observed PA-loss rate . . . . .	91
4.4	Test of the theoretical model . . . . .	97
<b>5</b>	<b>Conclusions and outlook</b>	<b>103</b>
<b>A</b>	<b>Enhanced magnetical trapping of Calcium</b>	<b>109</b>
A.1	Experimental setup . . . . .	110
A.2	Storage in the $^3P_2$ state . . . . .	110
A.3	Modeling the loading . . . . .	113
A.4	Lifetime of the magnetic trap . . . . .	115
A.5	MOT improvements . . . . .	117
A.6	Conclusion . . . . .	118
<b>B</b>	<b>Multi color spectroscopy</b>	<b>119</b>
B.1	Two photon photoassociation spectroscopy . . . . .	119
B.2	Bragg spectroscopy . . . . .	121

# Chapter 1

## Introduction

In my personal opinion, atomic physics is the most interesting of sciences from the point of view of understanding the surrounding nature, while light is in my eyes the most important source of information. The investigation of these two exciting topics already started thousands of years ago. Modification of the scattering behavior of atoms by light, presented in this work, to me, is the perfect combination of these two exciting fields of science and the result of hundreds of years of scientific investigations. In this chapter, I present as my motivation for this thesis work a personal selection of historic milestones in these two fields as well as their synergy, leading to the investigations presented in this work. The following historical presentation is mostly follows the works in [3, 4].

From the very beginning, humanity endeavored to explain and understand the phenomena of nature, which surrounded them. Examining nature, one recognizes, that there are a lot of systematic repetitions: beech trees in the Black forest for example are indistinguishable from beech trees of the same type in Berlin [3]. This led forward thinkers consider systematic patterns in matter. Could there be at least a



Figure 1.1: Leucippus, an ancient Greek philosopher [1]. Figure taken from [2].

common denominator, which this system of repetitions is based on? Is it possible, that from a certain point on it does not make sense to continue dividing material? In his book "Elementarteilchen, Bausteine der Materie" [3] Harald Fritsch gives a useful and interesting metaphor, by comparing matter with a library. In essence, all libraries are composed the same way. Libraries consist mainly of a huge number of books. Each single book consists of thousands of words. Each word in the English language is built up by 26 letters. Nowadays, since the beginning of the digital information age, it is more common to write a book on a computer. This means that every single letter can be described in binary code using the elements 0 and 1; therefore we have reached a fundamental limit of dividing. It is just not possible to reduce something beyond a binary system. The question is: Is there such a fundamental barrier in matter as well?

The first known humans, that are known to have debated this problem, were the ancient philosopher Democritus and his teacher Leucippus<sup>1</sup> (figure 1.1) in the 5th century B.C. They postulated, based on the idea of an "empty space", developed by the philosopher Parmenides, that all of nature consists of very small, impartible units called atoms (Greek *ατομος*, *átomos*, which means "impartible" or "the smallest indivisible particle of matter").

In this so called "golden era" of notable accumulation of philosophical developments around 500 B.C., in India a pretty similar idea of atomism occurred, developed in the philosophy of Mundaka-Upanischad, without influence from their European counterparts [5].

It took western civilization almost two millennia to overcome the dark medieval times, characterized by religious fanaticism, to accept these ancient ideas in an age of enlightenment. In the 17th century, the philosophic idea of atomism appeared again and was enhanced by Gottfried Wilhelm Leibniz (figure 1.2) for instance, who replaced an empiric point of view by a logic one, in his alternative "Monadology for atomism" [6]. In the same century, Sir Isaac Newton, the founder of theoretical physics [7], came to the conclusion that the interaction between elementary particles defines the coherence of macroscopic bodies.

Today, we know that atoms are neither indestructible nor indivisible. They are composed of a shell, consisting of electrons and a nucleus, which consists of protons and neutrons<sup>2</sup> [8]. These nuclear particles consist of so called quarks and gluons

---

<sup>1</sup>According to some researchers, Leucippus was just a pseudonym for Democritus.

<sup>2</sup>Besides the isotope <sup>1</sup>H, which only consist of a proton and an electron.

[9]. With the apparent proof of the standard model [10] by discovering the so called "God particle" [11] (or "Higgs Boson" [12]) at CERN<sup>3</sup> [13], from today's point of view, the elementary particles of matter, predicted by Democritus and Leukippus, seem to be leptons, quarks and gluons. Nevertheless modern research is even aiming at observing an internal structure of electrons<sup>4</sup>.



Figure 1.2: Gottfried Wilhelm Leibniz was a German mathematician and philosopher. He occupies a prominent place in the history of mathematics and the history of philosophy [14]. The Leibniz university of Hannover is named after him. Figure taken from [2].

we call light. The great minds of the Greek ancient time, such as Pythagoras, Democritus, Empedokles and Aristoteles, who thought about nature also developed theories about the nature of light.

Atoms in the modern nomenclature, are the smallest units, which can exist permanently. Also the statements of Anaxagoras and Democritus seem to be almost prophetic from today's point of view. The interactions of the atomic shells result in the combination of atoms to molecules or solid matter and bring with it the systematic richness of species of matter. Their geometry decisively matters: what would happen, if water, the primary substance of life, for example, would not have an angle of 104 degree in the axis between the nuclei of the two hydrogen atoms and the oxygen atom, leading to a non-polar molecular structure? Life, as we know, would simply not exist.

For the development of all this systematic understanding of nature, information about it, is indispensable. Humans have five senses to acquire information about the surrounding world. One of these senses, probably the most important to explore the surrounding world, is sight, using a medium

<sup>3</sup>Conseil Européen pour la Recherche Nucléaire

<sup>4</sup>private communication: Eric Cornell, JILA

During the dark medieval times, there were no significant further developments in the field of optics and some knowledge was even lost in Europe. But there have been some developments in the Arabic world worth noting; especially the notations of Alhanzen who lived in the 11th century.

In the 17th century new technologies in the field of optical instruments occur, such as g.e. the refracting telescope, credited to three individuals, Hans Lippershey, Zacharias Janssen and Jacob Metius and further developed by Galileo Galilei.

An enormous step for the theoretical description of light was taken in the 19th century. The wave theory of light by Huygens and the new interpretation of a phenomenon called interference, discovered by Thomas Young and modeled by Hermann von Helmholtz (figure 1.3), was combined by Augustin Jean Fresnel. This led him to the well-known formulas, named after him, of the amplitudes of reflected and transmitted light beams.

In parallel to these developments, research into electricity and magnetism made substantial progress. In particular the Faraday effect, named after the brilliant experimental physicist Michael Faraday, was a first experimental indication of an interaction between light and electromagnetism. It was James Clark Maxwell, who was able to make a theoretical prediction of the speed of light by combining the empiric knowledge in these fields [15]. At the end of the century the scientific community believed that an all-embracing theory in physics was almost achieved. In 1874 for example, Philipp von Jolly told Max Planck that "in this science (physics) almost everything is researched and that only a few voids have to be filled"! Physicists of that days, e.g. thought about a so called light ether in which the electro-magnetic waves are propagating.

However, one experiment at the end of the century, which is known today as the Michelson–Morley experiment disproved the existence of the so called light ether, and subsequently this hypothesis disappeared [16]. Right at the beginning of the 20th century, the consequences of these results became more and more apparent. It was Jules Henri Poincaré in 1900 and in 1905 Albert Einstein, who enhanced the theoretical understanding of light, space and time with the relativistic theory [17]. When Max Planck held his talk on the theory of the law of energy distribution in the normal spectrum, on 14th December 1900 at the Deutsche Physikalische Gesellschaft (DPG) it was the birth of quantum mechanics, which had a huge impact on atomism as well.

Quantum mechanics was the key to understand the physics occurring on very small length scales as well as the interaction of atoms and light<sup>5</sup>. Finally, this led to the development of techniques which opened a wide range of applications, that in turn enabled physicist to influence the systems they were researching. Compared to Astronomy for example, where there is no possibility of influencing the researched object, the experimental atomic physicists now developed tools which enabled them to conduct target-oriented experiments.

A significant device, based on a at that time extraordinary interaction between light and matter, is the *Microwave Amplification by Stimulated Emission of Radiation* (MASER) [19], developed in the 1950s. Its development was mostly based on research done by the Nobel prize winners of 1964: Charles Hard Townes, Nikolai Gennadienwitsch Basow and Alexander Michailowitsch Prochorow.

Shortly after the development of the *Maser* a discussion started, whether or not this technique could also be used in the optical spectral region. In 1958, Townes and Arthur Schawlow predicted the conditions to *Light Amplification by Stimulated Emission of Radiation* (LASER) [20]. Such a system was first developed two years later, in 1960, by Theodore Maimann. This was also the birth of modern atomic physics.

Based on this source of light with unique properties, a wide range of technical applications were developed, which gave scientists experimental access to atoms and their interactions. These unique properties: narrow spectral line width, high

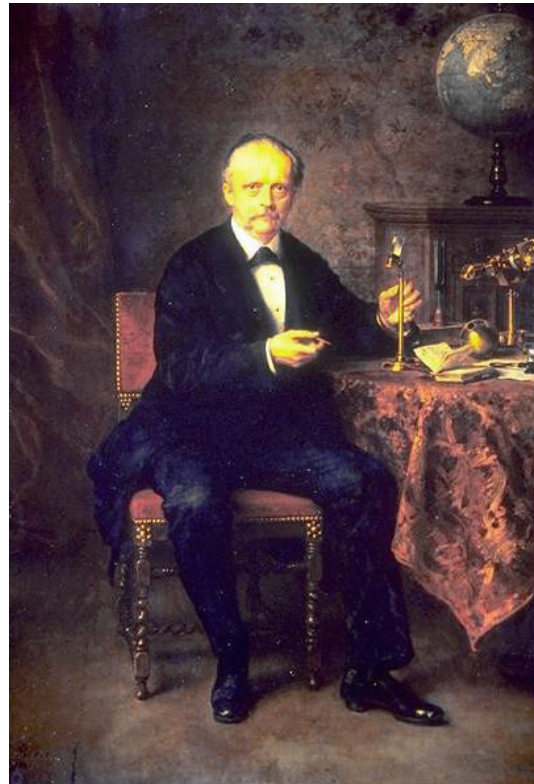


Figure 1.3: Hermann von Helmholtz was a German physicist and physician, who made significant contributions to a wide range of modern sciences [18]. Since 1887 he was the first president of the Physikalisch-Technische Reichsanstalt (PTR), the predecessor of the Physikalisch-Technische Bundesanstalt (PTB). Figure taken from [2].

<sup>5</sup>Already in the end of the 19th century first experiments, g.e. 1888 Johannes Rydberg, indicate the quantum character of atomism.

intensity and temporal and spatial phase coherence, make lasers perfect tools for atomic and molecular spectroscopy. Since then, entirely new investigations have become possible and have been improved by several orders of magnitude.

In the years 1967-1970, Arthur Ashkin and others developed the theory and later the experimental realization of *optical trapping* [21]. Lasers were used to trap very small particles like atoms or molecules in space.

His student, Steven Chu, enhanced this technique to the so called *Laser cooling* [22, 23], where the radiation pressure of light is used to decelerate the Brownian motion of atoms arising from their temperature. This technique was further improved to cool the atoms. For their work, Steven Chu, Claude Cohen-Tannoudji and William Phillips achieved the Nobel prize in 1997.

The combination of trapping, cooling, and spectroscopy on atoms enabled scientists to confirm fundamental theories, like the creation of a Bose–Einstein condensate [24], probably one of the fields of science with the highest attention in the last two decades. The same condition leads to technical applications like a new generation of optical clocks with an uncertainty in the order of  $< 10^{-17}$  — corresponding to less than one second in 3 000 000 000 years [25, 26].

Precise determination of long range interactions and scattering processes of the atoms are a prerequisite for a lot of these applications and research on fundamental theories in modern atomic physics. Scattering processes of atoms for example lead to collisional frequency shifts, contributing to the error budget of optical clocks, operating with atom clouds, and also Bose–Einstein condensation strongly depends on atom–atom collisions. The ability to control the strength of atomic interactions and the possibility to modify the scattering behavior of an ultra-cold atomic ensemble is hence a key technique for investigations in the whole field of quantum-degenerate gases of ultra-cold atoms and for studies of few- and many-body systems.

The most suitable known physical phenomenon with such a capability is a Feshbach resonances.

A Feshbach resonance is a scattering effect in physics, which is named after Herman Feshbach (figure 1.4) [27]. It should be mentioned that already in the 1930s the asymmetric shape of loss-spectra in noble gases due to coupling a continuum to a bound state, known as the "Fano-effect", was described theoretically [28]. It is based on the coupling of the scattering wave function to a bound molecular state.

In contrast to classical scattering processes of billiard ball-like particles it is not only possible to increase the interaction of the particles; if the scattering length is tuned to zero a non interacting regime is reached, and for negative scattering lengths the mean interaction energy can become negative like attraction.

The possibility to tune the scattering behavior and interaction of an atomic ensemble by Feshbach resonances gave access to study ultra-cold quantum gases [29], such as the formation of ultra-cold molecules [30], or the crossover between Bose–Einstein condensate to a Bardeen–Cooper–Schrieffer regime with fermionic gases [31], simulation of supernovae, and Efimov trimer states [32].

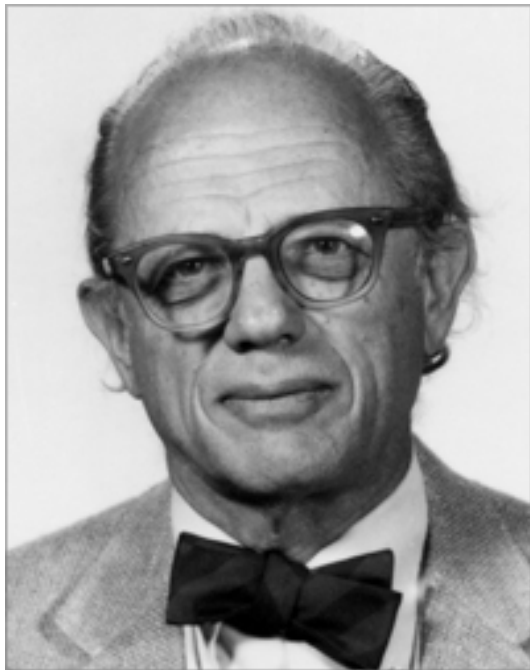


Figure 1.4: Herman Feshbach was an American physicist. He was an Institute Professor Emeritus of physics at MIT. Figure taken from [2].

There are several possibilities to couple the incoming wave to a bound molecular state for a Feshbach resonance. In the 1990s, a lot of predictions were made to modify the scattering length by magnetic coupling [33, 34, 35, 36, 37] or by radio frequency coupling [38]. At the end of this decade, the first magnetically induced Feshbach resonance was observed experimentally [39]. In a magnetic Feshbach resonance, the energy of a bound molecular state is tuned into resonance to the scattering state by altering an magnetic field.

In the same year, photoassociation (PA) spectroscopy was used to observe Feshbach resonances [40], already theoretically discussed ten years before [41]. A light field couples the scattering wavefunction of the ground state to an excited bound molecular state. It offers certain advantages over studying gas properties and provides a direct rapid signature of collisional resonances. It also bypasses a lot of difficulties when studying gas properties, which becomes important for very narrow resonances. Furthermore, PA precludes problems due to complicated analysis with contributions of different partial waves in gas thermalization experiments. Additionally, the laser frequency as an experimentally accessible parameter, allows studies of the energy dependence of various effects.

In the early days of the new millennium, experimental access was found [42] to modify the scattering length of atomic pairs, which are insensitive to magnetic fields, as was theoretically mentioned before, by an optical coupling [43, 44]. These so called optical Feshbach resonances hold several advantages compared to their magnetically induced counterparts. Light fields, can be switched much faster and, in contrast to magnetic fields they do not need to pass through the resonance in order to switch to "the other side" of the resonance, which causes losses [39, 45]. Furthermore, intensity and frequency are separately controllable parameters.

The tuning range of the scattering length as a function of the light field frequency in optical Feshbach resonances is limited by atom losses close to the resonance due to spontaneous decay [46]. Therefore, it was suggested to use ultra-narrow transitions, in order to overcome this limitation [47]. This makes alkaline earth elements as well as Ytterbium, with their two valence electrons, perfect candidates, due to their extremely narrow intercombination lines between the singlet and triplet systems. Their ultra-narrow transitions are used for a wide range of applications from metrological frequency standards [48, 49, 50] to fundamental research [51, 52, 53, 54, 55]. In the following years, photoassociation on the intercombination line was used for optical Feshbach resonances with  $^{171,172,176}\text{Yb}$  [56, 57, 29] and  $^{88}\text{Sr}$  [58, 59, 60]. The natural line widths of these elements are  $\Gamma_{\text{Yb}} \approx 182 \text{ kHz}$  and  $\Gamma_{\text{Sr}} \approx 7.5 \text{ kHz}$ .

In contrast to these elements, the small line width of  $^{40}\text{Ca}$  ( $\Gamma = 374(9) \text{ Hz}$  [61]) makes it a perfect candidate to reach the next order of magnitude in uncertainty of photoassociation spectroscopy [62] and for optical Feshbach resonances since for these even smaller natural linewidths less losses are expected.

Due to the small dipole matrix element in  $^{40}\text{Ca}$ , we are entering a new regime, where the long range molecular potentials are dominated by the van der Waals interaction. Due to the similar van der Waals coefficients in the involved ground state potentials and excited-state potentials of  $\text{Ca}_2$ , the PA differs considerably from other elements with stronger dipole interaction. This leads to a strong probability for spontaneous decay to bound molecular levels in the electronic ground state [63] and thus prevents applying the reflection approximation [64].

In addition, the small dipole coupling in Ca leads to excited potentials  $^3\Pi_u$  and  $^3\Sigma_u^+$ , that can be excited from the ground state and are predominantly attractive. These potentials therefore differ also from all other homo-nuclear PA studies investigated so far.

In this work the link of photoassociation, as spectroscopic tool, and the modification of the scattering behavior by optical Feshbach resonances in Calcium is presented. The present thesis is organized as follows:

The second chapter presents the experimental investigation of the relevant molecular potentials. As a first step, the previously unknown transition energies to the weakly bound molecular states close to the atomic resonance were measured by PA spectroscopy with an uncertainty on the order of a few kHz. Molecular states can effectively be coupled by rotational interaction, which leads to a striking dependence of the molecular  $g$ -factor on the vibrational levels. The observations are described by a theoretical model, which takes the spin-orbit coupling as well as the rotational interaction into account. This coupled channel model shows that only the inclusion of both, binding energies and effective  $g$ -factors, provide an accurate description of the long-range interaction potential. For the first time theoretically predicted long-range molecular coefficients based on *ab initio* calculations were compared to and confirmed by the experimentally derived coefficients.

In the third chapter, these excited state molecular potentials as well as corresponding ground state potential were used to predict the capabilities of optical Feshbach resonances in Calcium and compare it to other alkaline earth(-like) elements. Multi-color high intensity photoassociation spectroscopy was performed to test these theoretical predictions. Since the observed line shapes at high intensities cannot be explained by the existing models, in the fourth chapter a detailed discussion of the line shape and investigation of the loss rates is presented. This investigation proves the correctness of our molecular models as well of the existing PA models for low intensities. However these models do not provide a description for high intensities. Thus first discussions towards an enhanced model are presented.

As mentioned in the beginning, this work for me is a small step in the exciting field of modern atomic science, where light -as one of the most fascinating media and source of information- is used to enhance our fundamental knowledge about nature.



## Chapter 2

# Photoassociation experiment to determine molecular potentials

A detailed understanding of the coupling of atoms between the ground state continuum and excited molecular states by a light field is indispensable for the application of optical Feshbach resonances (OFR). Therefore I performed high-accuracy photoassociation (PA) spectroscopy, which enables modeling of the corresponding molecular potentials.

This chapter first gives a short summary of the theoretical background of light-assisted generation of molecules at the atomic asymptote  $^1S + ^3P$ , followed by the experimental setup for the presented measurements.

For these measurements, in a first step the so far unknown resonance frequencies of the weakly bound vibrational states near the asymptote to the pair  $^3P_1 + ^1S_0$  were measured. Different theoretical predictions [65, 66, 67] based on the first observed PA resonances [62] were used for a systematic search for the bound states.

For the identification of the vibrational states and for a detailed model of the corresponding molecular potentials also the gyromagnetic ratios were measured besides the binding energies of the three most weakly bound vibrational states relative to the transition energy of the  $^1S_0 + ^3P_1$  asymptote. Two accessible molecular potentials denoted as  $c0_u^+$  and  $(a, c)1_u$  of the atomic asymptote  $^1S + ^3P$  were investigated.

Based on these measurements the molecular potentials  $c0_u^+$  and  $(a, c)1_u$  were modeled by a close coupled channel model and the results were compared to *ab initio* calculations.

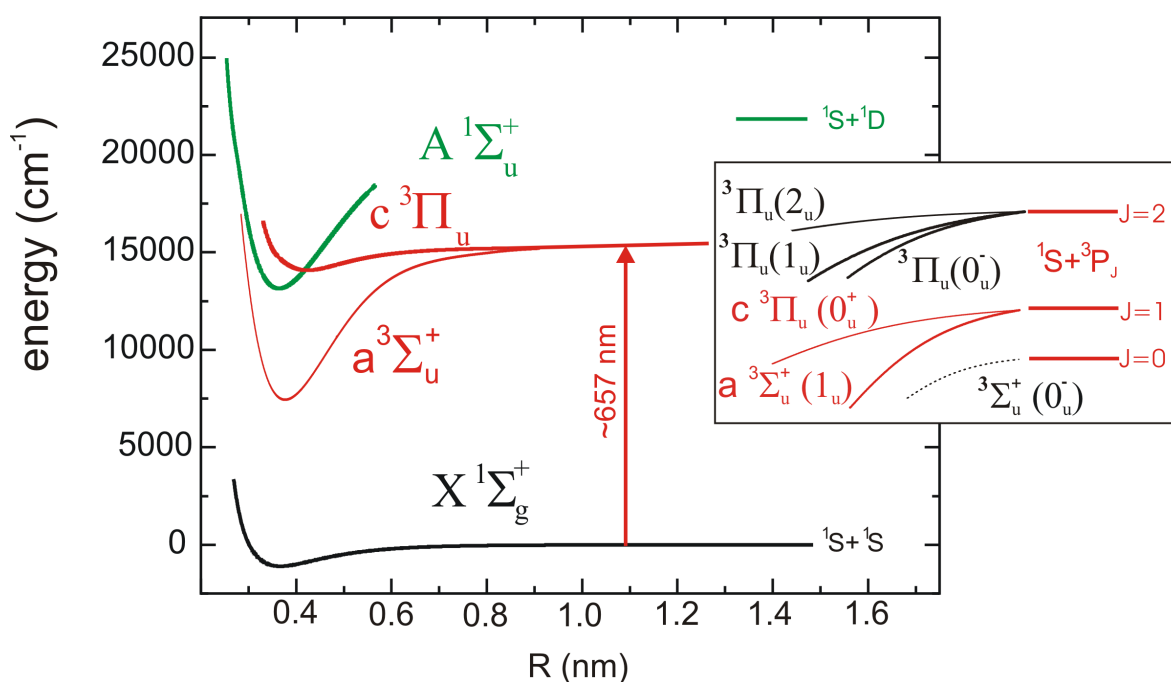


Figure 2.1: Plot of the  $\text{Ca}_2$  potentials corresponding to  $^1S_0 + ^1S_0$ ,  $+^3P$  and  $+^1D$  atomic asymptote - historically denoted as  $X$ ,  $a$ ,  $c$  and  $A$  - as a function of the internuclear distance  $R$  without fine structure. The inset shows the molecular potentials for large internuclear separation denoted in Hund's case (a)(c) and the corresponding atomic asymptotes. The photoassociation laser operates near the  $^1S_0 + ^3P_1$  asymptote ( $\lambda = 657 \text{ nm}$ ). Since this is a single-photon excitation and the ground state parity is *gerade* for the excited states, only states with electronic parity *ungerade* are accessible and included in the plot.

## 2.1 Light assisted generation of molecules at the intercombination line

For one  $^{40}\text{Ca}$  atom in the  $^1S_0$  ground state and another one in the  $^3P_1$  excited state approaching each other, the potential energy as function of the internuclear distance  $R$  separates into different molecular potentials. Two *ungerade* potentials (Fig. 2.1) can be excited from the  $X\ ^1\Sigma_g^+$  ground state by single-photon transitions; they are denoted by  $c\ ^3\Pi_u$  and  $a\ ^3\Sigma_u^+$  in Hund's case (a) [68] (see section 2.7). In the following these potentials will be denoted as  $a$  and  $c$ .

In the Born–Oppenheimer approximation [69] in a diatomic molecule, the energy  $V(R)$  of the electronic state at a fixed separation  $R$  of the nuclei creates the potential for the relative movement of the nuclei.

Generally, the molecular potential at large internuclear separation  $R$  can be expressed as an inverse power sum

$$V(R) = \sum \frac{C_n}{R^n}, \quad (2.1)$$

originating from a multi-pole expansion of the atom–atom interaction.

In the potential correlating to the  $^1S_0 + ^3P_1$  atomic states, the  $C_3$  coefficient is directly related to the dipole matrix element of the atomic  $^1S_0 - ^3P_1$  transition. It can be expressed as a function of the lifetime  $T = 1/\tau$  and the transition's angular frequency  $\omega$  yielding  $C_3 = \frac{3\hbar c^3}{2\tau\omega^3}$  [58]. For excitations on the intercombination line of calcium between the  $^1S_0$  ground state and the excited  $^3P_1$  state, the line width is  $\Gamma = 374$  Hz [61], and the contribution of the dipole interaction is very weak. In contrast to other narrow line PA measurements with alkaline earth(-like) elements like Sr and Yb, we enter a new regime in Ca, which is dominated by the next order of Coulomb interaction.

The  $C_6$  coefficient corresponds to van der Waals induced dipole–dipole interaction, whereas the  $C_8$  coefficient corresponds to the induced dipole–quadrupole interaction.

So far, the molecular potentials at the intercombination line for large internuclear separations of Ca have not been experimentally investigated yet. The dominant coefficients in this regime -  $C_3$ ,  $C_6$  and  $C_8$  - were calculated [63, 70] *ab initio* based on coupling strengths determined experimentally from atomic spectroscopy. The molecular potential is usually modeled by a fit to molecular spectroscopy data

[70, 71]. Due to the unknown phase accumulated in the inner region of the molecular wavefunction, the exact position of the near-asymptotic vibrational states cannot be extrapolated from the long range behavior only. Thus it does not provide predictions of the binding energies of the most weakly bound states.

Two atoms, excited to a bound vibrational state, can decay spontaneously back into the ground state continuum or to a bound state in the  $X^1\Sigma_g^+$  molecular ground state potential. The probability for a decay to a certain kinetic energy in the ground state continuum of this dimer depends on the Franck–Condon density<sup>1</sup>. Since this kinetic energy is typically much higher than the trap depth and cold molecules in the  $X^1\Sigma_g^+$  potential were not detected by our detection method, the photoassociation of an excited cold molecule can only be observed as a loss of atoms. For a more detailed discussion of the atom losses, see chapter 4.

## 2.2 Experimental realization

For the investigation, Ca atoms are first trapped and cooled optically. Since we are interested at two-body processes at low kinetic energies, we have to prepare the atoms at low temperatures and high densities. In this section, our experimental setup scheme is summarized shortly. For a detailed description of the setup, briefly I will refer to the corresponding publications; only the latest modifications and improvements for PA measurements being part of my contribution will be mentioned separately.

A schematic drawing of the experimental setup is given in figure 2.2. The experiment takes place in a vacuum chamber [72, 73] at a pressure of  $p = 2 \cdot 10^{-10}$  mbar.  $^{40}\text{Ca}$  atoms are trapped and cooled in two subsequent magneto-optical trap (MOT) stages [74]. The first stage operates on the  $^1S_0 - ^1P_1$  fluorescence transition. After one second of loading up to  $10^9$  atoms are trapped at a temperature of  $1 - 2$  mK. A loss channel to the metastable  $4s3d\ ^1D_2$  state (see figure 2.3) is closed by a repump laser system [61, 75]. In a second stage of magneto-optical trapping operating on the  $^1S_0 - ^3P_1$  transition, for 300 ms up to  $4 \cdot 10^7$  atoms are trapped at a temperature of  $T \approx 12\ \mu\text{K}$ . In order to increase the photon scattering rate on this transition additionally a quench laser is applied coupling the  $^3P_1$  state to the  $4s4d\ ^1D_2$  state. In a third

---

<sup>1</sup>This is not a coupling between two discrete states but rather a coupling between a continuum of states to a bound state. Thus the Franck–Condon factors for the density of states as a function of the kinetic energy in the continuum are denoted as Franck–Condon density (FCD).

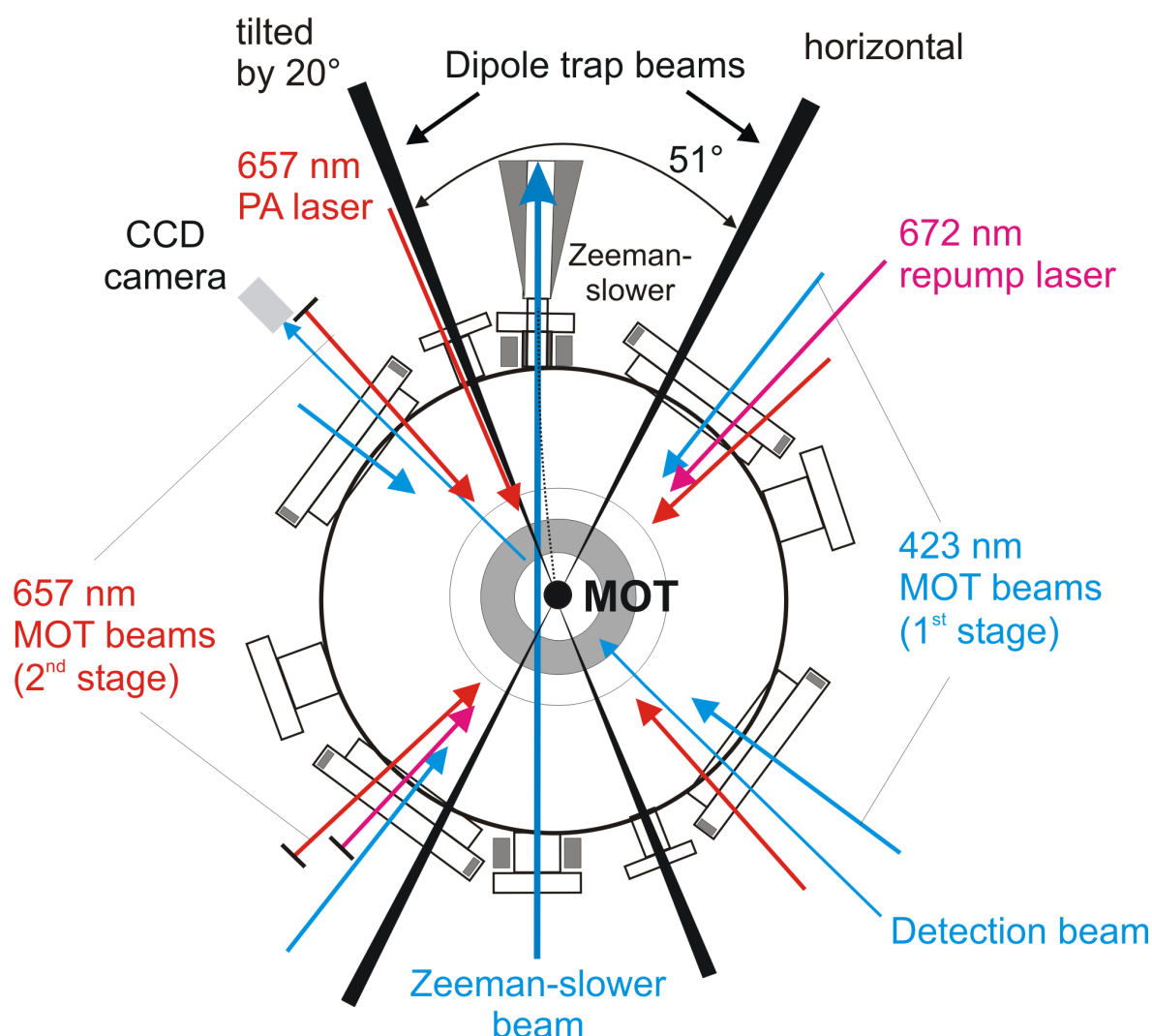


Figure 2.2: Schematic drawing of the vacuum chamber and the laser beams for trapping and cooling the atoms. The atoms emitted by an oven are decelerated by a Zeeman-slower beam and deflected by an optical molasses (not shown in the figure) towards the center region of the chamber. Thus the trapped atoms are not affected by the Zeeman-slower beam. In the center of the chamber, the atoms are trapped by the first-stage MOT beams operating at 423 nm. The repump laser system operating at 672 nm, which is retro-reflected to the atomic cloud, is aligned to this center region. The second stage MOT beams, operating at 657 nm, are retro-reflected. (For the MOTs only the horizontal beams are shown in the figure) The quench laser light at 453 nm, irradiated vertically from the bottom and retro-reflected, is not shown in the figure. The third trapping stage is a crossed dipole trap. The horizontal angle of the beams is  $51^\circ$ , and one beam is  $20^\circ$  tilted relative to the horizontal plane. The photoassociation laser light is irradiated from one side almost parallel to the tilted dipole trap beam. For detection a CCD camera and a resonant laser beam operating at 423 nm are used.

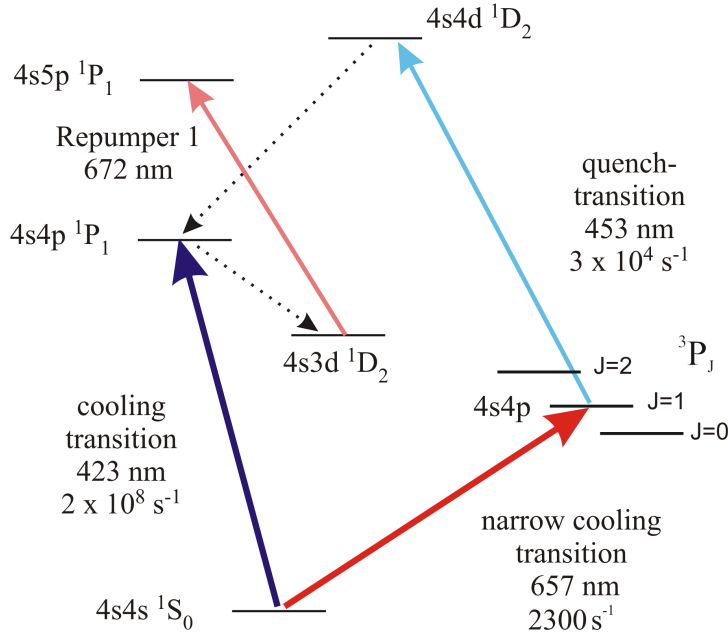


Figure 2.3: Simplified energy level diagram for  $^{40}\text{Ca}$  showing the main cooling transitions, decay channels, the quench transition and the repumping transition.

stage of trapping the atoms were loaded into a crossed dipole trap [76, 62] operating already during both MOT stages. A temperature of  $T \approx 15\ \mu\text{K}$  is reached for this trapping. After further evaporation [77, 62] by lowering the dipole trap depth about  $N = 150\ 000$  atoms are prepared at a temperature of  $T \approx 1\ \mu\text{K}$  and a peak density of  $\rho \approx 1.1 \cdot 10^{19}\ \text{m}^{-3}$ .

### 2.2.1 Compact laser frequency stabilization

In previous experiments with this setup [61, 76], the 423 nm laser light was stabilized to an atomic beam, and the 453 nm quench laser light was stabilized to a He-Ne laser via a transfer cavity. The eigenfrequency of the transfer cavity relative to the atomic transition had to be measured every time. Further, this technique was circuitous due to its higher complexity and thus more sensitive for perturbations compared to stabilization to a reference cavity, as was already being used for the 672 nm repump laser light [61]. Therefore, the stabilization of the 423 nm and 453 nm laser light was changed to a reference resonator. Figure 2.4 shows the resonator in the open vacuum chamber.

Since it is almost impossible to predict the exact value of the eigenfrequency of a cavity relative to a given frequency (in our case atomic transitions), the design

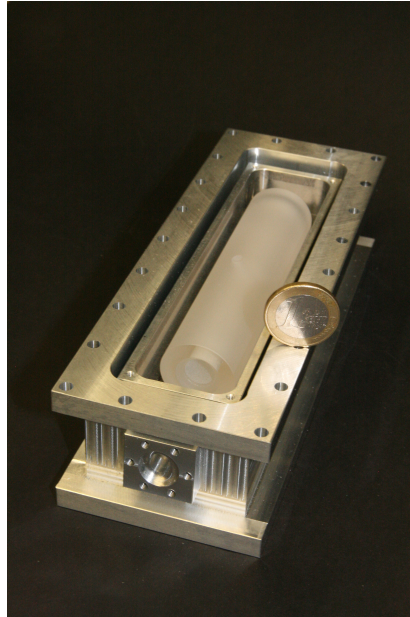


Figure 2.4: Optical resonator with an Ultra Low Expansion (ULE) glass spacer mounted in an aluminium heat shield inside the open vacuum chamber. The coin demonstrates the compactness of the setup.

has been chosen in such a way that a laser at any given frequency can be stabilized to this cavity<sup>2</sup>. The length of the resonator spacer was chosen to be  $l = 10$  cm. This leads to a free spectral range of 1.5 GHz [78]. The resonator configuration is plane–concave with a concave radius of  $r = -200$  mm. Therefore, we do not expect a superposition of the different eigenmodes of the resonator, and the relative frequency shifts between the  $TEM_{00}$ ,  $TEM_{10}$  and  $TEM_{20}$  modes are about 375 MHz. This means that there is a maximum of  $< 200$  MHz of frequency difference between the eigenfrequencies of different mode orders ( $TEM_{00}$ ,  $TEM_{10}, \dots$ ) of the resonator and each possible atomic transition frequency. Differences in the MHz range can easily be bridged by an acousto-optic modulator (AOM). The AOM is in double-pass configuration in order to avoid readjustments when the AOM carrier frequency is changed. Furthermore, the AOM is used to modulate the laser frequency for a lock-in stabilization of the laser frequency [78]. The entire setup is shown schematically in figure 2.5.

The line widths of the corresponding transitions are  $\Gamma(^1S_0 - ^1P_1) \approx 34$  MHz and  $\Gamma(^3P_1 - ^1D_2) \approx 4$  kHz. Therefore the coating of the mirrors has been chosen to provide for the optical wavelength of these transitions a reflection coefficient of

<sup>2</sup>Cavity configuration was calculated and technically designed by Dr. Sebastian Kraft.

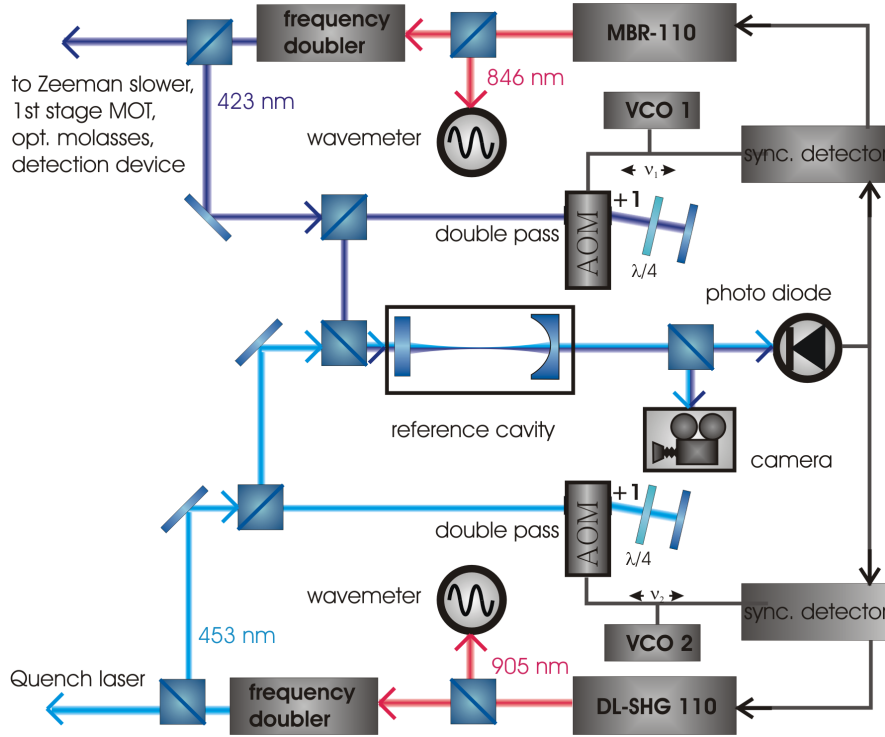


Figure 2.5: Schematic picture of the 423 nm and 453 nm laser frequency stabilization to a single reference resonator. The frequencies of the voltage-controlled oscillators (VCO), driving the AOMs, are frequency modulated by different modulation frequencies in order to allow a separate lock-in detection for both lasers.

$R = 99.7\%$  — leading to a finesse of  $\mathcal{F} = 1\,000$  [78]. The spacer length of  $l = 10$  cm results in [78] a line width of the resonator of  $\Delta = 1.5$  MHz. A lock-in stabilization with MHz width was sufficient for a frequency stabilization with kHz stability.

Using two different modulation frequencies for the 423 nm and 453 nm laser light, it was possible to use a single reference cavity and a single photo diode for a lock-in frequency stabilization of both lasers (see Figure 2.5). The lock-in stabilizes the frequency of the infrared lasers used to generate the 423 nm and 453 nm laser light (the generation of the 423 nm and 453 nm laser light is explained in [62]). Monitoring the transmitted laser light by a camera and additionally measuring the wavelength of the infra-red laser light by a wave meter, the right mode can be easily found within seconds, which simplifies the frequency stabilization procedure for these lasers considerably.

It has been found that temperature-stabilized ULE spacers are changing their length over time due to an aging process [79]. Therefore, the relative frequency difference of the eigenresonances of the reference cavity with respect to the relevant

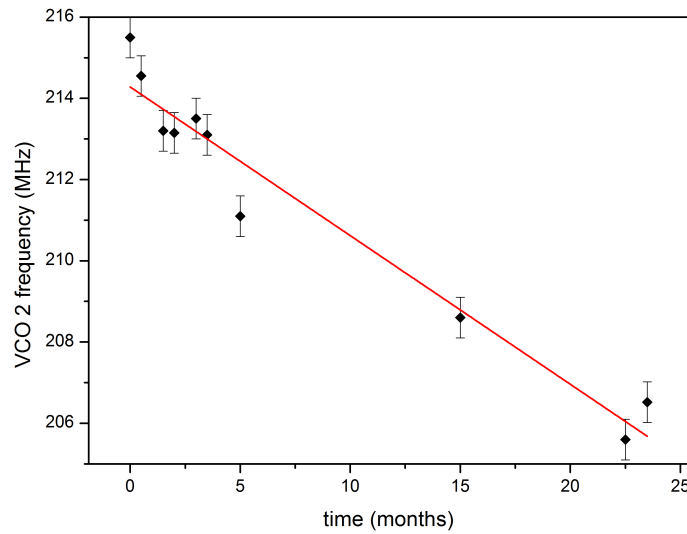


Figure 2.6: Optimal VCO frequencies for the 453 nm laser light (black diamonds) leading to optical drift rate (red line) of  $\approx 0.27$  Hz/s.

atomic transitions, which is bridged by the AOM frequency shift, is changing over time. Thus it requires a continuous readjustment of the AOM driving frequencies over time. Since the  $^1S_0 - ^1P_1$  transition has a natural line width of  $\Gamma \approx 34$  MHz, a readjustment was necessary on a typical time scale of about a year and can be easily done by optimizing the frequency of the resonant laser light used for detection of the atoms by tuning the AOM frequency. Once a different frequency of the resonance has been found, the frequency of the detection beam had to be set and the modulation AOM of the corresponding lock-in has to be changed by half of the amount - since it is in double pass configuration - in order to fix the relative detuning of the laser lights of the first stage MOT (Zeeman slower, optical molasses, cooling beams and detection beams).

The 453 nm  $^3P_1 - ^1D_2$  transition width is much smaller however. Therefore, the time scale of necessary AOM frequency corrections is on the order of weeks. It can be easily readjusted by optimizing the AOM frequency to maximize the atom number of the second MOT stage. Figure 2.6 shows the derived optimal AOM frequencies of the 453 nm laser light over two years. The indicated uncertainty is derived from the estimated width of the optimum. The average drift of the ULE resonator eigenfrequency is about 0.27 Hz/s.

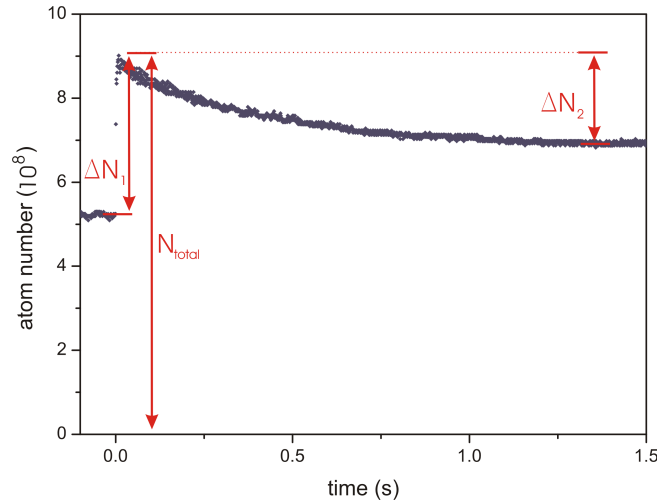


Figure 2.7: Atoms in state  $^1P_1$ , trapped in the first stage MOT if the 657 nm transition to  $^3P_1$  is driven simultaneously. At time  $t=0$  the 657 nm laser beam is switched off.  $\Delta N_1$  is the number of atoms which has been stored in the  $^3P_1$  state,  $N_{total}$  is the total number of atoms in the MOT and magnetically stored, and  $\Delta N_2$  is the increase of atom number with 657 nm loss compared to usual MOT operation.

## 2.2.2 Dark-state MOT and loading scheme

Since PA is a density dependent process, the weak transitions to the  $a^3\Sigma_u$  and  $c^3\Pi_u$  potentials - especially for more deeply bound states - for which coupling strength is predicted to decrease [63] can only be observed at high atom densities. Therefore the atom density in the dipole trap was increased by implementing a dark-state MOT loading scheme.

The maximum density and atom number in a MOT is mainly limited by two processes: First, due to repulsive forces between the atoms caused by re-absorption of scattered photons [80], and, second, by inelastic collisions between ground- and excited-state atoms [81], which result in a trap loss. Confining the atoms in a dark state, which does not interact with the trapping light [82] has been proven to be a very successful method to overcome these limitations. This method is now regularly applied in alkaline dark-spot MOTs and has been applied recently in Sr and Yb [83, 84, 85]. Here we use a variant of this method with a calcium MOT operated on the 423 nm  $^1S_0$ - $^1P_1$  transition (Fig. 2.3).

To put atoms in a dark state, we drive the  $^1S_0$  -  $^3P_1$  transition at 657 nm simultaneously to the 423 nm MOT. The repump laser at 672 nm was applied to reduce loss through decay to the  $^1D_2$  state. For excitation to the  $^3P_1$  state, we simply use the second stage MOT beams at 657 nm [61] with an intensity of  $I \approx 490 \text{ W/m}^2$ ,

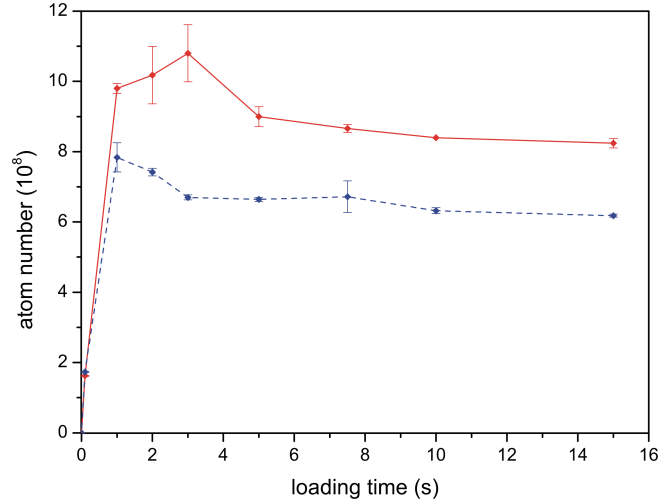


Figure 2.8: Number of atoms in the first stage MOT as function of time with (red line) and without (blue dashed line) driving the 657 nm transition.

broadened in the same way as for the second MOT stage. Atoms excited to the  $^3P_1$  state are non-resonant for the first stage cooling transition and are not subject to re-absorption scattering that limits the density. However, collisions between  $^3P_1$  and  $^1P_1$  atoms can still occur with an unknown cross section.

To evaluate the efficiency of this process we operate the 423 nm MOT together with the 657 nm laser beams for several seconds to reach an equilibrium between the loading and the loss rates. Then we switch off the 657 nm light. The fluorescence of the 423 nm MOT is proportional to atoms in the  $^1P_1$  state and proportional to the total number of atoms the the ground state and the  $^1P_1$  state (Fig. 2.7). Conversion of the fluorescence signal to atom numbers is independently calibrated via absorption images.

When the 657 nm light is switched off the fluorescence signal increases, corresponding to an increase of the atom number in the  $^1S_0$  and the  $^1P_1$  states by  $\Delta N_1 \approx 3.8 \cdot 10^8$ .  $\Delta N_1$  corresponds to the number of atoms which have been stored in the  $^3P_1$  state. This increase is on the order of  $\Delta N_1/N_{\text{total}} \approx 40\%$  of all atoms.

After one second, the number of atoms trapped in the 423 nm MOT alone (about  $10^8$  atoms) is almost in equilibrium. The fact that the equilibrium number with 657 nm laser is lower than the number for the 423 nm MOT alone can be explained by to additional collision losses from the atoms in the  $^3P_1$  state. In summary, we have thus increased the number of atoms by  $2 \cdot 10^8$ , i.e.  $\approx 30\%$ .

Figure 2.8 shows the loading curve of the first stage MOT with and without additional driving of the 657 nm  $^1S_0 - ^3P_1$  transition, measured by absorption images.

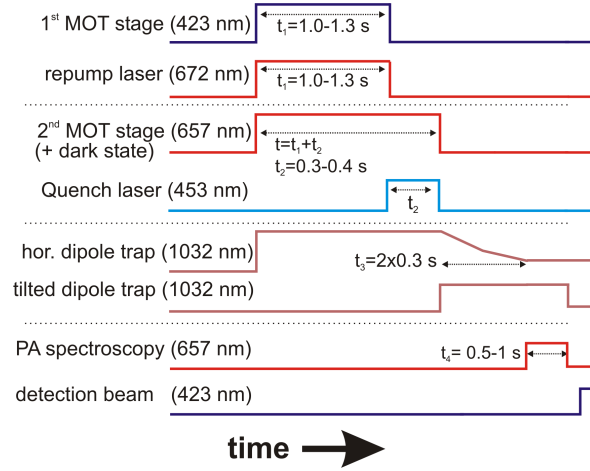


Figure 2.9: Temporal sequence for PA spectroscopy.  $t_1/t_2$  is the loading time for the first/second MOT stage.  $t = t_3$  is the ramp time of the horizontal dipole trap. The atoms remain in the crossed dipole trap for the PA irradiation time  $t_4$ . After an expansion time of typically  $t \approx 100 \mu\text{s}$  the detection beam resonant to the  $^1S_0 - ^1P_1$  transition is applied.

The fact that, in both cases, the total number of trapped atoms after a few seconds is above the equilibrium value can be explained by collisions with atoms which have decayed to the  $^3P_2$  state and are magnetically trapped in the field of the MOT, even when the 672 nm repump laser is used (see appendix).

For photoassociation, further cooling to microkelvin temperatures is necessary. When we use the combination with the second MOT stage, we find an increase of the atom number in the first stage MOT by a factor of up to 30%, leading to an increase in the second stage MOT atom number of up to 100% and to an increased of atom density by up to 50% in the dipole trap. This significant increase – well above the increase observed in the first MOT stage alone – is most likely due to a local increase of the density at the center of the MOT, which has a large influence on the transfer efficiency due to the small capture radius of the second MOT stage.

Based on these investigations the trap loading process was changed in order to achieve higher atom densities in the dipole trap. Instead of switching on the second stage MOT lasers at the instant when the first stage MOT light is switched off, we already apply the second stage MOT laser beams during the loading time of the first stage MOT. The loading scheme for the PA measurements presented in this work is shown in figure 2.9.

Applying this scheme, up to 300 000 atoms after an irradiation time of  $t_4 = 0.5$  s were trapped at a temperature of  $T \approx 1 \mu\text{K}$ . With these dipole trap laser powers the PA spectroscopy laser is typically applied for  $t_4 = 0.05 - 3$  s.

A loading scheme that has been further improved will be discussed in appendix A.

The atoms in the dipole trap are irradiated by the PA laser with a maximum intensity of  $I = 150 \text{ W/cm}^2$ . The PA-induced loss of atoms is detected via absorption imaging. The PA laser with a width below 2 kHz can be precisely tuned by a beat lock to a laser stabilized on an ULE reference resonator [86, 79]. The beat lock will be presented in the following section 2.2.3.

### 2.2.3 Photoassociation frequency measurements and stabilization

To determine the exact binding energy of PA resonances relative to the atomic asymptote, in a first step the PA resonance frequency relative to the eigenfrequency of the ULE reference resonator was determined. In a second step, for each PA measurement the relative detuning of the eigenfrequency of the ULE resonator to the atomic  $^1S_0 - ^3P_1$  transition was measured.

The PA measurements for each state as well as the atomic spectroscopy were both performed within less than one hour for each molecular resonance. From [79] it was known that the drift of the cavity resonance was up to 55 mHz/s averaged over months. The deviations over a single day were measured to be less than  $\pm 2$  kHz, as determined by absolute frequency, measured with a femtosecond frequency comb. The left graph in figure 2.10 shows the absolute frequency measurements with the frequency comb. The right graph in figure 2.10 shows the averaged drift over three months.

This average drift was continuously corrected during the measurements by changing the frequency of the offset AOM to the reference cavity. Also, by repeated measurements of the relative frequency during a day, no additional drift was observed within the experimental resolution of 4 kHz; thus an additional uncertainty due to the cavity drift between the PA and the atomic reference scan due to this drift was neglected.

So far, only theoretical predictions of the long-range potential exist for Ca. Thus the binding energies of the weakly bound molecular states, besides the  $v' = -1$  states [62], are unknown. Therefore a variation of the laser frequency between 10 and 20 kHz was chosen from shot to shot for a scan of the expected narrow resonances. Based on measurements of the binding energies of the most weakly bound states in the  $a$  and  $c$  potential, theoretical predictions for the energies of the more

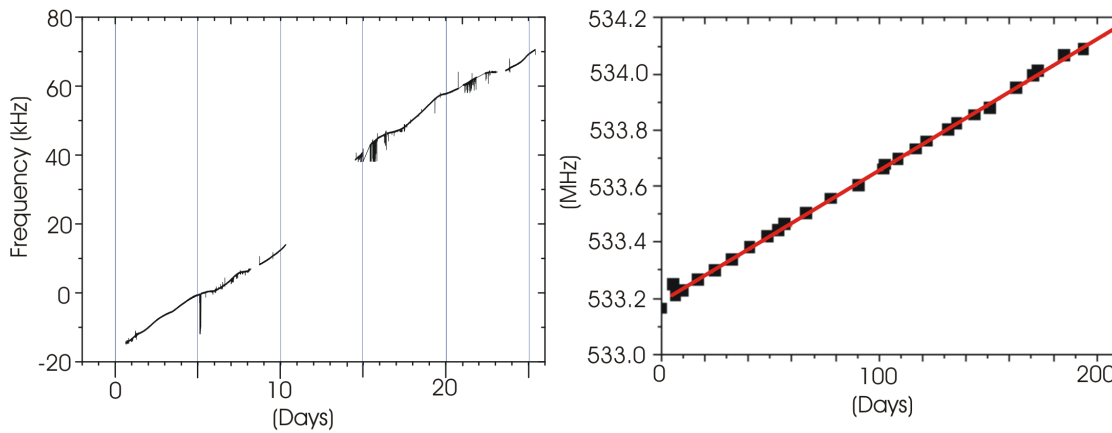


Figure 2.10: Left side: Eigenfrequency of the ULE reference cavity measured with a frequency comb as function of time in the year 2010. The drift measurement amounts to 36 mHz/s. Right side: Long term drift of the reference cavity in the year 2007, measured from the offset between the calcium intercombination line and an eigenmode of the cavity, which amounts to 55 mHz/s (figure taken from [79]). The change of the drift over the years could be an effect of the aging of the ULE spacer [87].

deeply bound states are presented in [62], allowing for systematic search for more deeply bound states. The uncertainties of these predictions were on the order of 150 MHz<sup>3</sup>. The determination and characterization of the six most weakly bound molecular states demands about 500 000 single measurements.

The PA laser frequency is stabilized by a beat lock with the diode laser which in turn is stabilized to the ULE resonator close to the atomic resonance used for the second stage MOT. In order to observe binding energies of down to  $h \cdot 40$  GHz with a spectroscopy laser, the existing experimental setup [62] had to be extended. The scheme for the whole beat frequency stabilization of the PA master laser is shown in figure 2.11. The photo diode is an ultra-fast photo diode<sup>4</sup> with bandwidth 60 GHz. The photo diode signal was first amplified by a high frequency amplifier and subsequently mixed down by synthesizer 1 with a maximum output frequency of 40 GHz to reach a beat frequency below 2.4 GHz. This frequency in turn was mixed down to 25 MHz by synthesizer 2. This beat, at 25 MHz, is compared in a phase-frequency detector, to a 25 MHz reference<sup>5</sup>, to generate an error signal to stabilize the frequency of the PA spectroscopy laser. By changing the frequency of synthesizer 2, it was pos-

<sup>3</sup>Private communication Oliver Appel.

<sup>4</sup>type: New Focus 0821A

<sup>5</sup>Reference signal given by an H-Maser referenced to the cesium fountain clocks of PTB.

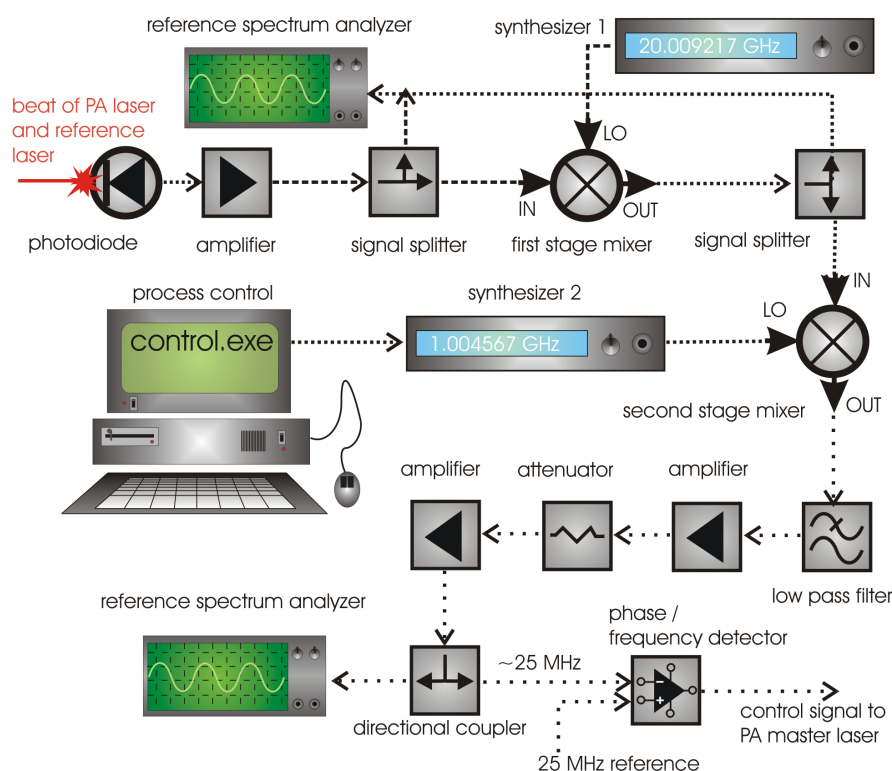


Figure 2.11: Schematic drawing of the enhanced beat lock setup in two stages.

sible to scan the spectroscopy laser [62]. The photo-diode signal as well as the beat signal, mixed down and stabilized to 25 MHz, were monitored by spectrum analyzers. The laser frequency was additionally monitored by a wave meter for a coarse adjustment of the laser frequency. From the signal of the gain, other possibilities for locking would be about 2 GHz detuned, which can be excluded from the wavemeter data, and from the beat frequency behavior for changing the mirror-piezo voltage of the diode laser for PA spectroscopy, which is in Littrow configuration.

The beat lock contribution to the uncertainty of the spectroscopy laser due to an imperfect lock was estimated from the beat spectrum to be less than 2 kHz for beat lock frequencies of  $\approx 25$  GHz and has therefore no significant contribution to the total measurement uncertainty.

Since, during the measurements, the frequency  $f_2$  of synthesizer 2 is continuously changed, the PA loss spectrum is measured as function of the synthesizer 1 frequency  $f_1$ . Taking all relevant acousto-optic modulators into account, the frequency of the PA spectroscopy laser relative to a laser on resonance to the atomic  $^3P_1$  state (compare [62]), and thus the binding energy of the PA resonance, can be calculated as function of the synthesizer frequencies

$$E_{bin}/h = f_1 + f_2 - 2 \cdot (DDS_{sweep} + AOM_{crm}) + 8 \text{ MHz} + \Delta_{corrections}, \quad (2.2)$$

where  $E_{bin}$  is the binding energy of the PA resonance relative to the atomic  $^1S_0 - ^3P_1$  transition,  $DDS_{sweep}$  is the frequency of a DDS responsible for the automatic drift compensation of the ULE cavity spacer. Here,  $AOM_{crm}$  is an AOM frequency, which is adjusted manually in order to tune the second MOT stage laser light frequency. The sum of both frequencies is given fed to double pass AOM (and therefore has to be taken into account twice).  $\Delta_{corrections}$  is the sum of several physical corrections, discussed later in this chapter. The 8 MHz term is the result of several constant frequency shifts due to AOMs and the 25 MHz of the phase lock.

## 2.3 Theoretical predictions for the binding energies

Appel [62] used the measured binding energies of the most weakly bound states, denoted as  $v' = -1^6$ , in the potentials  $a$  and  $c$  together with four different methods to predict the binding energies of the more deeply bound vibrational states:

- (1) A pure van der Waals potential using the Le Roy–Bernstein formalism neglecting rotational energy of the molecule [65].
- (2) A pure van der Waals potential using the Raab–Friedrich formalism neglecting rotational energy of the molecule [66].
- (3) A pure van der Waals potential using the Le Roy–Bernstein formalism including rotational terms [67].
- (4) An advanced Le Roy–Bernstein formalism considering rotational energy [67] and in addition to the van der Waals term  $C_6$  the  $C_8$  coefficient [88].

---

<sup>6</sup>In this work the bound vibrational states are denoted as follows: If it is a bound state in a molecular potential corresponding to an atomic asymptote where at least one of the atoms is excited from the ground state " ' " was used to clarify that state is an excited one. Positive numbers indicate the vibrational state counted from the potential minimum. If the number is negative the vibrational state is counted from the atomic asymptote with  $-1$  indicating the most weakly bound state.

state		binding energy $E/h$ (GHz)			
$v'$	$\Omega$	(1)	(2)	(3)	(4)
-2	0	4.01	4.08	4.51	4.58
-2	1	6.85	6.91	7.04	7.34
-3	0	15.65	15.86	17.19	17.71
-3	1	22.04	22.21	22.62	24.35

Table 2.1: Theoretically predicted binding energies of deeper bound states ( $v' = -2, -3$ ) by various formula. The quantum number  $v'$  determines the vibrational state counted from the asymptote.

Table 2.1 shows the predicted binding energies presented in [62] for the molecular potentials  $a$  and  $c$  calculated for all methods mentioned above, based on the measured binding energies of the most weakly bound states in both potentials. *Ab initio* calculated van der Waals potential coefficients [70] were used for these calculations.

Expecting method (4) to be the most accurate<sup>7</sup> these predicted binding energies were used as starting points for the spectroscopy. From these starting points, the spectroscopy was performed in alternating  $\pm 10$  MHz from the starting point.

## 2.4 Experimental results for PA binding energy measurements

Molecules excited by photoassociation lead to a loss of atoms in the trap due to spontaneous decay. PA is a two-body loss process. Thus we describe the time evolution of the atomic density  $n$  due to photoassociation by the differential equation  $\frac{d}{dt}n = K(\Delta, I, T)n^2$ , where  $K$  is the PA loss coefficient and a function of the frequency detuning  $\Delta$  to a PA resonance, the PA spectroscopy laser intensity  $I$  and the temperature  $T$ .

Experimentally, the atomic density could not directly be observed. We assume a constant size of the trapped atom cloud, leading to a linear dependence of the atomic density on the total atom number  $N$ . Thus we use the solution of the differential equation  $\frac{d}{dt}N = \beta(\Delta, I, T)N^2$  ( $\beta/K$  see chapter 4), given by

$$N(t) = \frac{N_1}{1 + t \cdot \beta(\Delta, I, T) \cdot N_1}, \quad (2.3)$$

<sup>7</sup>Private communication Oliver Appel.

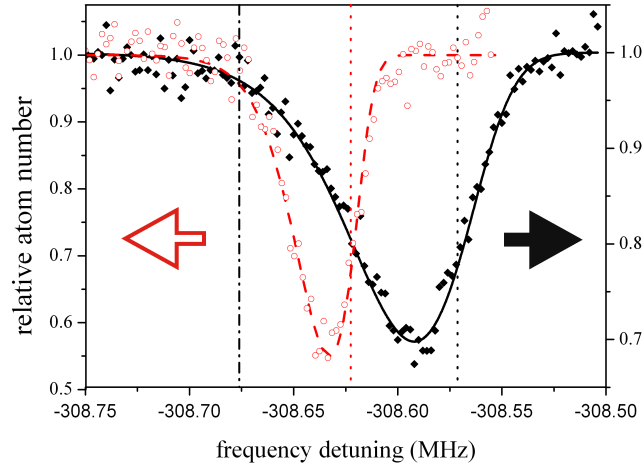


Figure 2.12: Trap loss as function of frequency detuning  $\nu - \nu_{atom}$  ( $\nu_{atom}$  denotes the true atomic resonance frequency  $E(^3P_1)/h$ ). The dipole trap is operated at powers of 0.6/1.6 W in the horizontal and tilted beam (full circles) and 0.3/0.8 W, respectively (open circles) at PA intensity of  $I = 6 \text{ mW/cm}^2$ . The black full line and the red dashed line show a fit described in the following section for temperatures of  $T = 1.0 \text{ } \mu\text{K}$  and  $T = 0.5 \text{ } \mu\text{K}$ , respectively. The dotted lines indicate the corresponding frequencies at  $T = 0$ , and the dash-dotted line the resonance frequency extrapolated to zero trap depth.

where  $N_1$  is the initial atom number which is equal to the atom number far off resonance,  $t$  the exposure time of the PA-inducing laser, and  $\beta(\Delta, I, T)$  the atomic loss rate. For the determination of the resonance frequency, low PA spectroscopy laser intensities were chosen to avoid power broadening by the laser light. Therefore, for low PA intensities the shape of  $\beta(\Delta)$  was assumed to be Gaussian because the largest effect is Doppler broadening. The Lorentzian natural line width of the molecular transition, which was assumed to be two times the natural atomic line width of  $374(9) \text{ Hz}$  [61], is small compared to the Doppler FWHM of  $36 \text{ kHz}$  at a temperature of  $1 \text{ } \mu\text{K}$ .

To avoid line shifts and broadening by an uncompensated residual magnetic field<sup>8</sup>, an external magnetic field of about  $B = 0.285(7) \text{ mT}$  was applied by two coils in Helmholtz configuration, leading to a Zeeman-splitting in the MHz-range and the central non-shifted  $M=0$  component was measured.

Figure 2.12 shows such a curve at different dipole trap depths of the dipole trap. To determine the exact frequency relative to of the PA resonance to the eigen-

<sup>8</sup>PA measurements in absence of the external field indicates a remaining non-compensated magnetic field of  $B \approx 7 \text{ } \mu\text{T}$ .

frequency of the ULE reference resonator from such curves, several corrections have to be taken into account: The photon recoil shift, the kinetic collision energy shift [89], the quadratic Zeeman effect, and the light shifts due to the dipole trap laser and the PA inducing laser<sup>9</sup>. These corrections as well as the Doppler broadening will be discussed in the following.

### 2.4.1 Thermal broadening

Besides their center of mass velocity (see next section), the pair of colliding atoms possesses kinetic energy from their relative movement, which reduces the necessary photon energy for the transition. The kinetic energy relevant for the formation of a molecule follows a Boltzmann distribution. We describe the trap losses as pure two-body losses with a loss coefficient  $\beta$ . For low PA-inducing laser intensities the power broadening is not dominant, and the asymmetric line shape [63] due to the kinetic energy of the atoms is observable. We therefore describe the atom loss as a superposition of Gaussians weighted and shifted according to the thermal distribution [89]

$$\beta(\Delta, T) = \frac{2}{\sqrt{\pi}} \int_0^\infty d\epsilon \beta_D(\Delta, \epsilon) e^{\frac{-\epsilon}{k_B T}} \cdot \frac{\epsilon^{l+1/2}}{(k_B T)^{3/2}}, \quad (2.4)$$

where  $l$  is the orbital angular momentum of the scattering partial wave,  $\beta$  is the loss coefficient as a function of the frequency  $\Delta$  and temperature  $T$ ,  $h \cdot \epsilon$  the collision energy, and  $\beta_D(\Delta, \epsilon)$  is the Doppler distribution as function of frequency  $\nu$ .

The integral was approximated by a sum of different collision energies with corresponding frequency shifts in our calculation. PA is induced at a temperature of  $T \approx 1 \mu\text{K}$ , and therefore only s-wave scattering ( $l = 0$ ) is relevant [76]. Furthermore, for low PA intensities, the shape of  $\beta_D(\nu)$  was assumed to be Gaussian, since the natural line width compared to the Doppler width (see next section) for the estimated temperatures is more than one order of magnitude smaller and no stimulated broadening is expected for the corresponding irradiation intensities.

The principle of this summation of Gaussians that are shifted and weighted due to their thermal distribution is shown in figure 2.13.

---

<sup>9</sup>The different frequencies of the atom number minima as g.e. are due to the light shift of the dipole trap. The shifts of the minima to the  $T = 0$  resonances (dotted lines) are as g.e. due to the thermal shift.

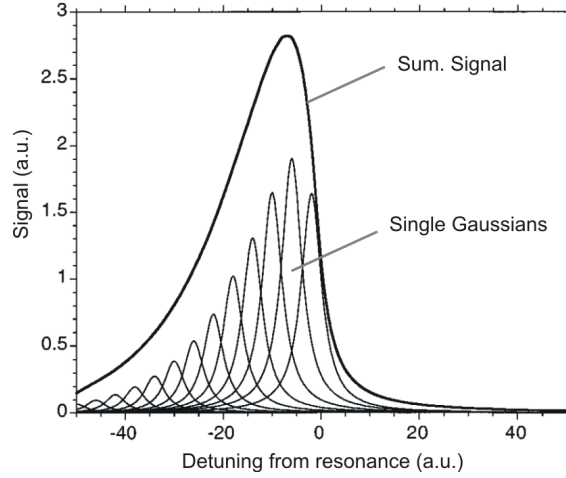


Figure 2.13: Schematic plot of the summation of Gaussians, weighted and shifted due to the thermal distribution. Taken from [89].

Therefore we describe the line shape as

$$\beta_{\epsilon}(\Delta, T) = \sum_i \beta_D(\Delta, \epsilon) e^{\frac{-\epsilon_i}{k_B T}} \cdot \frac{\sqrt{\epsilon_i}}{(k_B T)^{3/2}} \cdot \delta\epsilon, \quad (2.5)$$

where  $\delta\epsilon$  is the chosen energy resolution. For the fit presented in fig. 2.12, the number of summands was chosen to be  $i = 50$  at an increment of  $k_B T/5$ .

The two fitted lines represent temperatures of  $1.0 \mu\text{K}$  and  $0.5 \mu\text{K}$  and Gaussian FWHMs of  $42(7)$  kHz and  $18(5)$  kHz, respectively. These temperatures agree fairly well with the temperatures estimated from the trap depths. Additional time-of-flight measurements for the deep trap yielded  $1.1(1) \mu\text{K}$ . From the temperatures, one calculates due to Doppler broadening a Gaussian FWHM of  $38$  kHz and  $27$  kHz respectively in fair agreement with the fit.

From the fit, we extrapolated to the positions of the resonances at  $T = 0$ , which are indicated in figure 2.12 by dotted lines. Besides the thermal shift, the measured frequencies of the PA resonances are also shifted by the ac-Stark shift from the dipole trap laser beams, operating at a wavelength of  $1032$  nm. The unperturbed line position (dash-dotted line) was determined by linear extrapolation to zero dipole-trap depth. This extrapolation is in good agreement with a linear extrapolation using a Gaussian  $\beta(\Delta)$  to fit the experimental data, where the asymmetry due to collision energy is not taken into account and the thermal shift as well as the light shift of the dipole trap were corrected simultaneously (see section 2.4.3). Hence, this advanced fit was not performed for each vibrational state and justifies a simplified analysis by

single Gaussian shapes linearly extrapolated to  $P = 0$ . This detailed model<sup>10</sup> allows to experimentally determine the absolute value of the thermal shift and compare it to theoretical models. In this way the thermal shift was determined experimentally to be 20 kHz for  $T = 1.0 \mu\text{K}$  and 10 kHz for  $T = 0.5 \mu\text{K}$ .

Theoretically, the center of gravity of the line can be calculated from equation 2.4 by

$$\langle E \rangle = \frac{\int_0^\infty \epsilon^{3/2} e^{-\frac{\epsilon}{k_B T}} d\epsilon}{\int_0^\infty \epsilon^{1/2} e^{-\frac{\epsilon}{k_B T}} d\epsilon}, \quad (2.6)$$

where  $\epsilon$  is the thermal energy. Using the gamma-function  $\Gamma(x) = \int_0^\infty t^{x-1} e^{-t} dt$  and the substitutions  $t = \epsilon/(k_B T)$  with  $x = 5/2$  and  $x = 3/2$ , the average frequency shift is given by

$$\langle E \rangle = \langle h \cdot \Delta \rangle = k_B T \frac{\Gamma(5/2)}{\Gamma(3/2)} = 3/2 k_B T, \quad (2.7)$$

leading to 20 kHz for  $T = 1 \mu\text{K}$  and 10 kHz for  $T = 0.5 \mu\text{K}$ , respectively, which is in good agreement with the experimental measurements.

## 2.4.2 Doppler broadening and temperature

Besides the molecule-specific broadening in atomic and molecular physics, spectral lines are broadened due to the Doppler effect caused by a temperature dependent distribution of velocities of the atoms or the center of mass of the molecule. Therefore the broadening depends on the frequency of the spectral line, the mass of the absorbing particle and temperature.

The Doppler full-width half-maximum (FWHM) is given by

$$\Gamma_{Doppler} = |\vec{k}| \cdot \sqrt{\frac{k_B T}{M_{2Ca}}} \cdot \sqrt{2 \cdot \ln(2)}, \quad (2.8)$$

where  $M_{2Ca} = 2 \cdot m$  is the mass of a  $\text{Ca}_2$  molecule. The Doppler effect leads to a Gaussian line shape and entails no shift of the resonance.

The photoassociation measurements were performed for two different trap depths of the dipole trap. The temperature was assumed to scale linearly with the trap depth. For dipole trap configurations of 1.0/0.6 W (horizontal beam/tilted

<sup>10</sup>Where the fit allows determination of the  $T = 0$  resonance, shifted only by the light field.

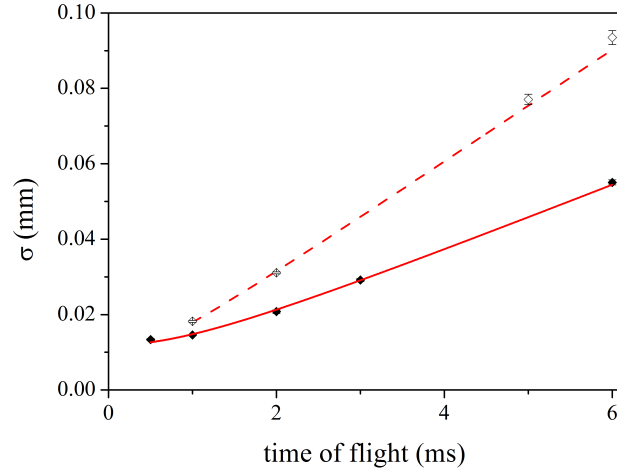


Figure 2.14:  $1/\sqrt{e}$ -widths  $\sigma$  of the atomic cloud as function of time-of-flight. The empty diamonds show the measurements for the dipole trap configuration 1.0/0.6 W (horizontal beam/tilted beam) and the filled diamonds for half the power (0.5/0.3 W), respectively. The lines show theoretical fits based on equation 2.9. The dashed line represents trap depth at power 1.0 W in the horizontal beam and 0.6 W in the tilted beam leading to temperature of  $T = 1.07(4) \mu\text{K}$ . The solid line represents the fit for half the amount of trap depth leading to an estimated temperature of  $T = 0.38(2) \mu\text{K}$ .

beam) and 0.5/0.3 W, respectively, this assumption was checked by time-of-flight (TOF) measurements.

To determine the temperature, the density distribution along two axes was calculated from absorption images. For an initial thermal distribution after a given time-of-flight, the distribution is Gaussian. The time evolution of this Gaussian's  $1/\sqrt{e}$  width is given by:

$$\sigma(t) = \sqrt{\sigma_0^2 + \frac{k_B T}{m} \cdot t^2}, \quad (2.9)$$

where  $t$  is the time-of-flight,  $T$  the temperature,  $k_B$  the Boltzmann constant,  $m$  the atomic mass, and  $\sigma_0^2$  the root mean square (rms) radius of the atomic cloud at time  $t = 0$ . The maximum expansion time results from the limited field of view of the CCD camera. The temperature was determined from the vertical expansion of the cloud, since in the horizontal axis – especially for short times of flight – a background of remaining atoms in the horizontal arm of the dipole trap leads to an overestimation of the expansion along this axis (see fig. 4.8).

The TOF measurements both trap depth configurations are shown in figure 2.14. The lines represent theoretical fits based on equation 2.9. The temperatures

estimated from the fits are  $T = 1.07(4) \mu\text{K}$  for 1.0/0.6 W (dashed line) and  $T = 0.38(2) \mu\text{K}$  for 0.5/0.3 W (solid line), respectively. The corresponding FWHM are  $\gamma_{\text{Doppler}} \approx 37.8 \text{ kHz}$  ( $T = 1.07(4) \mu\text{K}$ ) and  $\gamma_{\text{Doppler}} \approx 22.5 \text{ kHz}$  ( $T = 0.38(2) \mu\text{K}$ ), respectively.

### 2.4.3 Measurement corrections

Besides the correction for the temperature dependent relative kinetic energy, the light shifts, the photon recoil and the quadratic Zeeman effect have to be taken into account.

The photon recoil energy for a  $\text{Ca}_2$  molecule is  $\hbar^2 k^2 / 2M_{2\text{Ca}} = h \cdot 5.8 \text{ kHz}$  for a 657 nm transition, where  $M_{2\text{Ca}}$  is the molecular mass. Since we have to measure the eigenfrequency of the ULE resonator relative to the atomic transition in a second step in order to determine the binding energy of the observed resonances, we have to correct for the atomic photon recoil later. It is 11.6 kHz leading to a relative energy shift of  $\Delta E/h = 5.8 \text{ kHz}$  because of the ratio 2 between atomic and molecular mass.

In order to avoid broadening due to an imperfectly compensated magnetic field the binding energy of the  $M = 0$  level was measured in the presence of a magnetic field. This level is not affected by the linear Zeeman effect but by the quadratic Zeeman effect. This effect will be discussed in a later section describing the measurement of the Zeeman splittings. The model of the molecular potentials which will be presented at the end of this chapter allows a calculation of the corrections which have to be applied to the binding energy of the  $M = 0$  level for the corresponding field strengths. These corrections are presented in table 2.2 on page 37. The uncertainty of this correction was estimated with respect to the accurateness of the coupled channel model and the uncertainty of the  $B$ -field strength (see later sections).

According to equation 2.7 the average thermal shift<sup>11</sup> depends linearly on the temperature. To determine the molecular light shift<sup>12</sup> from the dipole trap laser beams and the thermal shift, which is not accounted for if  $\beta(\Delta)$  is assumed to be Gaussian, we additionally measured the resonance position of each PA line at half

<sup>11</sup>As thermal shift we denote the shift due to asymmetry of the line shape because of the relative kinetic energy of the two colliding atoms [47].

<sup>12</sup>As molecular light shift we denote the dipole trap induced light shift to the molecular PA resonances in order to distinguish it from the light shift of the dipole trap to the atomic resonance, which we denote as atomic light shift.

the amount of dipole trap depth and extrapolated to the unperturbed resonance at zero trap depth. We assume that evaporation to half the trap depth results in half the temperature. Time-of-flight measurements and temperatures derived using the fit algorithm, including the thermal broadening presented before, confirm this assumption, since they are in fair agreement.

For the PA resonances  $v' = -1$  in the potentials  $a$  and  $c$  the dipole trap power was 0.6(0.3) W in the horizontal beam and 1.6(0.8) W in the tilted beam for full (half) trap depth. For more deeply bound PA resonances the dipole trap power was 0.6(0.3) W in the horizontal beam and 1.0(0.5) W in the tilted for full (half) trap depth. The measurements at both dipole trap depths were performed with the same PA laser light intensity to avoid different contributions of the ac-Stark shift due to the PA inducing laser light.

Assuming a linear dependence of light shift on trap depth, including contribution due to kinetic collision energy, leads to the corrections presented in table 2.2, line labeled by DT.

The uncertainties of the light shift and temperature corrections in the dipole trap are given by two effects: The uncertainty of the linear extrapolation given by the fit and the deviations of the temperature relative to the linear assumption.

Assuming the temperature and the light field-induced ac-Stark shift to scale linearly with the trap depth, this leads to the unperturbed resonance  $\nu_0$  extrapolated from two measurements is given by

$$\nu_0 = 2 \nu_{1/2} - \nu_1, \quad (2.10)$$

where  $\nu_{1/2}$  is the resonance frequency measured for half trap depth relative to the full trap depth, where the resonance frequencies  $\nu_1$  were measured. The uncertainty of this linear extrapolation  $\sigma_0$  due to frequency uncertainties  $\sigma_1, \sigma_{1/2}$  as given by the atom loss fit uncertainties reads

$$\sigma_0 = \sqrt{4 \cdot \sigma_{1/2}^2 + \sigma_1^2}. \quad (2.11)$$

at full or half trap depth, respectively.

The uncertainty of the dipole trap power and therefore that of the dipole trap intensity was measured to be less than 1% and thus does not contribute significantly to the total uncertainty. According to TOF measurements (see fig. 2.14) the assumption of linear temperature scaling with the trap depth is not perfectly true. Since the

beam waists of the two, dipole trap beams differ by a factor of two a change in light intensity can lead to a changed trap geometry and hence to a different temperature.

With respect to the deviations of TOF-determined temperatures from the fit results for the temperatures presented before, we assume an uncertainty in TOF-derived temperatures for both trap depths of  $0.1 \mu\text{K}$ . In order to accommodate this contribution to the frequency determination uncertainty, the average thermal shift is given by equation 2.7. This leads to an additional frequency uncertainty of the linear extrapolation of  $4.5 \text{ kHz}$ .

In addition to the ac-Stark shift due to the dipole trap the PA lines are also influenced by the ac-Stark shift from the PA spectroscopy laser (see figure 2.15). In order to determine this ac-Stark shift, the PA resonance loss spectra were measured for several PA light intensities<sup>13</sup>. For more deeply bound states, higher PA intensities were chosen in order to achieve a good signal-to-noise ratio. The PA light shifts, their corrections and their uncertainties derived from the linear fit are shown in table 2.2 for the vibrational states  $v' = -2; -3$  in potential  $a$  and  $c$ , line labeled in PA. For the most weakly bound state  $v' = -1$  in potential  $a$  and  $c$ , due to a stronger coupling a good signal-to-noise ratio was achieved for PA intensities, for which no light shifts was resolvable ( $< 2 - 3 \text{ kHz}$ ) since measurements at intensities of  $I \approx 6 \text{ mW/cm}^2$  and additional measurements at intensities of up to  $I = 0.6 \text{ W/cm}^2$  did not show any resolvable light shift. Therefore the measurements for  $v' = -1$  do not require this correction, and a possible small light shift was taken into account for the estimated measurement uncertainty.

The uncertainty of the PA light shift correction is given by the fit uncertainty of the linear extrapolation, including the loss signal fit uncertainty for each measurement (see line shape discussion), and a non-systematic random error in the PA light intensity determination. The PA light intensity the atoms are experiencing also depends sensitively on the laser beam alignment. Furthermore, there is an uncertainty in the intensity determination from light power.

The intensity of the PA light experienced by the atoms was determined from the measured applied light power. The beam waist of the PA-inducing laser was measured by a beam-view camera to be  $42 \mu\text{m}$ . The adjustment was optimized by maximizing the induced atom loss. From the adjustment uncertainty an average beam waist of  $w \approx 50 \mu\text{m}$  was estimated. The width of the atom distribution in

---

<sup>13</sup>Neglecting the third or higher orders the perturbation theory leads to a linear dependence of the ac-Stark shift on the light intensity.

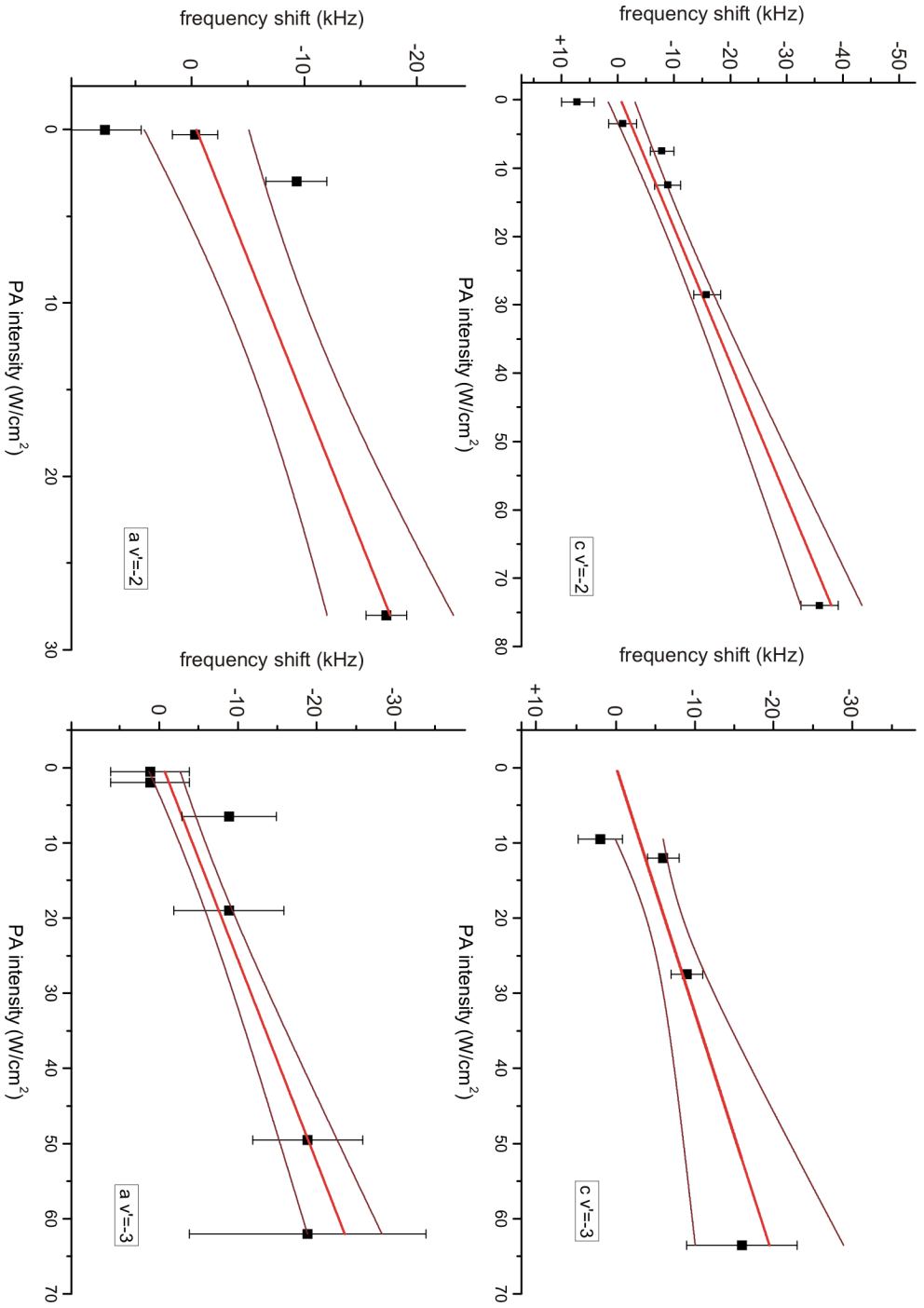


Figure 2.15: Frequency shifts of the PA resonances measured as function of PA inducing light intensity and including fit uncertainty of each loss signal for the  $v' = -2$ ,  $-3$  states in the potentials  $a$  and  $c$  relative to the unshifted resonance. The red curves show the linear approximation to zero light intensity. The brown curves show  $1\sigma$  deviation estimated from the linear fits.

state $v'$ $\Omega$	-1 0	-1 1	-2 0	-2 1	-3 0	-3 1
molecular recoil shift	-6	-6	-6	-6	-6	-6
atomic recoil shift	12	12	12	12	12	12
quadratic Zeeman effect	30 (1)	-17 (1)	6 (0)	-13 (1)	2 (0)	-11 (1)
PA light shift	0(3)	0(2)	15(1)	15(1)	17(2)	9(3)
DT molecular light shift	-80(6)	-82(6)	-26(7)	-36(12)	-42(6)	-60(6)
DT atomic light shift	122(2)	122(2)	110(21)	0(5)	0(4)	0(5)

Table 2.2: Corrections with uncertainties in brackets applied to the measured line positions at high dipole trap power for the  $c\ 0_u^+$  and (a,c)  $1_u$  states to obtain the binding energies  $h\nu$ . The correction of the quadratic Zeeman effect was calculated for  $B = 0.285$  mT. The molecular light shift including thermal shift of 20 kHz. All frequency values are given in kHz. The sign is given relative to the absolute light frequency.

the dipole trap is on the order of a few  $\mu\text{m}$ . From the beam profile camera pictures an assumed Gaussian intensity for the radial beam profile is justified. Thus the intensity  $I$  of the laser the atoms experience is

$$I = \frac{2P}{\pi w^2}, \quad (2.12)$$

where  $I$  is the peak laser intensity,  $P$  the laser power, and  $w = 50\ \mu\text{m}$  the average beam waist.

The uncertainty of the linear extrapolation to the unperturbed resonance at zero light intensity of the PA laser is given by the linear fit (see figure 2.15). The overall uncertainty of the unperturbed resonance is therefore derived from the statistical contributions of the frequency uncertainty for each intensity, as given by the fit uncertainties of the atom loss signal, the statistical uncertainty in the PA light intensity determination and the linearity of the fit. The resulting uncertainties in frequency of the unperturbed PA resonances contributing to the total uncertainty are shown in table 2.2. Since both effects remain constant in each measurement run, they are irrelevant to the linear extrapolation of the unperturbed resonance.

Besides the uncertainties of the PA resonance frequency determination, the uncertainty of the determination of the atomic resonance frequency, relative to the resonator, also contributes to the total uncertainty, as does the relative uncertainty of the eigenfrequency of the resonator itself for both measurements.

To determine the atomic resonance frequency, the atom loss spectra signal were fitted by Gaussians. Depending on the signal-to-noise ratio for each measurement a fit uncertainty is given, contributing to the total uncertainty.

state		binding energy (GHz·h)
$v'$	$\Omega$	
-1	0	-0.308700(8)
-1	1	-0.982977(7)
-2	0	-4.649209(22)
-2	1	-7.411933(13)
-3	0	-17.857276(8)
-3	1	-24.539435(8)

Table 2.3: Molecular energies with respect to the atomic asymptote of the experimentally observed PA resonances corrected for light, kinetic energy and recoil shifts and their uncertainties.

The atomic resonance frequency relative to the eigenfrequency of the resonator was measured for every PA resonance by spectroscopy either in ballistically expanding clouds of free atoms or atoms stored in the dipole trap. In both cases the atomic photon recoil shift was taken into account as well.

For the most weakly bound states ( $v' = -1$ ), the atomic reference spectra are measured in the dipole trap only due to technical reasons. Thus, the light shift of the atomic resonance due to the dipole trap had to be corrected for these states. Here, we also extrapolated the light shift of the atomic resonance by a second measurement at half dipole trap intensity and linearly extrapolated to zero intensity. The uncertainty of this correction is the root mean square (rms) sum of the fit uncertainties of the atom loss signal for both dipole trap powers. The non-linearity of the intensity determination was measured to be less than 1% and therefore not taken into account.

The atomic spectra for the measurements of the  $v' = -2$  state in potential  $c 0_u^+$  were measured for a trap powers of 0.6 W in the horizontal beam and 1.2 W in the tilted beam. The unperturbed atomic resonance was estimated by extrapolating the measured light shift for beam intensities of 0.6 W and 1.6 W to 0.6 W and 1.2 W, respectively, by applying the ratio of the calculated trap depth for both beam power configurations on the experimentally determined light shift of 122 kHz for beam powers of 0.6 W and 1.6 W [62]. The uncertainty is dominated by the uncertainty of the light shift determination for the states  $v' = -1$  with an additional uncertainty of estimated 20% in intensity due to trap beam adjustment. For the calculation an uncertainty of 3 kHz was estimated by comparison of experimental data to theoretical predictions based on trap frequency measurements.

For more deeply bound molecular states, the eigenfrequency of the ULE resonator relative to the atomic asymptote was measured in absence of the dipole trap

laser light and thus does not require a light shift correction. The uncertainties for these measurements are therefore given by the fit uncertainty of the spectra. The resulting corrections are shown in table 2.2 (last line).

Table 2.3 shows the binding energies measured for the six most weakly bound states in potential  $a$  and  $c$ , including their total uncertainties<sup>14</sup>.

The total uncertainty of the determined binding energies  $\sigma_{total} = \sqrt{\sum_i \sigma_i^2}$ , summing over each uncertainty contribution  $\sigma_i$  mentioned before, was calculated under the assumption that all contributions are independent from each other.

## 2.5 Comparison of the derived binding energies to the predictions

The comparison of the observed resonances (table 2.3) to the theoretical predictions given by Appel [62] (see also table 2.1) clearly shows that the contribution due to molecular rotation, which can be expressed in this picture by effective potential terms (compare [58])  $V_{rot}(0_u) = \frac{\hbar^2}{2\mu R^2} \cdot J(J+1)$  and  $V_{rot}(1_u) = \frac{\hbar^2}{2\mu R^2} \cdot J((J+1)+2)$ , respectively, cannot be neglected, since method (4) was the most accurate prediction. Furthermore, the  $C_8$  coefficient of the molecular potential has a significant contribution and cannot be neglected either. Since three parameters ( $C_6$ ,  $C_8$  and the phase of the wavefunction) have to be fitted for the description of both molecular potentials at large internuclear separations ( $C_3$  can be calculated from the measured lifetime of the  $^3P_1$  state), the knowledge of three binding energies for each potential is not sufficient for a detailed description of the corresponding potentials. Therefore, we also investigate the coupling behavior of the angular momenta as determined by measurements of the gyromagnetic ratio.

## 2.6 Angular momentum coupling in the Ca molecule

For an approaching pair of atoms at certain internuclear separation, various molecular interactions become comparable or larger than the particular couplings within the individual atom. Thus, we have to introduce different good quantum numbers

---

<sup>14</sup>Note: These binding energies differ from the binding energies published in [90] since there they have not yet been corrected for the quadratic Zeeman effect.

e.g. related to the interatomic axis, which is the relevant symmetry axis of a diatomic molecule [91]. For an approximate description depending on the relative size of the various interactions in the Hamiltonian, one chooses a Hund's coupling case, which is summarized briefly in the following section. Which interaction is of relevance, however, and which Hund's case hence is suited best, depends strongly on the internuclear separation.

Each of these Hund's cases has a different set of quantum numbers form basis of Hilbert space, because they correspond to approximate constants of motion of a molecular state, describing the coupling behavior of the angular momenta. Therefore, we generally expect a different coupling behavior and a different gyromagnetic ratio (commandly called  $g$ -factor) in molecules depending on their ro-vibrational molecular state.

Initially, the gyromagnetic ratios of both relevant molecular potentials were used in order to intuitively identify the corresponding potential for each of the observed states. States from  $\Omega = 0$  (see Hund (c)) will have a small Zeeman effect, but those from  $\Omega = 1$  a significant one, as explained in section 2.7 below.

## 2.7 Hund's coupling cases

In a non-rotating molecule, the internuclear axis is the axis of quantization and thus the projections of the atomic quantum numbers on this axis appear as quantum numbers for the molecular states. The relative strength of their coupling to this axis determines the best-suited set of quantum numbers, systematized in Hund's coupling cases [92]. For our case only the cases (a), (c) and (e), visualized in figure 2.16, are of interest and will be explained in the following.

### 2.7.1 Hund's case (e)

In Hund's case (e), the electrostatic coupling to the molecular axis at very large internuclear separations is extremely weak. Thus the atomic angular momentum  $\vec{J}_a$  does not precess around the internuclear axis. Therefore  $\vec{J}_a$  and the rotational angular momentum of the dimer  $\vec{R}$  couple to a total molecular angular momentum  $\vec{J} = \vec{J}_a + \vec{R}$  (see figure 2.16) giving exact quantum numbers for the idealized case (e).

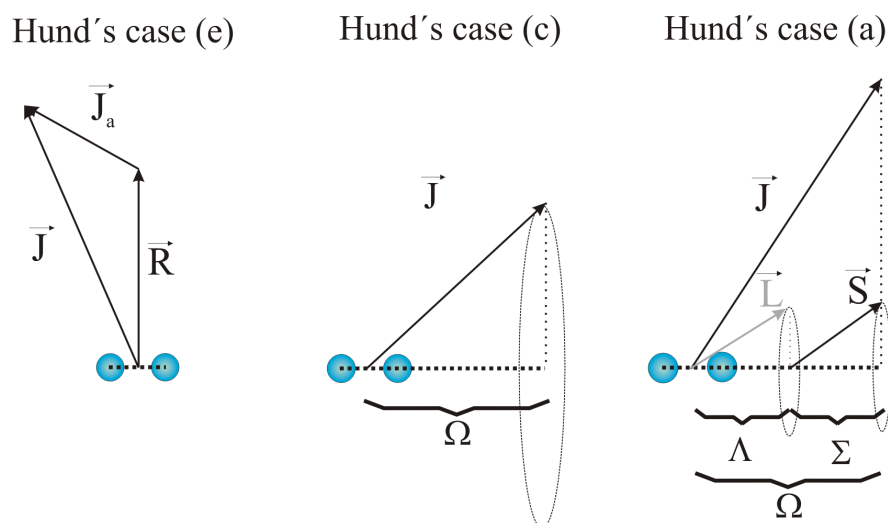


Figure 2.16: Schematic drawing of the angular momenta coupling behavior in a dimer for the Hund's cases (e), (c) and (a). In Hund's case (e), the total atomic angular momentum  $\vec{L} + \vec{S} = \vec{J}_a$  couples directly with the rotation of the molecule  $\vec{R}$  to form the total molecular angular momentum  $\vec{J}$ . In Hund's case (c), the projection to the internuclear axis  $\Omega$  of  $\vec{J}_a$  allows only total  $\vec{J}$  with that fixed projection. In Hund's case (a), the interatomic interaction couples  $\vec{L}$  strongly to the axis and leads to its projection  $\Lambda$ .  $\vec{S}$  is coupled weakly to  $\vec{L}$  and its projection  $\Sigma$  is an additional quantum number.

### 2.7.2 Hund's case (c)

In Hund's case (c), the binding energy at intermediate internuclear separation is increased but still not strong enough to break the  $L - S$ -coupling, since the spin-orbit coupling represented by the coupling constant  $A$  is relatively large compared to the molecular potential energy. Thus the projection to the molecular axis  $\Omega$  of the coupled orbital and spin angular momenta is a good quantum number and becomes also the projection of the total angular momentum  $J$  in the molecular fixed frame. The states are denoted  $\Omega_{g/u}^{+/-}$ , where  $g/u$  is the *gerade* or *ungerade* parity of the electronic wavefunction when inverting the electronic space only.  $+/-$  denotes the symmetry for  $\Omega = 0$  states when mirroring the wavefunction on a plane which contains the internuclear axis.

### 2.7.3 Hund's case (a)

At short internuclear separations the Coulomb and exchange interatomic interactions are large compared to the spin-orbit interaction and thus strong enough to break the  $L - S$ -coupling, i.e.  $\vec{L}$  now precess around the internuclear axis. Due to

the strong anisotropic electric field of the two nuclei,  $\langle \vec{L}^2 \rangle$  is thus no longer a conserved quantity, but its projection to the internuclear axis  $\Lambda$  is. Because of the weak spin-orbit coupling, the spin quantum number  $S$  as well as the projection of  $\vec{S}$  to the internuclear axis  $\Sigma$  are good quantum numbers. The sum of these projections is  $\Lambda + \Sigma = \Omega$  and only total angular momenta  $\vec{J}$  which have a projection onto the molecular axis equal to  $\Omega$  are allowed. In Hund's case (a) the molecular states are denoted  $^{2S+1}\Lambda_{\Omega_{g/u}}^{+/-}$  with the same symmetry quantum numbers *gerade/ungerade* and (for  $\Lambda = 0$ )  $+/-$  as described previously, but here for  $\Lambda = 0$ .

In contrast to atomic physics, where the states of angular momenta  $L = 0, 1, 2, \dots$  are denoted as  $S, P, D, \dots$ . However, the molecular states with  $\Lambda = 0, 1, 2, \dots$  are denoted by Greek letters ( $\Sigma, \Pi, \Delta, \dots$ ), where  $\Sigma$  is not to be confused with the projection of  $\vec{S}$  to the internuclear axis  $\Sigma$ .

## 2.8 Theoretical predictions for the $g$ -factors and molecular state identification

For the situation investigated here, only the cases (a), (c) and (e) are of relevance, and the theoretical predictions for the  $g$ -factor in these cases will be calculated.

For an atom in  $L - S$ -coupling the Landé  $g$ -factor is given by [68]

$$g_J^{atom} = 1 + \frac{J(J+1) + S(S+1) - L(L+1)}{2J(J+1)}, \quad (2.13)$$

where  $J$  is the total angular momentum of the atom,  $S$  the spin quantum number, and  $L$  the orbital quantum number. For the atomic state  $^3P_1$ , the Landé factor is therefore  $g_J^{atom} = 1.5$ . Measurements of the  $^3P_1$  state with  $^{40}\text{Ca}$  yield  $g_J^{atom}(^3P_1) = 1.5010829(28)$  [93]. This value is also valid in Hund's coupling case (e) if the quantization is determined by  $\vec{J}_a$  rather than the the total angular momentum  $\vec{J}$  and the rotational Zeeman contribution can be neglected.

The  $g$ -factor in Hund's case (a) is given by [68]

$$g^a = \frac{|\Lambda + 2\Sigma| \cdot |\Lambda + \Sigma|}{J(J+1)}, \quad (2.14)$$

which results in  $g^a(^3\Sigma_{1u}) = 1$  and  $g^a(^3\Pi_{0+}) = 0$  for  $J = 1$ .

Following the treatment<sup>15</sup> presented in [68]<sup>16</sup>, the  $g$ -factor in Hund's case (c) is given by

$$g^{(c)} = g_J^{atom} \frac{\Omega^2}{\sqrt{J(J+1)}}, \quad (2.15)$$

where  $\Omega$  is the projection of the total atomic angular momentum  $J_a$  on the internuclear axis. This leads to  $g^{(c)}(1_u) = 0.75$  and  $g^{(c)}(0_u^+) = 0$  for  $J = 1$ .

These theoretically predicted  $g$ -factors differ significantly for both molecular potentials.

In Hund's case (c), which is usually used at large internuclear separations, the potentials are denoted as  $0_u^+$  and  $1_u$ , where 0 and 1 are the possible values of  $\Omega$  for an atomic pair, e.g.  $^1S_0 + ^3P_1$  as in our present case. The Zeeman splitting is characterized by the  $g$ -factor, which can be calculated in Hund's case (c) [68] by equation 2.15, where  $J$  is the total angular momentum of the molecule,  $J_a = L + S$  the total molecular electronic angular momentum, and  $g_{J_a}^{atom}$  the atomic Landé factor. At the low temperature of our experiment ( $\mu\text{K}$  regime), only s-wave scattering is expected for bosons<sup>17</sup> and thus only states with total angular momentum  $J = 1$  can be excited by a single photon. This results in  $g^{(c)}(1_u) = 0.75$  and  $g^{(c)}(0_u^+) = 0$  for  $J = J_a = 1$ .

To measure the splitting a magnetic field was applied, and the  $\Delta M = \pm 1, 0$  spectra for each PA resonance were measured. The magnetic field of  $B = 0.285(7)$  mT was generated by two coils in Helmholtz configuration with a current of  $I \approx 5.7$  A. The coils have been characterized in [79].

The three  $M$  components were observed in a single atom loss spectrum with constant PA laser intensity, exposure time and trap configurations. The atom losses were also described by  $\dot{N} = -\beta N^2$ , where the loss rate was given by:  $\beta = \beta_{+1}(\Delta_{+1}) + \beta_0(\Delta_0) + \beta_{-1}(\Delta_{-1})$ , where  $\beta_M$  is the individual loss rate for each component at resonance frequency  $\Delta_M$ . Since such a measurement took several minutes a possible systematic drift of the background ( $N_0$ ) was taken into account as a fitted linearly varying background.

The magnetic splitting of the molecular states was used to distinguish the experimentally observed  $a \ ^3\Sigma_u^+$  and  $c \ ^3\Pi_u$  states.

<sup>15</sup>Private communication Dr. Uwe Sterr.

<sup>16</sup>Eq. V.89 and V.90; replace  $\bar{\mu}_w = \Omega \cdot g_{atom} \cdot \mu_0$  and  $\Omega = \Lambda + \Sigma$ .

<sup>17</sup>Due to d-wave rotational barrier on the order of  $m\text{K}$ .

state		$ g_{exp} $
$v'$	$\Omega$	
-1	0	0.276(1)
-1	1	1.074(4)
-2	0	0.147(6)
-2	1	0.901(27)
-3	0	0.081(3)
-3	1	0.843(26)

Table 2.4: Measured molecular  $g$ -factors of the  $c\ 0_u^+$  and  $(a,c)\ 1_u$  states for the atomic asymptote  $^1S_0 + ^3P_1$ .

## 2.9 Experimental results of the Zeeman splitting measurements

To determine the  $g$ -factor (tab. 2.4) from the magnetic splitting the field strength at the position of the atoms was calibrated by measuring the splitting of the  $^3P_1$  atomic transition using the Landé factor  $g_J^{atom}(^3P_1) = 1.5010829(28)$  [93]. The observed splitting of the atomic resonance was 5.99(18) MHz leading to a magnetic field of  $B = 0.285(7)$  mT.

Figures 2.17 and 2.18 show the Zeeman splitting observed experimentally for bound levels of the  $a\ ^3\Sigma_u^+$  ( $\Omega=1_u$ ) and  $c\ 0_u^+$  potentials, respectively, as well as that of the atomic  $^1S_0 - ^3P_1$  transition. For each measurement, the same magnetic field of  $B = 0.285(7)$  mT was applied.

At such a small magnetic field only a linear Zeeman effect was expected. The observed small and unsystematic asymmetries of the Zeeman splittings in the particular triplets were treated as contributions to the uncertainties (see next section). In our setup the PA laser beam is perpendicular to the magnetic field, thus we cannot distinguish between  $\Delta M = \pm 1$  transitions and only the absolute values of the  $g$ -factors could be determined experimentally.

The experimentally observed magnetic splitting of the PA resonances and the fit uncertainties for the atom losses of these scans are shown in table 2.5. For each PA resonance the observed splitting differs significantly from the predictions and cannot be explained by a pure Hund's case.

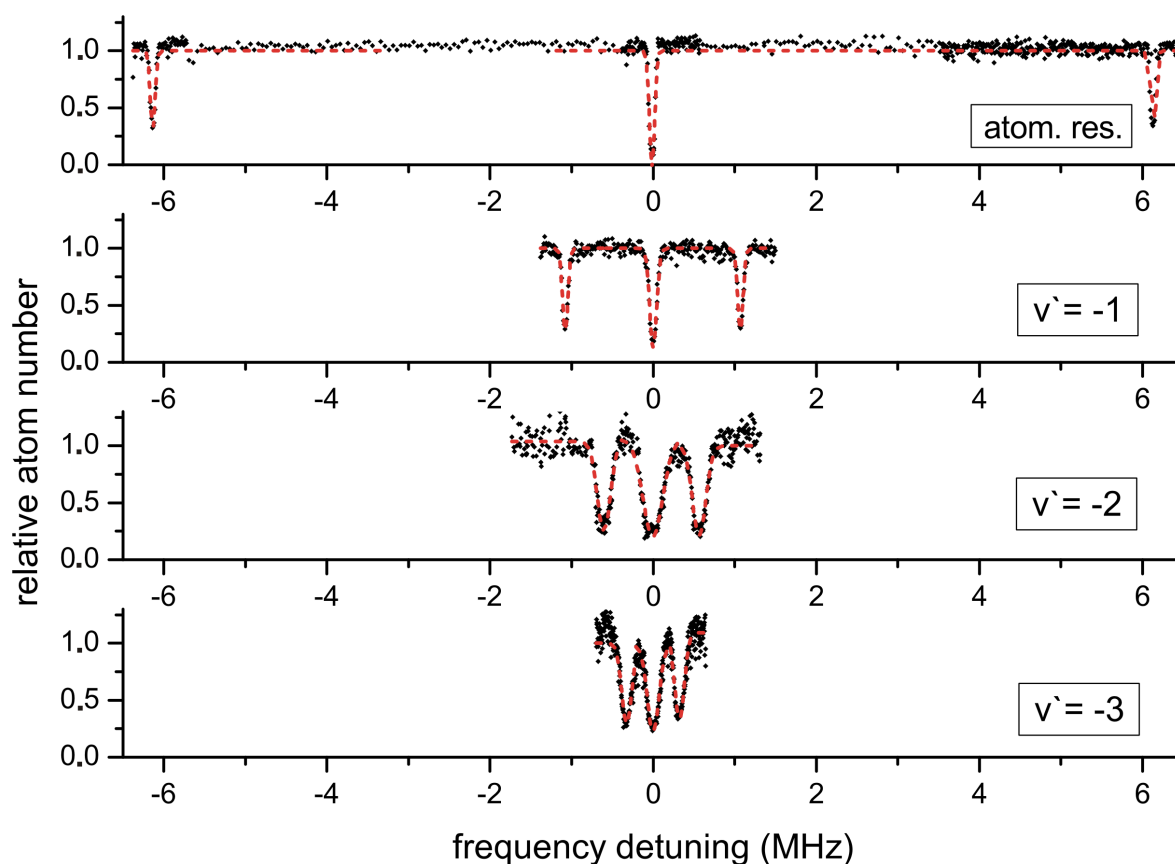


Figure 2.17: Atom number trap loss as a function of the spectroscopy laser frequency relative to the  $M = 0$  component. Shown are the atomic  $^3P_1$  resonance and the Zeeman triplet for the three most weakly bound molecular states in the  $c^3\Pi_u$  ( $\Omega=0_u^+$ ) potential for a magnetic field of  $B = 0.285(7)$  mT. The intensities of the PA laser were  $I(v' = -1) = 4$  W/cm<sup>2</sup>,  $I(v' = -2) = 56$  W/cm<sup>2</sup>,  $I(v' = -3) = 40$  W/cm<sup>2</sup>. The red curves are simulated profiles, as described by eq. 2.3.

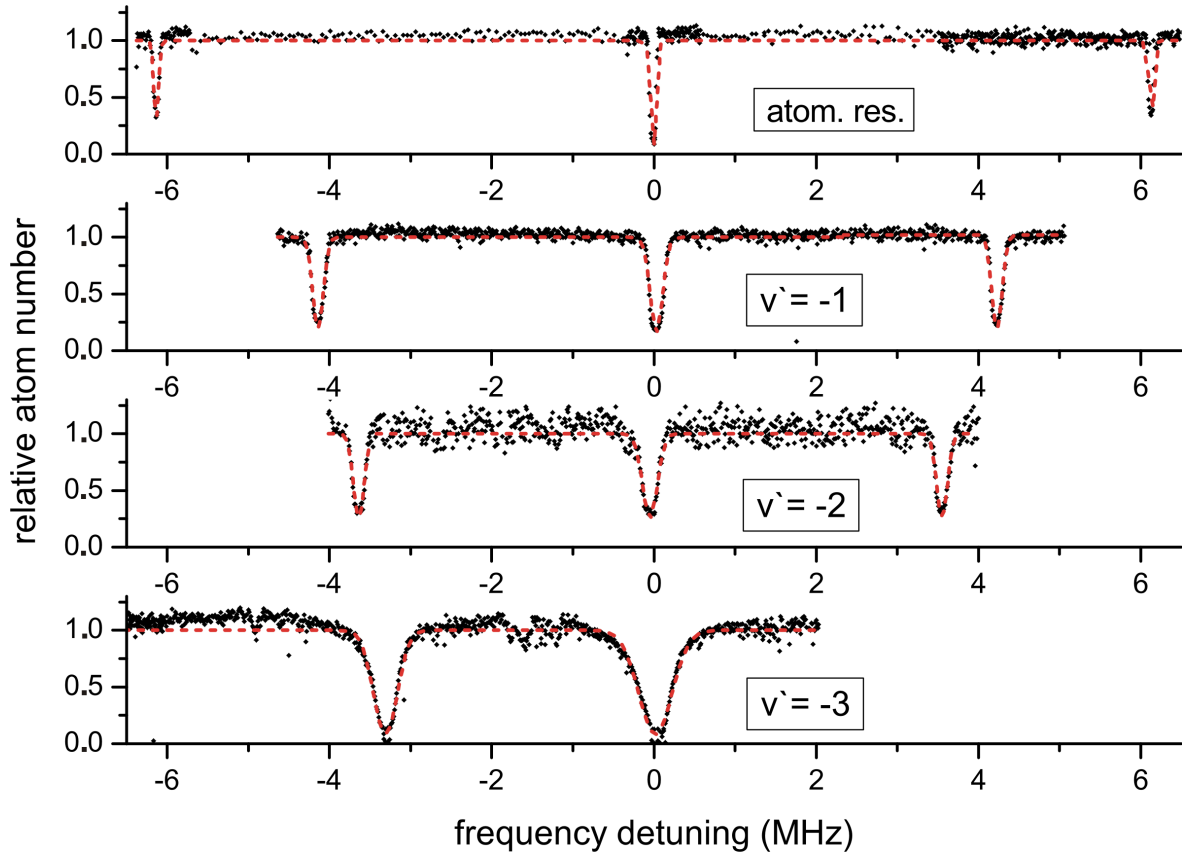


Figure 2.18: Atom number trap loss as a function of the spectroscopy laser frequency relative to the  $M = 0$  component. Shown are the atomic  $^3P_1$  resonance and the Zeeman triplet for the three most weakly bound molecular states in the  $a^3\Sigma_u^+$  ( $\Omega=1_u$ ) potential for a magnetic field of  $B = 0.285(7)$  mT. The intensities of the PA laser were  $I(v' = -1) = 8$  W/cm<sup>2</sup>,  $I(v' = -2) = 56$  W/cm<sup>2</sup>,  $I(v' = -3) = 124$  W/cm<sup>2</sup>. The red curves are simulated profiles, as described by eq. 2.3.

## 2.10 Estimated uncertainty of the $g$ -factors

Three effects dominate the uncertainty of the  $g$ -factor determination for each PA resonance: The uncertainty of the field strength, the asymmetry of the splitting and the fit uncertainty of the atom loss signals.

The Zeeman energy is given by

$$E_Z = \mu_B \cdot g \cdot M \cdot B + \chi_0 \cdot B^2 + \chi_2(M^2) \cdot B^2, \quad (2.16)$$

where  $\mu_B$  is the Bohr magneton,  $g$  the molecular  $g$ -factor,  $M$  the projection of the angular momentum,  $B$  the magnetic field,  $\chi_0$  the scalar susceptibility and  $\chi_2$  the tensorial susceptibility, as a function of  $M$ .

In our coupled channel model (see section 2.11) the Zeeman energies were also taken into account, i.e. the Zeeman effect is no longer treated to first order only. It includes the spin–orbit and the rotational coupling between states  $^3\Sigma$  and  $^3\Pi$ .

The difference between the linear Zeeman splitting and the Zeeman splitting given by the coupled channel model is shown in figure 2.19 for the  $v' = -1$  state in the molecular potentials of the coupled states  $(a)0$  and  $(a, c)1$ .<sup>18</sup> Since due to the corresponding energy differences the off-diagonal coupling in  $J$  is much weaker compared to coupling between the three  $J = 1$  states, the coefficient  $\chi_2(M^2)$  is much smaller compared to  $\chi_0$ . This fact can also be derived from fig. 2.19. Thus, we do not expect an asymmetry due to the quadratic Zeeman effect, but rather a shift of the resonance energy  $\Delta E = \chi_0 \cdot B^2$  of all  $M$  states. These shifts were taken into account as corrections for the determination of the binding energy.

Since no asymmetry due to the quadratic Zeemann effect is expected, the mean value of the splitting was derived for the evaluation and an observed asymmetry was taken into account in the uncertainty evaluation.

The Zeeman splittings of the PA resonances show an asymmetry between the  $M = -1, 0$  and the  $M = 0, 1$  splitting of up to 40 kHz. The exact amount of asymmetries is shown in table 2.5. The observed asymmetries could be due to tensor and vector light shifts caused by the dipole trap and the PA spectroscopy light. Possible  $M$ -dependent light shifts from the PA laser will be discussed in more detail in the following section.

The polarization of the PA spectroscopy laser light was adjusted in such a way

---

<sup>18</sup>Calculated by Prof. Eberhard Tiemann.

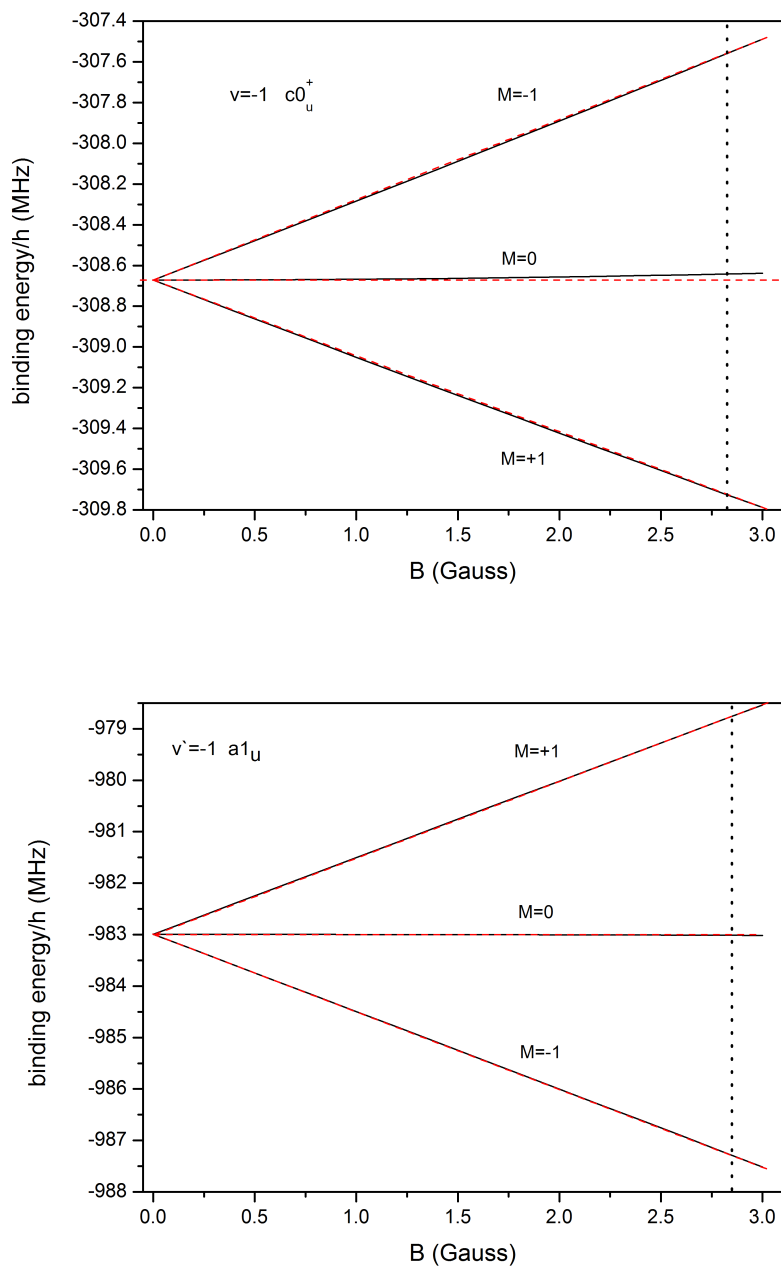


Figure 2.19: Zeeman splittings for the  $v' = -1$  states in potentials  $c$  and  $a$ . The black lines shows the theoretical predictions for the Zeeman effect as a function of the strength of the external magnetic field given by the coupled channel model. The red dashed line shows the prediction for a pure linear Zeeman effect. The dotted line represents the fields strengths of the typically applied magnetic field.

state		$\Delta M(-1, 0)$	$\Delta M(0, 1)$	$\delta$
$v'$	$\Omega$	$h \cdot \text{kHz}$	$h \cdot \text{kHz}$	$h \cdot \text{kHz}$
-1	0	1 078(4)	1 072(3)	-6
-1	1	4196(1)	4 171(2)	-25
-2	0	600(4)	570(3)	-30
-2	1	3 602(1)	3 589(2)	-13
-3	0	321(2)	325(3)	+4
-3	1	3 360(5)	3 330(8)	-30

Table 2.5: Splitting  $\delta$  between the  $M$  components of the three most weakly bound states  $v' = -1, -2, -3$  in the  $c\ 0_u^+$  and (a,c)  $1_u$  molecular potentials for the atomic asymptote  $^1S + ^3P$  and their asymmetry  $\delta$ . The uncertainty shown here is the fit uncertainty of the spectra.

state		fit uncer.	fit uncer.	fit uncer.	splitting	uncer. of	total uncer.
$v'$	$\Omega$	$M = 0$	$M = -1$	$M = +1$	asymmetry	$B$ -field cal.	$g$ -factor
		kHz	kHz	kHz	kHz	(%)	(1)
-1	0	1.4	3.2	1.0	6.0	<0.1	0.001
-1	1	1.1	1.3	1.5	25.0	<0.1	0.004
-2	0	2.0	3.0	2.2	30.0	3.0	0.006
-2	1	1.7	2.5	3.0	13.0	3.0	0.027
-3	0	1.6	2.5	3.0	4.0	3.0	0.003
-3	1	1.2	5.2	3.0	30.0	3.0	0.026

Table 2.6: Contributions to the uncertainty of the Zeeman-splitting of the  $c\ 0_u^+$  and (a,c)  $1_u$  states for atomic asymptote  $^1S_0 + ^3P_1$ .

that 50% of the laser intensity was driving the transition to the  $M = 0$  component and 25% to the  $M = \pm 1$  states each. Assuming that the "wrong" polarization does not contribute, we expect twice the amount of light shift of the  $M = 0$  state compared to the  $M = \pm 1$  states due to the ac Stark shift.

The magnetic field from the splitting of the atomic transition was not measured for each PA resonance due to technical reasons. From several atomic measurements during the measurement campaign at a constant current of the Helmholtz coils the atomic Zeeman splitting was measured to be 5.99(18) MHz.

Besides the asymmetry and the field strength calibration as dominant contribution to the total uncertainty, the fit uncertainties of the atom loss signal, discussed in the previous sections, have been taken into account for the three components for each PA resonance and are shown in table 2.6.

For the most weakly bound states  $v' = -1$  in both potentials it was possible to measure the atomic Zeeman splitting within minutes after measuring the molecular Zeeman splitting. Several measurements during a day indicate that no change in

the field strength occurred on this time scale. Therefore, the uncertainty in the field strength was neglected. For more deeply bound molecular states, it was not possible to observe the atomic Zeeman splitting simultaneously. The field strength was therefore calibrated several times by measuring of the atomic Zeeman splitting for a given coil current. The uncertainty was determined statistically by measurements of the atomic Zeeman splitting on different days for the same coil current with a from statistics estimated uncertainty of 3 %.

All uncertainties including the resulting total uncertainty of the  $g$ -factors are shown in table 2.6. For the states  $v' = -2, -3$ , the uncertainty is dominated by the contribution of the  $B$ -field calibration. Due to technical reasons this limit can only be overcome if the photo diode is replaced by a different model, allowing detection of beat frequencies in the range 0.5 – 30 GHz. This would allow the observation of the Zeeman splitting of the atomic resonance without significant changes of the experimental setup and thus a  $B$ -field calibration for each PA Zeeman splitting measurements as it was performed for the  $v' = -1$  states using a photodiode for beat frequencies between 0.6 – 1.5 GHz.

## 2.11 Close coupled channel model

The comparison (of the deviation) of the experimentally derived  $g$ -factors to the theoretical predictions based on pure Hund's coupling cases leads to a requirement of an enhanced theoretical model to describe the experimental data. Based on the theoretical model described in section 2.11.2 developed by Eberhard Tiemann, the molecular potential coefficients were determined from the experimental data and allow theoretical predictions for more deeply bound states as well as the involved Franck-Condon densities for the free-bound transition in photoassociation.

### 2.11.1 Experimental deviation from Hund's cases

In a first step, we calculate the classical outer turning points of the observed bound states. The far-range molecular shape depends on the  $C_3$  and  $C_6$  coefficients. For the determination of the classical turning points, we use theoretical predicted  $C_x$  coefficients [63] and the measured binding energies presented in table 2.3.

The binding energy of these states as well as the potential shapes at long range are shown in figure 2.20.

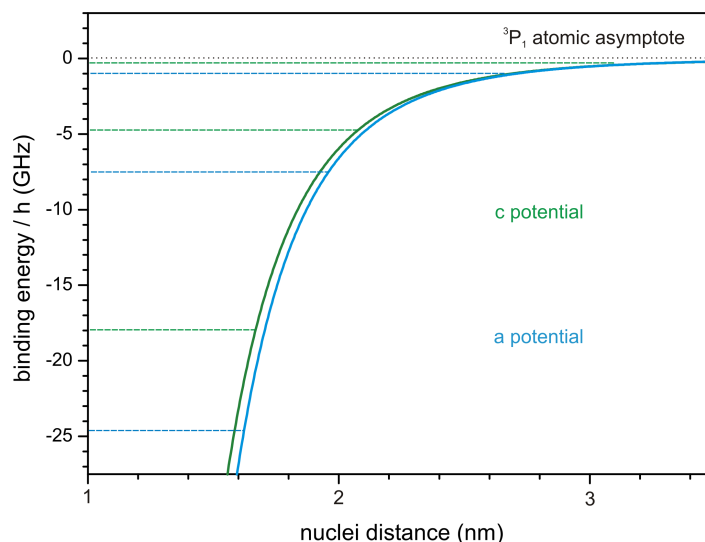


Figure 2.20: Long range potential  $c 0_u^+$  and (a,c)  $1_u$  based on theoretical predicted potential coefficients [63] and the experimentally determined bound vibrational states.

In order to visualize the  $g$ -factor as a function of the internuclear distance  $R$ , the measured effective  $g$ -factors and their corresponding outer potential turning points - derived from the measured binding energies and the theoretical predicted molecular potential coefficients [63] - are shown in fig. 2.21. Hund's cases (a),(c) and (e) are also shown in figure 2.21. At extremely large internuclear distances  $R$ , the  $g$ -factors are in fair agreement to Hund's case (e). The  $g$ -factors for decreasing internuclear distance  $R$  are progressive better described by Hund's case (c).

Since we observe significant Zeeman splitting in all states (also for  $\Omega = 0$ , where it is predicted to be 0 in Hund's case (c)) and the observed splitting cannot be explained by a pure Hund's coupling case, a theoretical model which takes the coupling by spin-orbit and rotational interaction into account is required.

### 2.11.2 Theoretical model

For a theoretical description of the observed energies, the couplings of the states of relevance to each other have to be taken into account. Thus, we describe the eigenfunctions as a superposition of the corresponding states. In equation 2.17, this superposition is shown in the basis of Hund's case (e) basis (and thus well defined by the quantum numbers  $L, S, j, l, J$ )<sup>19</sup>.

<sup>19</sup>where  $l$  denotes the overall molecular rotation,  $L$  the atomic angular momentum,  $S$  the atomic spin angular momentum of the electrons,  $j$  the total electronic angular momentum and  $J$  as the total angular momentum.

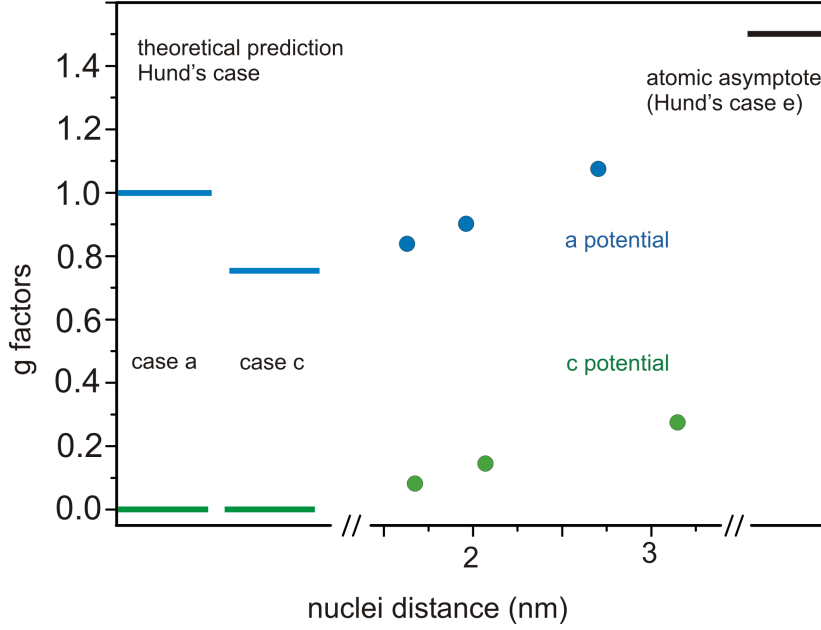


Figure 2.21: Experimentally derived  $g$ -factors of the  $c\ 0_u^+$  and (a,c)  $1_u$  states for atomic asymptote  $^1S + ^3P$  and the theoretical predictions for Hund's cases (a),(c) and (e).

$$\psi = \sum_i |(L, S)j, l, J\rangle_i \cdot \varphi_i(R), \quad (2.17)$$

where  $\varphi_i(R)$  gives the dependence of the internuclear distance  $R$ .

For these states we have to solve the Schrödinger equation  $\hat{H} \cdot \psi = E\psi$ . The potential functions  $U(r)$ , which are diagonal in the basis of Hund (a), ( $^3\Sigma$  and  $^3\Pi$  states) will be transformed to the basis Hund (e) and then the diagonal term of the overall rotation in Hund (e) can be added  $\frac{\hbar^2 l(l+1)}{2\mu R^2}$ .

The Hilbert space in this close coupled channel model is in contrast to a similar model presented in [63] only spanned by molecular states resulting from atomic pairs in quantum states  $^1S_0 + ^3P_1$  and  $^1S_0 + ^3P_2$ . Since in Ca the singlet-triplet coupling is much weaker than in Sr, the coupling to the  $^1S_0 + ^1P_1$  state was included by setting up weak effective dipole-dipole terms in the long range potentials. With respect to the selection rules, only molecular levels with a total angular momentum of  $J = 1$  and parity " - " will be excited by a single photon s-wave photoassociation from the  $^1S_0 + ^1S_0$  ground state. Thus only three molecular states are considered. We chose Hund's case (e) as basis since the spin-orbit and Zeeman interaction are diagonal and the coupling constant and the  $g$ -factors are the atomic quantities.

Thus the molecular states are given by  $|(L, S)j, l, J\rangle_e$ :

$$|(1, 1)1, 0, 1\rangle \quad |(1, 1)1, 2, 1\rangle \quad |(1, 1)2, 2, 1\rangle,$$

In Hund's case (a) the three eigenstates of relevance due to selection rules are given by  $|\Lambda, S, \Sigma, J\rangle_a$ :

$$c|1, 1, -1, 1\rangle \quad c|1, 1, 0, 1\rangle \quad a|0, 1, 1, 1\rangle.$$

All states will be mixed by rotational and spin-orbit coupling. Because we assume a  $C_3$  term for all components of the the  $c$  states the second state  $c|1, 1, 0, 1\rangle$  has a contribution due to dipole–dipole interaction contrary to its correlation to the atomic pair  $^1S_0 + ^3P_2$ . This artificial contribution to the energy of the eigenstates is only on the order of magnitude of the experimental uncertainty and was neglected. All states will be mixed by rotational and spin-orbit coupling. Because we assume a  $C_3$  term for all components of the the  $c$  states the second state  $c|1, 1, 0, 1\rangle$  has a contribution due to dipole–dipole interaction contrary to its correlation to the atomic pair  $^1S_0 + ^3P_2$ . This artificial contribution to the energy of the eigenstates is only on the order of magnitude of the experimental uncertainty and was neglected.

The related molecular potentials are described in Hund's case (a) as  $a^3\Sigma_u^+$  and  $c^3\Pi_u$ . The outer region for internuclear distances  $R_o = 1.2$  nm of these potentials can be described in Hund's case (a) as

$$U_a = -\frac{4C_3^{(0)}}{R^3} - \frac{C_6^{(a)}}{R^6} - \frac{C_8^{(a)}}{R^8}$$

$$U_c = -\frac{2C_3^{(0)}}{R^3} - \frac{C_6^{(c)}}{R^6} - \frac{C_8^{(c)}}{R^8}.$$

The resonant  $C_3$  term (dipole-dipole interaction) was estimated [63, 64] from the lifetime of the  $^3P_1$  state  $\tau = 0.426(19)$  ms [94] and the  $^1S_0 \rightarrow ^3P_1$  transition frequency of 455 986 240 494 144(5.3) Hz [61], leading to  $C_3^{(0)} = 10.72$  cm<sup>-13</sup>.

The potentials for the full Hamiltonian are derived by transforming them from Hund's case (a) to case (e) by using the transformation matrix given in [63].

state		binding energy (GHz/h)		$\delta$	$g$ -factor		$\delta$
$v'$	$\Omega$	exp.	model	(kHz/h)	exp.	model	
-1	0	-0.308700 (8)	-0.308684	-16	0.276 (2)	-0.274	0.002
-1	1	-0.982977 (7)	-0.982984	7	1.074 (4)	1.069	0.005
-2	0	-4.649209 (22)	-4.649238	29	0.147 (6)	-0.147	0.000
-2	1	-7.411933 (13)	-7.411921	-12	0.901 (29)	0.902	0.001
-3	0	-17.857276 (8)	-17.857276	0	0.080 (6)	-0.079	0.001
-3	1	-24.539435 (8)	-24.539436	1	0.838 (26)	0.831	0.007

Table 2.7: Experimentally derived binding energies and  $g$ -factors compared to the binding energies and  $g$ -factors given by the coupled channel model.  $\delta$  is the difference of the measured and calculated binding energy or  $g$ -factors, where here only the absolute value of the theoretical quantity was taken.

### 2.11.3 Fit to experimental data

The matrix was now diagonalized for different molecular coefficients  $C_x$  and the difference of theoretical quantities to the experimentally observed binding energies  $E$ , as well as their effective  $g$ -factor due to their rotational and spin-orbit coupling were calculated. The long range parameters were varied to find the minimum of the sum of weighted squared deviations. This fit was performed by Eberhard Tiemann. The fit routine was taken from CERN library, called "Minuit".

The comparison of the experimentally derived data, to the theoretical predictions of [62] (see table 2.1), shows clearly the necessity to take the  $C_8$  molecule coefficient into account. During the fit it turns out, that, based only on the binding energies, different combinations of molecular potential coefficients can be found. This explains the binding energies within kHz experimental uncertainty but leading to totally different  $g$ -factors. During the evaluation of the experimental data, fits were found in which within the series of observed levels a  $\Omega = 1$  level belonging to the asymptote  $^1S_0 + ^3P_2$  appeared. While the binding energies were still fitted well the  $g$ -factors imminently indicate a wrong solution. Only the inclusion of both, energies and Zeeman splittings, provides an accurate description of all observations with a potential model. These results have been published in [90].

**Comparison of the fit results to the experimental data:** The results of the fit to the experimental data is shown in table 2.7. The differences for the binding energies are on the order of the experimental uncertainty. The Zeemann effect is well described by the coupled channel model including the strong dependence on quan-

state		binding energy (GHz / $h$ )		$g$ -factor
$v'$	$\Omega$	method (4)	coupled channel model	coupled channel model
-4	0	44.75	44.758207	-0.0435
-4	1	57.91	57.852473	0.7946
-5	0		90.173668	-0.0243
-5	1		112.930480	0.7757

Table 2.8: Predictions of the binding energies for deeper bound vibrational states based on method (4) [62] and the presented coupled channel model as well as the theoretical prediction gyromagnetic ratio based on the coupled channel model.

tum number  $\Omega$ . We also derived from the coupled channel model the correct sign of the  $g$ -factor and thus the identification of the  $M = \pm 1$  levels.

**Comparison of the experimental data to the theoretical predictions:** The fit derived molecular potential coefficients allows predictions of the binding energies and the  $g$ -factors of the deeper bound vibrational states. Table 2.8 presents the predictions for the more deeply bound molecular states for the closed channel model compared the advanced Le Roy-Bernstein formalism, presented as method (4) in [62].

**Comparison of the fit results to *ab initio* calculations:** Based on *ab initio* calculations, there have been several predictions for the molecular potentials coefficients in  $\text{Ca}_2$ . In table 2.9 they were compared to the experimentally derived coefficients. The precise knowledge of the corresponding molecular potentials allows now to calculate theoretical predictions for optical Feshbach resonances, discussed in the following chapter. Therefore the Schrödinger equation was solved for the corresponding potentials (the here experimentally investigated excited potentials  $a$  and  $c$  as well as the ground state molecular potential  $X$ ) giving the wavefunctions of the bound excited vibrational states.

state	$C_6$			$C_8$	
	$(10^7 \text{ \AA}^6)$			$(10^9 \text{ \AA}^8)$	
	exp.	[63]	[70]	exp.	[70]
$c^3\Pi_u$	1.209	1.187	1.226	0.238	0.266
$a^3\Sigma_u$	1.335	1.313	1.358	0.905	1.057

Table 2.9: Derived long range parameters at the asymptote  $^1S_0 + ^3P_j$  and comparison with theoretical results from Mitroy and Zhang [70] and Ciurylo *et al.* [63]. Note: The for the quadratic Zeeman shift corrected binding energies result in slightly different molecular potential coefficients compared to [90].



## Chapter 3

# Modification of scattering length by optical Feshbach resonances theory and experimental test

In this chapter, I summarize the scattering length as a parameter for the description of scattering behavior and introduce optical Feshbach resonances (OFR) as a tool for controlled modification of the atomic scattering behavior. I present a theoretical model which describes the losses and the optically induced scattering length modifications. This model allows a comparison of different alkaline earth(-like) elements. Based on this theoretical model, the applicability and tuning range of optical Feshbach resonances in Ca is predicted, using the molecular potential model, developed in the previous chapter. These predictions were tested by a multi-photon PA experiment. These measurements showed for high PA intensities a line shape, which cannot be explained by the existing models.

### 3.1 Scattering length

The scattering length  $a$  describes low-energy scattering in quantum mechanics. It is defined by:

$$\lim_{k_r \rightarrow 0} k_r \cot \eta(k_r) = -\frac{1}{a}, \quad (3.1)$$

where  $\eta(k_r)$  is the  $s$ -wave phase shift. The elastic cross section  $\sigma$  at low energy is determined solely by the scattering length  $\lim_{k_r \rightarrow 0} \sigma = 4\pi a^2$ .

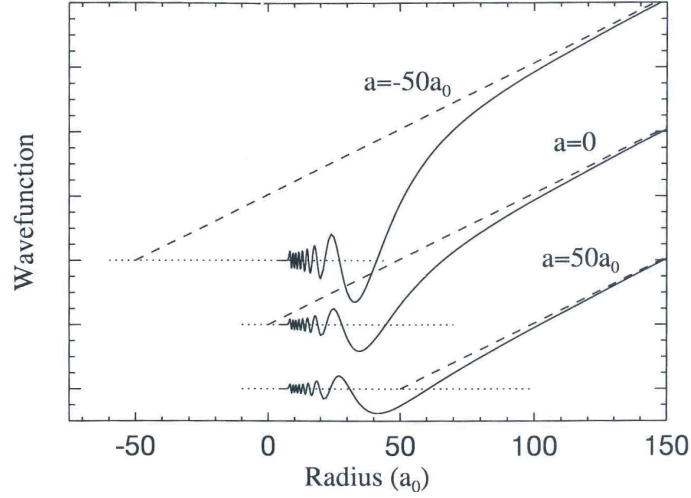


Figure 3.1: Scattering wavefunctions for three different values of scattering length  $a$  for  $k_r \mapsto 0$ . For clearness the wavefunctions have different offsets. The dashed lines indicate the matching of the wavefunctions for large  $R$  and  $k_r \mapsto 0$  with the unperturbed wavefunctions. Figure taken from [95] p. 205.

The physical interpretation of the scattering length  $a$  can be inferred from fig. 3.1, where the scattering wavefunction is shown for three different values of  $a$ . At very large internuclear separations, the wavefunction is a plane wave. Its wavelength is inversely proportional to the kinetic energy. At ultra-low temperatures, where only  $s$ -wave scattering occurs, the large wavelength justifies a Taylor expansion of the wavefunction that yields a linear fit to first order. The scattering length  $a$  is obtained by matching the wavefunction for large  $R$  and  $k_r \mapsto 0$  to the unperturbed wavefunctions, indicated by the dashed lines in fig. 3.1.

For short internuclear separations ( $R < 20 a_0$ ), there is no obvious difference between these three wavefunctions. At large internuclear separations  $R$ , they are shifted differently. Since the phase shift of the scattering wavefunctions at low temperatures is directly proportional to scattering length  $a$ , the whole potential and the scattering behavior can be described by only one parameter.

In a classical picture, a large scattering length  $a$  corresponds to repulsive hard shell scattering with particles of radius  $r_p = a$ . If  $a = 0$ , the wavefunction is indistinguishable from an unperturbed plane wave for large internuclear separation  $R$ . Thus a scattering of zero represents a non-interacting regime. There is no classical correspondence for negative scattering lengths. However,  $a < 0$  corresponds to a negative mean field energy.

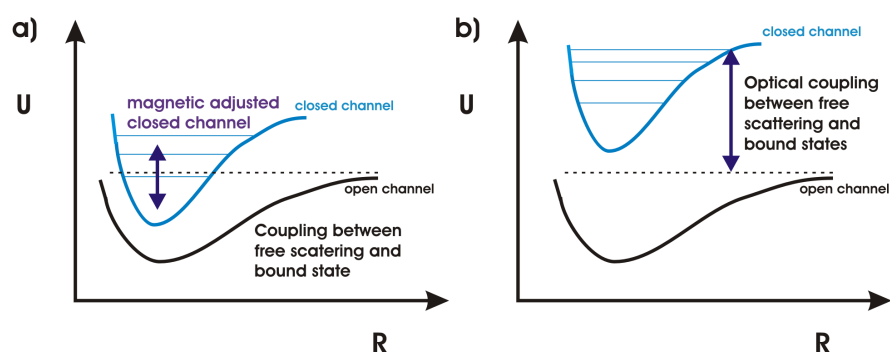


Figure 3.2: Potential energy  $U$  as a function of the internuclear separation  $R$  and the corresponding bound vibrational states. (a) Magnetic Feshbach resonance: Coupling between molecular potentials to the electronic ground state. (b) Optical Feshbach resonance: Optical coupling between electronic ground state and an excited electronic molecular state.

## 3.2 Optical Feshbach resonances

Modification of the scattering length by magnetically induced Feshbach resonances [96] is a key technique for investigations of ultra-cold atoms and for quantum-degenerate gases. A magnetic Feshbach resonance occurs, when a bound molecular state (closed channel) is tuned to couple near-resonantly to the scattering state (open channel) by a magnetic field. This resonant coupling changes the scattering length, which describes the scattering behavior completely at low energies.

A similar coupling can also be realized by a light field. Here, the scattering state is coupled by a resonant light field to a bound excited state. This phenomenon is called an optical Feshbach resonance [42, 46]. The principles of a magnetic and an optical Feshbach resonances are visualized in figure 3.2.

Compared to a magnetic Feshbach resonance, an optical Feshbach resonance provides several advantages: Light fields can be switched off, changed much faster than magnetic fields and allow switching from one side of the resonance - as function of the manipulated field - to the other, fast enough, to avoid adiabatic crossing of the resonance. Furthermore, frequency and amplitude of the light field can easily be changed separately. Therefore, and in contrast to magnetic Feshbach resonances, where only one parameter (field strength) can be changed, the field strength and redundant the frequency detuning of the light field can be chosen independently. These two independent parameters allow an optimization of the loss rates for a given manipulation of the scattering length. Optical Feshbach resonances are the only possibility of modifying the scattering length for atoms with a ground state, that lacks a magnetic sub-structure, such as  $^{40}\text{Ca}$ .

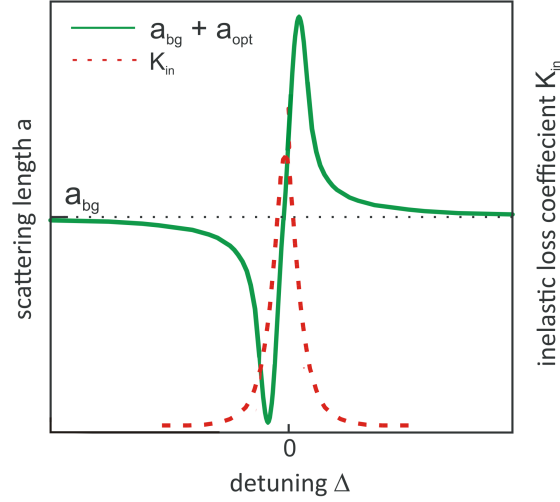


Figure 3.3: A qualitative picture of the theoretically expected (see later sections for a model) scattering length  $a = a_{bg} + a_{opt}$  as a function of the light frequency detuning  $\Delta$  from a bound excited state (green line) and the corresponding losses close to such a resonance (red dashed line).  $a_{bg}$  represents the scattering length in absence of light and  $a_{opt}$  the light-induced modification of  $a$ . The maximum in the scattering length modification  $a_{opt}$  is reached at a detuning  $\Delta = \Gamma_{mol}$ .

As pointed out in the previous chapter however, such a light field-induced coupling leads to atom losses. The largest scattering length modification is at a frequency detuning  $\Delta = \Gamma_{mol}$ , where the losses are large (see figure 3.3). In order to avoid huge losses for relatively small detuning, quantum systems with narrow transitions are of interest [97]. Therefore, in the last decade alkaline earth(-like) elements have become more important in the field of research on quantum-degenerate gases and ultra-cold atoms due to their narrow intercombination transitions between the singlet and triplet system.

The narrow linewidth of Ca, and alkaline earth metals in general, is expected to solve the loss problem [47] for the use of optical Feshbach resonances [98, 46]. So far optical Feshbach resonances in alkaline earth(-like) elements have been realized with Ytterbium [99] and Strontium [60]. In this chapter, I will present the theoretical predictions for scattering length modification in  $^{40}\text{Ca}$ , compare it to the mentioned above other elements, and present an experimental test of the predictions.

### 3.3 Theoretical model for the influence of light

The theoretical model presented here follows the calculations in [97] and describes the influence of light on the scattering length  $a$ . The light field couples the ground state to a single isolated bound excited state.

In this coupled channel model, scattering process is described by a scattering matrix, and  $S_{gg}$  represents the matrix element which gives the scattering amplitude between the incoming and the scattered wave, both of which are in the internal ground state. In order to describe the elastic collision, references [44, 100] introduce a complex scattering length  $\delta_s$  for the matrix element for  $k_r \rightarrow 0$ :  $S_{gg} = e^{i\delta_s k_r}$  with  $\delta_s = \lambda + i\mu$  and  $k_r$  the wavevector for the kinetic energy.

Following [100], the imaginary part of  $S_{gg}$  can be expressed as

$$\frac{\text{Im}(S_{gg})}{2k_r} = -\frac{\sin(2\eta_g)}{2k_r} \cdot \frac{\Delta^2 + (\Gamma_{mol}^2 - \Gamma_{stim}^2)/4}{\Delta^2 + (\Gamma_{mol} + \Gamma_{stim})^2/4} + \frac{\cos(2\eta_g)}{2k_r} \cdot \frac{\Gamma_{stim}\Delta}{\Delta^2 + (\Gamma_{mol} + \Gamma_{stim})^2/4}$$

It is related to the scattering length by

$$\lim_{k_r \rightarrow 0} \frac{\text{Im}(S_{gg})}{2k_r} = a = a_{bg} + a_{opt}. \quad (3.2)$$

And the real part corresponds to the inelastic losses as

$$K_{in} = \frac{1 - |S_{gg}|^2}{4k_r} = \frac{1}{4k_r} \cdot \frac{\Gamma_{mol} \cdot \Gamma_{stim}}{\Delta^2 + (\Gamma_{mol} + \Gamma_{stim})^2/4}, \quad (3.3)$$

where  $\Delta$  is the frequency detuning from the resonance,  $\Gamma_{mol}$  the natural molecular line width of the resonance,  $\eta_g$  is the elastic phase shift and  $\Gamma_{stim}$  the stimulated line width of the resonance.

The density of states, and thus the Franck–Condon density, is assumed to be constant over the stimulated width range and the electric dipole moment to be independent of  $R$  i.e.  $\langle \epsilon | \hat{D} | \psi_\epsilon \rangle = \hat{D} \cdot \langle \epsilon | \psi_\epsilon \rangle$ , where  $\hat{D}$  is the dipole operator.  $|\langle \epsilon | \psi_\epsilon \rangle|^2$  represents the coupling of the ground state  $\epsilon$  to the excited state  $\psi_\epsilon$ , where the Franck–Condon density and the molecular rotational coupling (of  $f_{ROT} = 1/3$  for this transition) are included. The stimulated line width is obtained by applying Fermi's golden rule<sup>1</sup>.

<sup>1</sup>Fermi's golden rule is a way to calculate transition rates from one energy eigenstate of a quantum system into a continuum of energy eigenstates due to a perturbation [2].

Here, it is used to describe to transition rate from a continuum to a bound state [97, 100, 101]:

$$\Gamma_{stim} = 2\pi \left\langle \epsilon \left| \hat{D} \right| \psi_\epsilon \right\rangle^2 = \Gamma_{atom} \frac{3}{4\pi} \frac{I\lambda^3}{c} f_{ROT} f_{FCD}, \quad (3.4)$$

where  $\lambda$  is the wavelength of the light field,  $c$  the speed of light,  $f_{ROT}$  the molecular Hönl–London factor and  $f_{FCD}$  the Franck–Condon density for the corresponding excitation.

For  $k_r \rightarrow 0$  the scattering length  $a$  and loss rate  $K_{in}$  given by eq. 3.3 and 3.3 become:

$$a(\Delta, I) = a_{bg} + \underbrace{\frac{\lambda^3 f_{ROT} f_{FCD} I}{16\pi c k_r} \frac{\Gamma_{mol} \Delta}{\Delta^2 + (\Gamma_{mol})^2/4}}_{a_{opt}} \quad (3.5)$$

and

$$K_{in} = \frac{2\pi\hbar}{\mu} \frac{\lambda^3 f_{ROT} f_{FCD} I}{16\pi c k_r} \frac{\Gamma_{mol}^2}{\Delta^2 + 1/4(\Gamma_{mol} + \Gamma_{stim})^2}, \quad (3.6)$$

where  $\mu$  is the reduced mass of the dimer.

For reasons of practicability, I define the optical length  $l_{opt}$  as

$$l_{opt} \equiv \frac{\lambda^3 f_{ROT} f_{FCD} I}{16\pi c k_r}. \quad (3.7)$$

Since the stimulated FWHM [47, 60] is proportional to the wavenumber  $k_r$ , the optical length  $l_{opt}$  is independent of the temperature (compare figure 3.4).

Using eq. 3.7, the equations 3.6, 3.4, and 3.5 can be expressed as

$$a_{opt} = \frac{l_{opt} \Gamma_{mol} \Delta}{\Delta^2 + \Gamma_{mol}^2/4} \quad (3.8)$$

$$K_{in} = \frac{2\pi\hbar}{\mu} \frac{l_{opt} \Gamma_{mol}^2}{\Delta^2 + 1/4(\Gamma_{mol} + \Gamma_{stim})^2} \quad (3.9)$$

$$\Gamma_{stim} = 2k_r l_{opt} \Gamma_{mol}. \quad (3.10)$$

This model allows predictions for the inelastic loss rate  $K_{in}$  and the optically induced scattering length  $a_{opt}$  based on the Franck–Condon densities derived from our model of the molecular potentials determined in the previous chapter.

### 3.4 Optical length as indicator for OFR capability

To observe an optically induced modification of the scattering length and not induce a significant amount of atom losses we have to operate in a regime where the detuning  $\Delta$  is much higher than the stimulated FWHM ( $\Delta \gg \Gamma_{stim} + \Gamma_{mol}$ ).

In this limit, equations 3.8 and 3.9 result in the following description of an optical modification of the scattering length  $a_{opt}$  as a function of optical length  $l_{opt}$  and detuning  $\Delta$ :

$$a_{opt} = \frac{l_{opt} \cdot \Gamma_{mol}}{\Delta}, \quad (3.11)$$

and for the loss rate

$$K_{in} = \frac{2\pi\hbar}{\mu} l_{opt} \cdot \left( \frac{\Gamma_{mol}}{\Delta} \right)^2 = \frac{2\pi\hbar}{\mu} \frac{a_{opt}^2}{l_{opt}}. \quad (3.12)$$

Evidentially, the parameters  $l_{opt}$  and  $\Delta$  can be controlled. For constant optically induced scattering length modification  $a_{opt}$ , the losses,  $K_{in}$ , decrease inverse proportional to  $l_{opt}$ ; hence the optical length is an appropriate quantity to describe the usability of optically induced Feshbach resonances.

### 3.5 Theoretical prediction for the optical length based on the molecular potential

Knowledge of the molecular potentials, determined in chapter 2, allows calculations of the wavefunctions of the bound molecular states. The molecular ground state potential is also well investigated [102]. Therefore, the scattering ground state wavefunction can be calculated as a function of the kinetic energy, and hence allows calculations of the Franck–Condon density as a function of the ground state energy. Figure 3.4 shows  $f_{FC} \cdot f_{ROT}$  of the PA excitations as function of the kinetic energy in the ground state<sup>2</sup>.

The background scattering length  $a_{bg}$  of has been determined by PA spectroscopy on the  $^1S_0 - ^1P_1$  transition [76] to be  $340a_0 < a_{bg} < 700 a_0$  and by BEC expansion [77] to be  $a_{bg} \approx 440 a_0$ . In this work, for the calculations we assume

<sup>2</sup> $f_{FC} \cdot f_{ROT} \propto l_{opt}/I$  (see eq. 3.7) is used since it is independent of the intensity. Thus, in the following we will use this value.

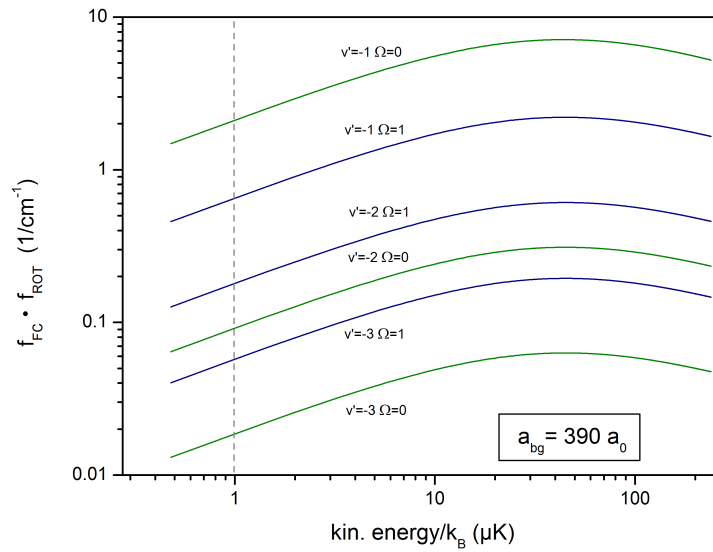


Figure 3.4: Calculated Franck–Condon densities - including the rotational factor - for the six observed PA resonances, as a function of the kinetic energy in the ground state based on the coupled channel model. For the calculation  $a_{bg} = 390 a_0$  was assumed. The dashed gray line represents the typical kinetic energy at  $T = 1 \mu\text{K}$  at which the PA measurements were performed.

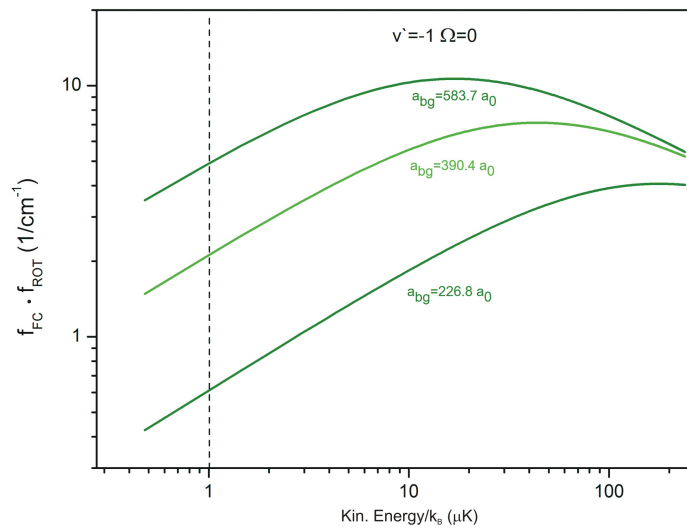


Figure 3.5: Theoretical predictions for  $f_{FCD} \cdot f_{ROT}$  of the  $v' = -1$  state in the  $c$  potential as function of the collisional energy for several ground state scattering lengths  $a_{bg}$ . The dashed line indicates the typical temperature  $T = 1 \mu\text{K}$  of the atomic ensemble for which the measurements were performed.

state		$l_{opt}/I$ ( $a_0/\text{W cm}^2$ )
$v'$	$\Omega$	
-1	0	130
-1	1	41
-2	0	11
-2	1	5
-3	0	4
-3	1	1

Table 3.1: Optical lengths for the three most weakly bound states in potential  $\Omega = 0$  and 1, normalized to the PA light intensity, given by equation 3.7, calculated for a background scattering length of  $a_{bg} = 390 a_0$ .

$a_{bg} = 390 a_0$ , which is in good agreement to both measurements and consistent to the calculation presented in [97].

Due to the uncertainty in the background scattering length determinations, the Franck–Condon densities and therefore the expected optical lengths are uncertain within a range of a factor of three. Figure 3.5 shows the calculated Franck–Condon densities as a function of the kinetic energy for several values of the background scattering length. Technically, the background scattering length was adjusted by two different methods: The first one is a variation of the slope of the repulsive short range branch of the potential. The second one is a variation of the potential energy in the molecular potential minimum. The linear shape in a bilogarithmic plot shows that, for temperatures below and around  $1 \mu\text{K}$ , the Wigner threshold law is expected to be valid up to a scattering length of more than  $a_{bg} > 700 a_0$ .

Table 3.1 shows the expected optical lengths as a function of the PA light intensity  $I$  for the most weakly bound states in the potentials  $\Omega = 0$  and 1.

Based on this model, we predict from eq. 3.7 and for a temperature of  $T = 1 \mu\text{K}$  and a maximum OFR laser intensity of  $I = 150 \text{ W/cm}^2$  an optical length of  $l_{opt} \approx 5800 a_0$  (for  $a_{bg} = 390 a_0$ ). This corresponds to a stimulated width of  $\Gamma_{stim} = 12 \text{ kHz}$ , which can be neglected compared to the Doppler width  $\Gamma_{Doppler} = 36.5 \text{ kHz}$  and a thermal broadening of  $\Gamma_{therm} \approx 15 \text{ kHz}$ . At a detuning of  $\Delta = 30 \text{ kHz}$ , where the predicted loss is  $N(t)/N_0 \approx 60\%$ , the expected scattering length modification is  $a_{opt} = 350 a_0$ .

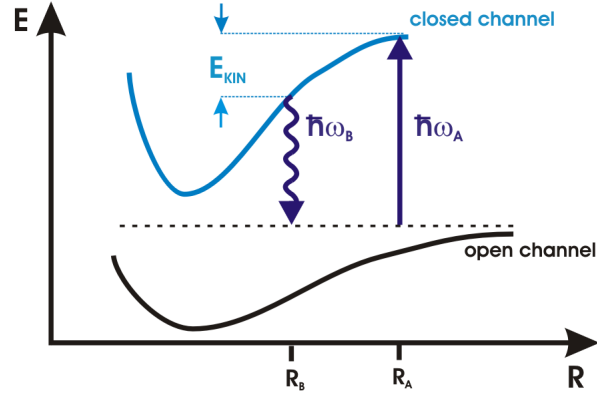


Figure 3.6: Schematic diagram showing radiative escape losses in the Gallagher–Pritchard model. Photon  $A$  with energy  $h\omega_A$  is red detuned to the atomic asymptote and transfers population to an excited potential for large internuclear separations. The excited atom gets accelerated radially until it emits photon  $B$  with energy  $h\omega_B$ . The kinetic energy  $E_{kin} = (h\omega_A - h\omega_B)/2$  transferred to each atom and may be sufficient to expel both from the trap.

### 3.6 Suitability of Ca for optical Feshbach resonances compared to other elements

Since the experimental access to magnesium and other alkaline earth(-like) elements is much more complex<sup>3</sup> and besides Sr and Yb no OFR experiments were performed so far, we will only discuss Sr, Yb and Ca in the following.

Compared to Sr and Yb, the natural atomic lifetime of calcium ( $\Gamma_{Ca} \approx 374$  Hz [61]) is more than 20 times smaller ( $\Gamma_{Sr} \approx 7.5$  kHz;  $\Gamma_{Yb} \approx 183$  kHz). Therefore,  $^{40}\text{Ca}$  has been supposed to be a good candidate for optical Feshbach resonances [47] without significant losses.

#### 3.6.1 Gallagher–Pritchard losses

Experiments with Ytterbium and Strontium [99, 60] observe additional density-dependent losses, which can be described as Gallagher–Pritchard (GP) losses [103] (see figure 3.6). The Gallagher–Pritchard model describes two different trap loss processes [91]. These are the so called fine structure-changing collisions (FCC) and radiative escape (RE) processes. The GP model considers a pair of atoms at a given internuclear separation  $R_0$  and illuminated by a laser  $A$  resonant to the corresponding energy  $E_A = \hbar\omega_A$  of photon  $A$  for the excitation at that separation. After this

<sup>3</sup>e.g. for Mg the technical access to the corresponding wavelengths is more difficult and the even narrower intercombination line requires a different loading scheme.

element	$\delta$ (MHz)	$\Gamma_{mol}$ (Hz)	$K_0$ ( $\text{m}^3/\text{s} / \text{W}/\text{cm}^2$ )	$K_{GP}$ ( $\text{m}^3/\text{s}$ )
$^{88}\text{Sr}$	-24	14 000	$1.0 \cdot 10^{-5}$	$3.4 \cdot 10^{-18}$
$^{172}\text{Yb}$	-800	366 000	$1.1 \cdot 10^{-5}$	$2.3 \cdot 10^{-18}$
$^{40}\text{Ca}$ <i>a</i> Pot	-983	740	$< 0.5 \cdot 10^{-5}$	$< 3 \cdot 10^{-24}$
$^{40}\text{Ca}$ <i>c</i> Pot	-308	740	$< 0.5 \cdot 10^{-5}$	$< 3 \cdot 10^{-23}$

Table 3.2: Gallagher–Pritchard losses  $K_{GP}$  calculated for  $I = 1 \text{ W}/\text{cm}^2$  for the most weakly bound states  $v' = -1$  in the  $^3P_1 + ^1S_0$  molecular potentials with binding energy  $E = h \cdot \delta$  and the spontaneous decay rate  $\Gamma_{mol}$  for  $^{172}\text{Yb}$ ,  $^{88}\text{Sr}$  as well as potential *a* and *c* of  $^{40}\text{Ca}$  given by equation 3.13 and an experimentally derived  $K_0(\text{Sr})$  [60], an estimated  $K_0(\text{Yb})$  (see text [99]) and the estimated upper limit for  $K_0(\text{Ca})$  (see text).

excitation, the atoms get accelerated towards each other in the attractive potential (in our case for the alkaline earth(-like) elements, mostly dominated by the van der Waals coefficient  $C_6$ ). In the RE process, the excited molecule emits a photon at internuclear separation  $R_1$  with energy  $E = \hbar\omega_B$ . The energy difference  $\Delta E = \hbar(\omega_A - \omega_B)/2$  is transferred as kinetic energy to each atom, leading to a trap loss. The FCC process describes a crossing to a different excited molecular potential with resonant energy at a given internuclear separation  $R_2$ , transferring energy  $E = \Delta_{FCC}/2$  to each atom, where  $\Delta_{FCC}$  is the energy difference of the atomic asymptotes. This leads to an atom loss for both involved excited molecular potentials. The loss rate  $K_{GP}$  was phenomenologically observed (and thus RE and FCC are considered) to be [60] for Strontium:

$$K_{GP} = K_0 \cdot \left(\frac{\Gamma_{mol}}{2\delta}\right)^2, \quad (3.13)$$

where  $\delta$  is the frequency detuning relative to the atomic asymptote and  $K_0$  and element specific constant experimentally determined to be  $K_0(\text{Sr}) = 5.8 \cdot 10^{-13} \text{ m}^3/\text{s}$  for an intensity of  $I = 0.057 \text{ W}/\text{cm}^2$ .

For  $^{172}\text{Yb}$ , this constant was estimated from the experimental data (shown in figure 2 in publication [99]). Since the atomic density is not given, we derive the loss rate  $K_{GP}$  by comparison of atom number loss rates  $\beta$  of the PA- and GP- induced losses. The ratio  $K/\beta$  was derived by comparing the value of  $K_{PA}$  given in the publication and  $\beta_{PA}$  derived from the graph. We estimate  $K(\text{Yb})_{GP} \approx 7.5 \cdot 10^{-19} \text{ m}^3/\text{s}$  for an intensity of  $I = 1.3 \text{ W}/\text{cm}^2$ . Using equation 3.13 for  $\delta \approx 800 \text{ MHz}$  [99] and  $\Gamma_{mol} \approx 366 \text{ kHz}$ , this leads to  $K_0 \approx 1.4 \cdot 10^{-5} \text{ m}^3/\text{s}$  for this intensity.

In order to compare the elements we assume a linear dependence  $K_0 \propto I$  and calculate the loss rate constant  $K_0$  for Yb and Sr for a given intensity of  $I = 1 \text{ W}/\text{cm}^2$ .

We find  $K_0(Sr) \approx 1.0 \cdot 10^{-5} \text{ m}^3/\text{s}$  and  $K_0(Yb) \approx 1.1 \cdot 10^{-5} \text{ cm}^3/\text{s}$ . In the Gallagher–Pritchard model this constant  $K_0$  depends on the long range form of the excited molecular potential.

For comparison, table 3.2 gives the corresponding GP loss rates  $K_{GP}$  for intensity  $I = 1 \text{ W/cm}^2$  for the most weakly bound states  $v' = -1$  in the  ${}^3P_1 + {}^1S_0$  molecular potentials for  ${}^{172}\text{Yb}$ ,  ${}^{88}\text{Sr}$  as well as potentials  $a$  and  $c$  of  ${}^{40}\text{Ca}$ . The corresponding GP losses for calcium are about 10 000 times smaller than in Ytterbium and Strontium due to its low  $\Gamma_{mol}$  and the relatively large detuning from the atomic asymptote  $\delta$ .

### Estimation of $K_0(Ca)$

We calculate an upper limit of  $K_0(Ca)$  from our experiment. During PA spectroscopy for the most weakly bound state  $v' = -1; \Omega = 0$ , at a detuning of  $\delta = 230 \text{ MHz}$  to the atomic  ${}^3P_1$  asymptote and for an irradiation time of 500 ms with intensity  $I \approx 80 \text{ W/cm}^2$ , no losses due to irradiation were observed. With respect to the signal to noise ratio, we assume, that an atom loss of  $> 5\%$  would have been identified. From equation 3.13 we get for an irradiation time of 500 ms and a 5% loss a maximum possible atomic loss coefficient  $\beta_{max} \approx 8 \cdot 10^{-7} / \text{s}$ . The ratio  $K/\beta$  was calculated (see next chapter) for the corresponding dipole trap geometry and depth. This gives a maximum loss rate of  $K_{GP,max} \approx 9.7 \cdot 10^{-22} \text{ m}^3/\text{s}$ . Assuming  $K_{GP} \propto I$  equation 3.13 leads to  $K_0(Ca)(I = 1 \text{ W/cm}^2) < 5 \cdot 10^{-6} \text{ m}^3/\text{s}$ .

This analysis indicates that high intensities can be used for the investigation of optical Feshbach resonances in Ca.

Density dependent losses caused by near resonant irradiation have already been observed in experiments with ultra-cold Ca [76]. They have been explained by possible photoassociation-induced losses assuming a bound state very close to the atomic asymptote. Since calculations based on the most weakly bound states  $v' = -1$  and the Le–Roy Bernstein formalism predict such a state close to the atomic resonance, in [62] another possible explanation was given by proposing an increased three body loss in the presence of irradiation close to the atomic asymptote due to OFR coupling to this state. The derived precise model of the corresponding molecular potentials (see chapter 2), however, predict no further bound states close to the atomic resonance besides the observed states. Thus the observed density-dependent loss cannot be explained as PA losses nor as additional three-body losses. We therefore try to explain these losses in the Gallagher–Pritchard model.

Element	$\delta$ (MHz)	$\Delta$ (kHz)	$K_{GP}$ (m <sup>3</sup> /s)	$K_{in}$ (m <sup>3</sup> /s)	$K_{total}$ (m <sup>3</sup> /s)
<sup>40</sup> Ca <sub><i>a</i></sub>	-983	45	$4 \cdot 10^{-22}$	$1.8 \cdot 10^{-18}$	$1.8 \cdot 10^{-18}$
<sup>88</sup> Sr	-24	68 000	$5 \cdot 10^{-16}$	$2.2 \cdot 10^{-19}$	$5 \cdot 10^{-16}$
<sup>172</sup> Yb	-800		$3.4 \cdot 10^{-16}$		$>3 \cdot 10^{-16}$

Table 3.3: Relative detuning  $\Delta$  to the most weakly bound states in the  $^3P_1 + ^1S_0$  potentials of <sup>40</sup>Ca (potential *a*), <sup>88</sup>Sr and <sup>172</sup>Yb<sup>5</sup> to achieve a scattering length change of  $a_{opt} = 100 a_0$  under similar experimental conditions ( $I = 150 \text{ W/cm}^2$  and  $T \approx 1 \mu\text{K}$ ) and loss rates for inelastic process and the GP losses  $K_{GP}$  at a detuning  $\delta$  relative to the atomic asymptote.

state $v'$	$\delta$ (MHz)	I (mW/cm <sup>2</sup> )	$l_{opt}$ ( $a_0$ )	$l_{opt}/I \cdot \delta^2$ ( $\frac{10^3 a_0 \text{cm}^2}{\text{mWMHz}^2}$ )
-2	-24	4	28	4
-3	-222	310	14	2
-4	-1084	524	14	31

Table 3.4: The ratio of the measured optical length and the light intensity  $l_{opt}/I$  for the  $v' = -2; -3; -4$  states in the  $0_u$  potential in <sup>88</sup>Sr and their corresponding PA detuning  $\delta$  relative to the atomic resonance [104].

### 3.6.2 Comparison of Ca to other elements

We now calculate the necessary detuning to a PA resonance,  $\Delta$ , to achieve a given optically induced scattering length  $a_{opt}$  for similar temperatures of the atomic cloud and similar irradiation intensities. We compare the sum of PA-induced and GP losses for the different elements. Table 3.3 summarize the parameters (the detuning from the PA resonance detuning  $\Delta$ , the corresponding inelastic loss rate  $K_{in}$  due to PA, the detuning relative to the atomic asymptote  $\delta$ , and the corresponding Gallagher–Pritchard losses  $K_{GP}$ , and the total loss rate  $K_{total} = K_{in} + K_{GP}$ ) for an intensity of  $I = 150 \text{ W/cm}^2$  at a temperature of  $T \approx 1 \mu\text{K}$ , to achieve an optically induced scattering length change of  $a_{opt} = 100 a_0$  for <sup>40</sup>Ca (potential *a*), <sup>88</sup>Strontium and <sup>172</sup>Ytterbium.

The expected loss rates  $K_{GP}$  for Calcium are about five orders of magnitude smaller compared to the elements Strontium and Ytterbium for a similar scattering length modification of  $a_{opt} = 100 a_0$ , for high PA intensity and a temperature of  $T = 1 \mu\text{K}$ . For losses at high intensities, Calcium is dominated by PA-induced losses, while for Strontium and Ytterbium the losses are dominated by GP losses. Also, the use of more deeply bound vibrational states to avoid background losses is not a solution in the case of Strontium since the optical length is decreasing for larger detuning from the atomic asymptote.

Table 3.4 shows the expected ratio of the measured optical length to the light

intensity  $l_{opt}/I$  for  $v' = -2, -3, -4$  states in the  $0_u$  potential and their corresponding PA detuning  $\delta$  to the atomic resonance for Sr, taken from [104]. The smaller background losses due to a higher detunings  $\delta$  are almost compensated by a smaller optical length per intensity. This is illustrated by the ratio  $l_{opt}/I \cdot \delta^2$ . This ratio can be understood as a coefficient for the ratio of the optical length and the loss rate  $l_{opt}/K_{in}$ , since the optical length as well as the background losses are proportional to the intensity (eq. 3.7). The ratio  $l_{opt}/K_{in}$  for the  $v' = -4$  state is expected to be one order of magnitude higher than in the  $v' = -2$  state, but still orders of magnitude worse compared to the  $v' = -1$  states in Ca. For more deeply bound states, an upper limit of the optical length is given by the decreasing FCDs and a maximum possible intensity for the spectroscopy laser due to technical reasons.

Thus, since  $l_{opt} \propto I$ , in Calcium much higher optical lengths can be realized. This analysis shows the benefit of the unique property of Calcium ( $\Gamma_{mol}/2\delta$  very small) for using optical Feshbach resonances. At  $\delta \approx -309$  MHz (close to the  $\Omega = 0; v' = -1$  resonance), no atomic loss rate was experimentally observed ( $K_{GP,theo}(I = 100 \text{ W/cm}^2) < 10^{-21} \text{ m}^3/\text{s}$ ) for intensities  $I > 100 \text{ W/cm}^2$  and irradiation times of  $t > 500$  ms. Since even for the most weakly bound PA resonance no further density dependent loss process is observed for high intensities and long irradiation times, Ca is expected to be a perfect candidate for observing optical Feshbach resonances for high light intensities and therefore small losses.

## 3.7 Test of scattering length modification

For testing the theoretically predicted strong influence of high-intensity PA laser light in Ca, we perform a two-photon detection scheme, similar to the one introduced by [99] and explained in the following.

### 3.7.1 Two-photon detection of the ground state scattering wavefunction phase

An optically induced modification of the scattering length results in a phase shift of the incoming ground state scattering wavefunction. This also changes the Franck-Condon densities of the ground state continuum and the excited, bound vibrational states for large internuclear separations. Due to this influence on the Franck-Condon density of this transition, the observable PA-induced loss rate is expected

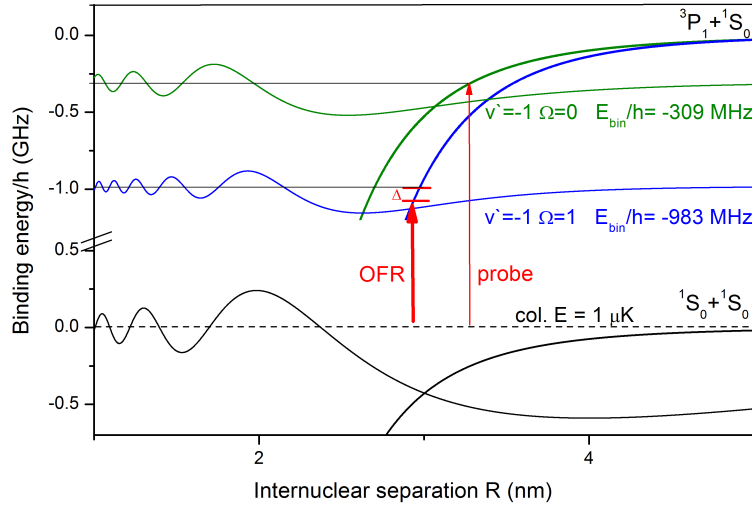


Figure 3.7: Wavefunctions of the most weakly bound vibrational states  $v' = -1$  in the potentials  $a(\Omega = 1)$  and  $c(\Omega = 0)$ , as well as the incoming scattering wavefunction in the ground state potential  $X$ , corresponding to the atomic asymptote  $^1S_0 + ^1S_0$  and the applied laser fields. The similarity of these wavefunctions is due to the similarity of the molecular potential shapes of the potentials  $a$ ,  $c$  and  $X$  because of the very weak  $C_3$  coefficient at the  $^3P_1 + ^1S_0$  asymptote and visualizes the limits of the reflexion approximation.

to change. Under the conventional reflexion approximation<sup>6</sup>, we assume that the excitations correspond to a well defined internuclear separation each. The idea is, to test this change of the PA loss rate by applying a probe PA laser, resonant to a vibrational state with a long classical turning point, while a second strong laser for OFR with different frequency detunings is coupling to a vibrational state with a shorter classical turning point. This scheme is shown schematically in figure 3.7.

Table 3.5 shows the classical turning points of the six observed resonances for the molecular potential coefficients, derived from our coupled channel model, as well as the calculated FCD for a collisional energy of  $T = 1 \mu\text{K}$ . These values support the feasibility of this scheme. The classical turning points for our potentials can be derived by equations 3.14 for potential  $a$  and 3.15 for potential  $c$

<sup>6</sup>If the molecular potentials differ for large internuclear separations, the overlap of both wavefunctions is mostly given by the contribution of the first peak at long range. For shorter nuclear distances, the wavefunction de-phases due to the different potentials at long ranges and thus due to destructive interference their contributions to the wavefunction overlap vanish. Therefore the excitation can be located at this relatively sharp internuclear range of the first peak [105].

state		binding energy (GHz · h)	classical turning points (nm)	$f_{FCD} \cdot f_{ROT}$ (1/cm <sup>-1</sup> )
$v'$	$\Omega$			
-1	0	0.309	3.1	2.2
-1	1	0.983	2.6	0.7
-2	0	4.649	2.1	0.2
-2	1	7.412	2.0	0.1
-3	0	17.857	1.7	<0.1
-3	1	24.539	1.6	<0.1

Table 3.5: Classical turning points and Franck–Condon densities for  $T = 1 \mu\text{K}$  for the six observed vibrational states in the potentials  $a$  and  $c$  estimated from the coupled channel model for  $a_{bg} = 390 a_0$ .

$$V_a = -\frac{4C_3^{(a)}}{R^3} - \frac{C_6^{(a)}}{R^6} - \frac{C_8^{(a)}}{R^8} + \frac{4 \cdot h}{8\pi^2 \mu R^2} \quad (3.14)$$

$$V_c = -\frac{2C_3^{(c)}}{R^3} - \frac{C_6^{(c)}}{R^6} - \frac{C_8^{(c)}}{R^8} + \frac{2 \cdot h}{8\pi^2 \mu R^2}, \quad (3.15)$$

where  $\mu$  is the reduced mass of the dimer and  $R$  the internuclear separation.

The coefficients  $C_6$  and  $C_8$  were taken from the coupled channel model given in table 2.9. The  $C_3$  coefficient is  $C_3^{(a)} = 3.22 \cdot 10^8 \text{ Hz nm}^3$  [106] for the  $a$  potential and  $C_3^{(c)} = 6.42 \cdot 10^8 \text{ Hz nm}^3$  [106, 58] for the  $c$  potential. The coefficients  $C_6$  and  $C_8$  presented in the previous chapter, given there for Hund's case (a), can be calculated [58] in Hund's case (c) by  $C_{n,0_u^+} = C_{n,3\Pi}$  and  $C_{n,1_u} = \frac{1}{2}(C_{n,3\Pi} + C_{n,3\Sigma})$ . The  $C_3$  coefficient can be calculated as  $C_{3,0_u} = -2 \cdot C_{3,1_u} = \frac{3\hbar c^3}{2\tau\omega^3}$ .

For our detection we chose the  $v' = -1$  states since these two states provide much stronger coupling to the ground state continuum and their classical outer turning points differ significantly. The strong coupling provides a long optical length in the applicable rang of the PA light intensity. The coupling of the  $v' = -1$  state in the  $c$  potential is stronger compared to the  $a$  potential (see fig. 3.4). We chose the state in the  $c$  potential to be our "probe"-resonance and the  $v' = -1$  state in the  $a$  potential as the "OFR" resonance, since a change in the phase of the ground state scattering wavefunction can only be observed for longer internuclear separations.

### 3.7.2 Theoretical predictions for loss rate changes by OFR

The Franck–Condon densities for the ground state continuum and the bound excited states depend crucially on the background scattering length of the ground state

molecular potential (see figure 3.5). Figure 3.8 shows  $f_{FCD} \cdot f_{ROT}$  of both bound vibrational states  $v' = -1$  as a function of the background scattering length. We can simulate the optically induced scattering length modification by a variation of the background scattering length in the coupled channel model. Assuming the reflexion wave approximation [64], the total amount of this modification can be observed at larger internuclear separations. Due to the very weak dipole moment of the intercombination line (leading to a weak  $C_3$  coefficient and thus to a pretty similar shape of the molecular potentials in the ground state and the excited state), this is a course assumption. Therefore, we expect this prediction to overestimate the effect.

The loss rate  $K_{in}$  depends linearly on the Franck–Condon density. Using the qualitative linear fit in the desired energy region of the Franck–Condon density as functions of the scattering length and assuming to model an optical modification of the scattering length by a variation of the background scattering length, this leads to an expected change of the loss rate for the "probe"-laser of 0.4% per  $a_0$  scattering length modification. Assuming further a linear dependence of the atom number on the atomic density, we can express the expected relative change of the atom number losses  $\Delta\beta$  as a function of the detuning of the "OFR"-laser relative to the bound state  $\Delta$  and OFR laser intensity  $I$  (see eq. 3.16). A modification of the scattering length on the order of several hundred Bohr radii is expected to lead to a change of the loss rate of the "probe"-laser of up to a factor of 3 – 5, which was expected to be resolvable since the experimental signal to noise ratio is more than 10.

### 3.7.3 Experimental realization

For the observation of optical Feshbach resonances, we use the same trapping and cooling system as was presented in the previous chapter. About  $N_0 = 10^5$  atoms were trapped and cooled to a temperature of  $T = 0.5 - 2 \mu\text{K}$ . The entire laser scheme is shown in figure 3.9. This detection scheme needs an additional spectroscopy laser system with the same requirement to their accuracy as in the PA measurements presented in the previous chapter. The laser system used so far for the PA measurements will be used as "OFR"-laser.

For the "probe"-laser a second diode-laser system was set up. This laser system mainly consists of a diode laser stabilized in frequency by an indirect beat lock to the ULE cavity. The beat lock is similar to that presented in the previous chapter. However, only one synthesizer is used for adjustments of the laser frequency. The

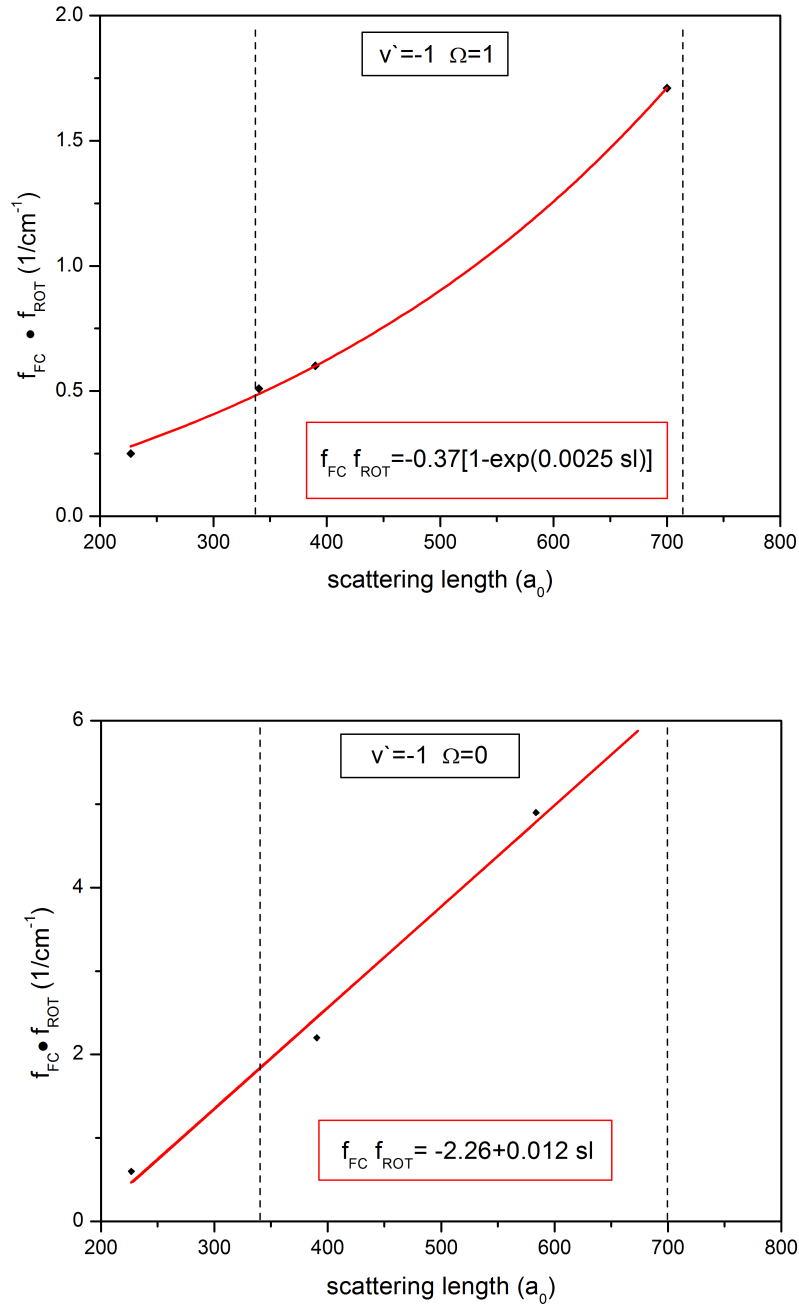


Figure 3.8:  $f_{FCD} \cdot f_{ROT}(\propto l_{opt})$  of the  $v' = -1$  states in both potentials as a function of the background scattering length from 200 to 700  $a_0$ . The dashed black lines give the range of the estimated background scattering length [75]. The red curves are approximations to the few calculated Franck–Condon densities (diamonds) for  $T = 1 \mu\text{K}$ . The red boxes give the assumed mathematical functions, where  $sl$  is the scattering length modification in  $a_0$ .

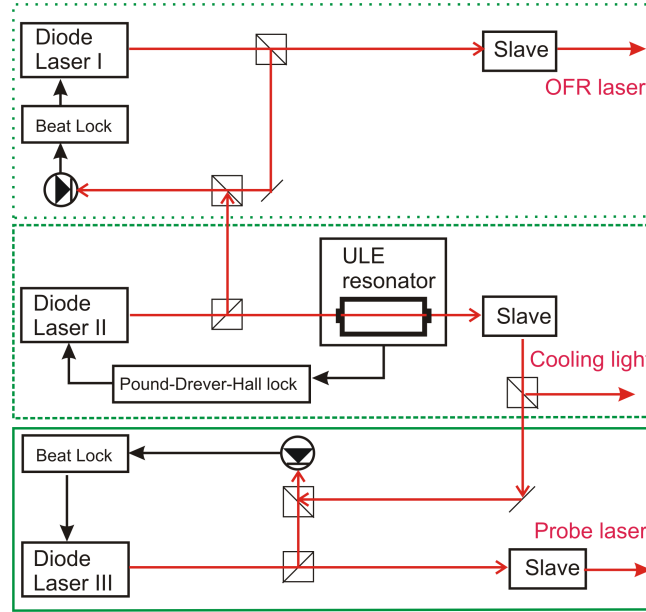


Figure 3.9: The additional laser used as "probe"-laser (green line) is a diode laser (Laser III) beat-locked to a slave of laser system II used for the second stage MOT (dashed line). Laser I (in chapter 2 used for PA spectroscopy (dotted line)) is used as "OFR"-laser.

frequency range of the beat lock is 1 GHz due to the photo diode. The diode laser seeds a second diode laser for amplification. Its light is sent by a fiber to the vacuum chamber in which the experiment takes place.

### 3.7.4 Measurement at high PA intensities

The measurement was performed by observing the loss spectra as a function of the detuning of the "OFR"-laser from the  $\nu' = -1; \Omega = 1$  resonance at high intensities in presence of the "probe"-laser, which is stabilized on resonance to the  $\nu' = -1; \Omega = 0$  PA transition. The irradiation time was chosen short enough to prevent saturation effects in the spectra of the "OFR"-laser by losing all atoms in the trap. The light intensity of the "probe"-laser for a given irradiation time was chosen to cause 30-60% loss. By a second measurement of the loss spectra by the OFR laser in absence of the probe laser the relative contribution of the "probe"-laser induced losses to the first spectra as a function of the detuning  $\Delta$  of the "OFR"-laser relative to the  $\nu' = -1; \Omega = 1$  state can be extracted and compared to the theoretical predictions given by equation 3.16 representing the formula for  $\Delta\beta(\Delta, I)$  derived in section 3.7.2.

$$\Delta\beta(\Delta, I) \approx 1 + 0.004 \cdot \frac{l_{opt}(I)\Gamma_{mol}\Delta}{\Delta^2 + 1/4(\Gamma_{mol})^2} \quad (3.16)$$

T ( $\mu\text{K}$ )	$\Gamma_{stim}$ (kHz)	$\Gamma_{Doppler}$ (kHz)	$\Gamma_{therm}$ (kHz)	$\Gamma_{theo}$ (kHz)	$\Gamma_{exp}$ (kHz)
0.6(1)	1.7	28	11	31	120
1.1(1)	1.7	38	20	43	170
2.1(2)	1.7	53	42	65	230

Table 3.6: The theoretically predicted stimulated width (eq.3.4) for an intensity of  $I = 30 \text{ W/cm}^2$  and the Doppler FWHM for the three investigated temperatures. For the asymmetric thermal broadening, we assume its contribution to be a Gaussian shape with a FWHM of  $\Gamma_{therm} = 20 \cdot \text{kHz}/\mu\text{K}$  (to be compared to calculations in chapter 2). Assuming the Lorentzian shape of  $\Gamma_{stim}$  to be negligible this leads to a total theoretically predicted FWHM of  $\Gamma_{theo}$  which is compared to the experimentally observed FWHM  $\Gamma_{exp}$ .

The intensity of the OFR laser  $I = 30(5) \text{ W/cm}^2$  was chosen to lead to a scattering length modification of up to  $100 a_0$  at a detuning of  $\Delta = 30 \text{ kHz}$  corresponding to predicted 20 – 50% PA induced losses depending on the temperature<sup>7</sup>. The expected change in the atom loss rate was  $\Delta\beta \approx \pm 30 \%$ . Thus a strong asymmetry in the shape of the loss spectra as function of the OFR laser was expected.

Figure 3.10 shows such measurements for different temperatures of the atomic ensemble. The intensity of the probe-laser was  $I = 5 \text{ W/cm}^2$ . The temperatures of the thermal gas cloud (estimated by TOF measurements) were varied from  $T = 2 \mu\text{K}$  to  $T = 0.5 \mu\text{K}$ .

For these temperatures no change of the loss rate contribution of the "probe"-laser was observable<sup>8</sup>. In addition the expected stimulated linewidth due to the high intensity given by equation 3.4 was expected to be  $\Gamma_{stim} \approx 1.7 \text{ kHz}$  for  $f_{FC} \cdot f_{ROT} = 0.7 \text{ 1/cm}^{-1}$ <sup>9</sup> and we expected from theory a lineshape strongly dominated by the Doppler- and thermal broadening. The measured and theoretical predicted FWHM are shown in table 3.6. Since the natural line-width is assumed to be  $\Gamma_{mol} \approx 750 \text{ Hz}$  it is not taken into account in this comparison.

Experimental investigations (see next chapter) gives an upper limit for the natural lifetime of  $\Gamma_{mol} < 10 \text{ kHz}$ . Calculations with the presented model and higher natural lifetimes within this limit does not provide a description of the observed line width. This light dependent broadening cannot be explained by equation 3.4 since the required Franck–Condon densities would correspond to background scattering

<sup>7</sup>For  $I = 30 \text{ W/cm}^2$  a stimulated rate of  $\Gamma_{stim} < 2 \text{ kHz}$  was predicted. Thus the width of the losses is expected to be dominated by the Doppler broadening (25–50 kHz, depending on the temperature).

<sup>8</sup>For a detailed analysis the measured loss rate  $\beta(\Delta)$  of the laser for the OFR was measured (black diamonds) and the contribution of the "probe"-laser  $\beta_{probe}$  to the total losses (red diamonds)  $\beta_{total} = \beta_{probe} + \beta_{OFR}$  was derived.

<sup>9</sup>For the calculation  $a_{bg} = 390 a_0$  and  $\Gamma_{mol} = 750 \text{ Hz}$  were assumed.

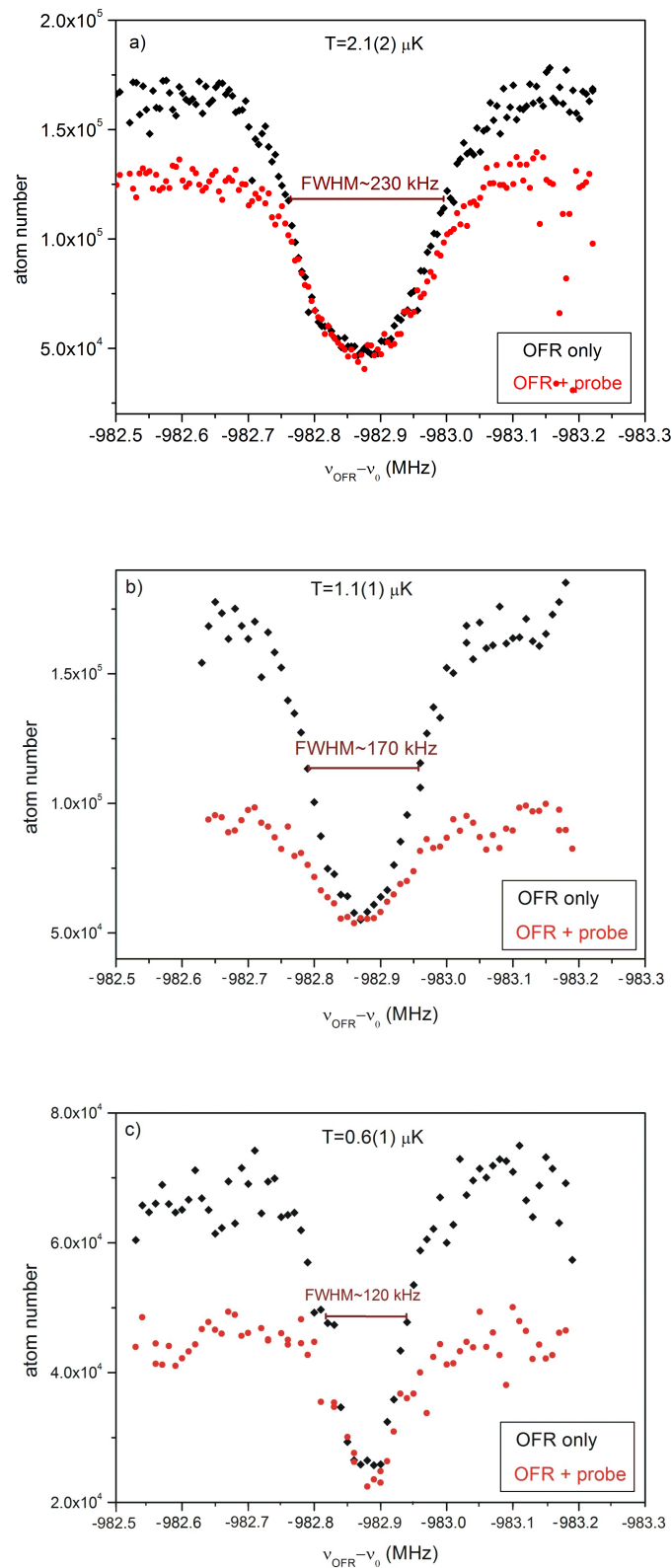


Figure 3.10: Atom loss spectra of the  $v' = -1; \Omega = 1$  state at temperatures of  $T = 2.1(2) \mu\text{K}$  (a),  $T = 1.1(1) \mu\text{K}$  (b) and  $T = 0.6(1) \mu\text{K}$  (c) with (red cycles) and without (black diamonds) "probe"-laser with intensity  $I = 5 \text{ W/cm}^2$  on resonance to the  $v' = -1; \Omega = 0$  state. The intensity of the "OFR"-laser was  $I = 30(5) \text{ W/cm}^2$  with an irradiation time of  $t = 50 \text{ ms}$ .

lengths of more than  $a_{bg} > 5000 a_0$  (eq. 3.7, fig. 3.5), which are in contradiction the investigation of PA on the  $^1S_0 + ^1P_1$  transition [75]. Furthermore such a stimulated width corresponds in the theoretical model (eq. 3.4) to an optical length of  $l_{opt} > 3 \cdot 10^5 a_0$ , leading to a very strong influence of the "probe"-laser even at far detuning  $\Delta \gg \Gamma_{stim}$  on the loss rate, which was not observed. This unexpected light-induced broadening (for investigations at very low intensities in chapter 2 widths on the order of 40 kHz due to Doppler- and thermal broadening were observed) prevents an observation of optically induced scattering length modification by this detection scheme. The discrepancy of the theoretical predicted FWHM and the experimental results will be investigated in the following chapter.

# Chapter 4

## High intensity photoassociation

As was pointed out in the previous chapter, the theoretical model of Bohn & Julienne [44, 100] does not provide a description of the observed width of the spectra for high PA intensities. In this chapter, first we will investigate the line shape behavior for high PA intensities and then discuss effects contributing to the width of the signal. Further we investigate the atomic loss rate, which is the experimental value, which has not been taken into account so far. This investigation of the observed loss rates allows to test our coupled channel model and the capability of the model of Bohn & Julienne for high PA intensities. This test indicates the need of an enhanced dressed state model for high PA intensities and a differentiation between the excitation rate and the stimulated width.

### 4.1 Experimental line shape investigation for high PA intensities

In this section I will present the experimental investigations on the dependence of the line width on PA intensities and the temperature of the atomic ensemble. Understanding of the line shape and the broadening processes is necessary for a quantitative analysis of the loss rates, which then will be compared to the predictions.

#### 4.1.1 Intensity- and temperature dependence of the signal width

For an investigation of the signal widths, we measure the width  $\Delta_{PA}$ , which is the FWHM of  $\beta(\Delta)$ , given from the fit of eq. 2.3 to the observed spectra. For Ca the spec-

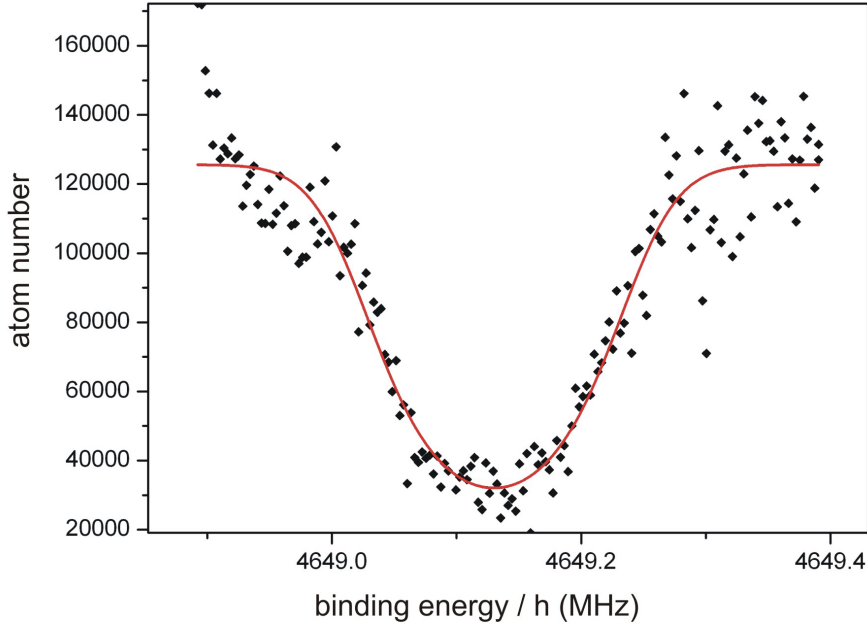


Figure 4.1: Loss spectra (black diamonds) of the  $v' = -2; \Omega = 0$  (potential  $a$ ) state and the fitted solution (red line) of  $\dot{N} = -\beta N^2$ . The PA intensity was  $I = 75 \text{ W/cm}^2$  at a temperature of  $T = 1 \mu\text{K}$ .

tra widths are not dominated by the natural line width. Depending on the temperature and the intensity we have a convolution of a Gaussian shape (mostly Doppler broadening) and a Lorentzian shape ( $\Gamma_{mol} + \Gamma_{stim/hom}$ ), leading to a Voigt profile. A Voigt profile however cannot be analytically described, but well approximated by a weighted sum of a Lorentzian and a Gaussian both having the same width. Appel [62] shows that an approximated Voigt is well suited to describe narrow PA loss spectra. Figure 4.1 shows the sufficiency of such a fit to a broadened high PA intensity spectrum. Thus, an apparent broadening effect due to a decreasing atom density during PA irradiation is taken into account.

The line widths  $\Delta_{PA}$  as a function of the PA light intensity for all six observed PA resonances are shown in figures 4.3 and 4.4. For higher intensities the linewidth saturates. From the model of Bohn & Julienne a linear intensity dependence  $\Delta_{PA} \propto I$  (eq. 3.4) is expected. Thus the saturation cannot be explained by the stimulated width  $\Gamma_{stim}$ . Also the observed width is several orders of magnitude higher than expected due to the Franck–Condon densities (eq. 3.4).

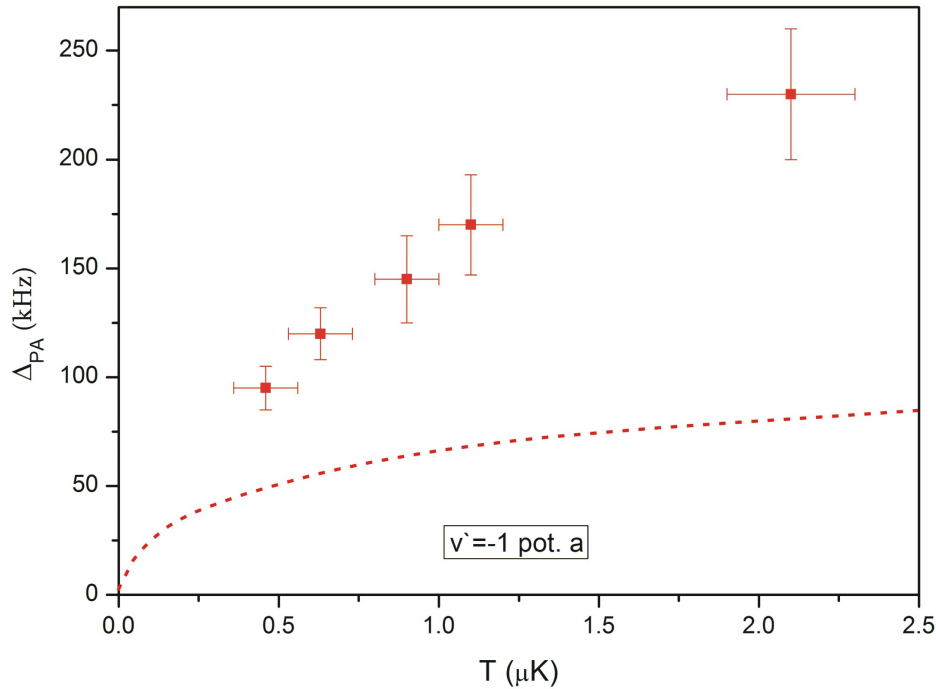


Figure 4.2: Observed FWHM  $\Delta_{PA}$  of the PA-transition to the  $v' = -1$  state in potential  $a$  as a function of the temperature of the atomic ensemble. The irradiation intensity was  $I = 30(5) \text{ W/cm}^2$ . The red dashed line shows the predictions given by the model of Bohn & Julienne [100].

Besides the dependence on the irradiation intensity, the line width for high PA intensities also show a crucial dependence on the temperature of the atomic cloud, which cannot be explained by the Doppler- and thermal broadening (see figure 4.2). The uncertainty of  $\Delta_{PA}$  is given by the fit-uncertainty to the loss spectra. The uncertainty of the corresponding temperatures was derived from TOF measurements. From the model of Bohn & Julienne a temperature dependence  $\Delta_{PA} \propto \sqrt{T}$  (eq. 3.10)<sup>1</sup> is expected.

<sup>1</sup>The stimulated width has a Lorentzian shape and a  $\sqrt{T}$  dependence. The Doppler broadening for this temperatures has about twice the amount of the thermal broadening, thus the thermal broadening has a relative small contribution to the total width. The Doppler broadening has a Gaussian shape with a  $\sqrt{T}$  dependence of the width. Thus, the resulting Voigt profile is expected to also have a  $\sqrt{T}$  dependence in this temperature regime.

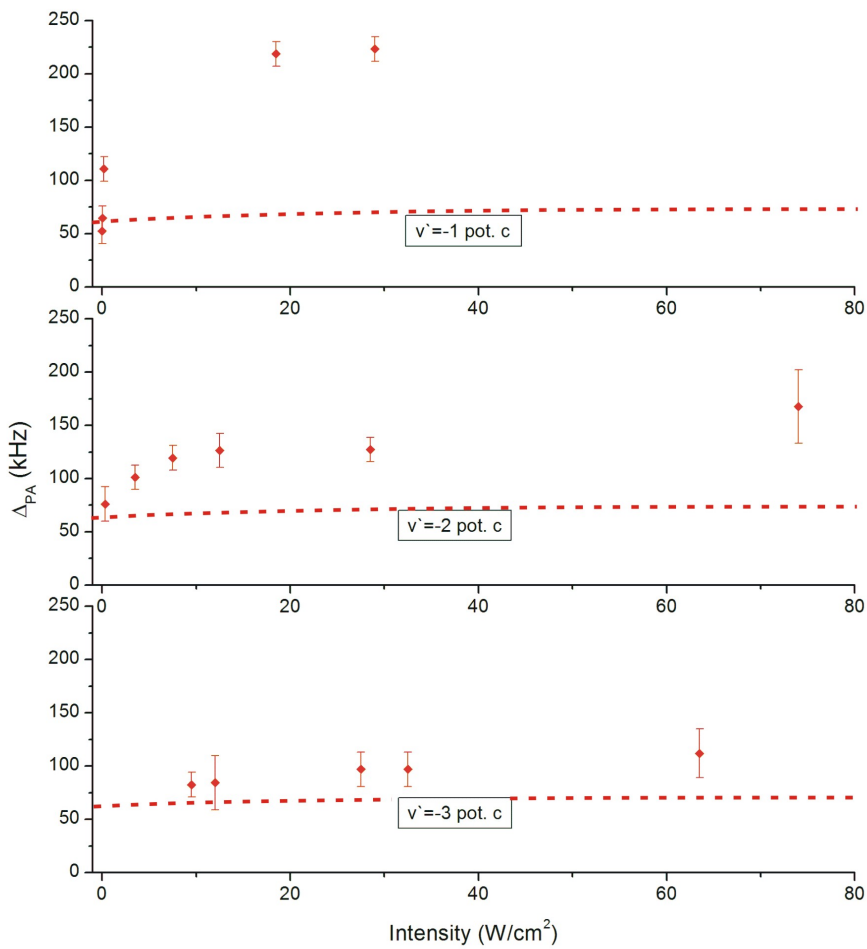


Figure 4.3: Experimentally observed FWHM  $\Delta_{PA}$  for the three most weakly bound states in potential  $c$  as function of the PA light intensity. The irradiation time was independently chosen in order to prevent a saturation of the loss signal. The temperature was  $T \approx 1 \mu\text{K}$ . The red dashed line shows the predictions given by the Bohn & Julienne model.

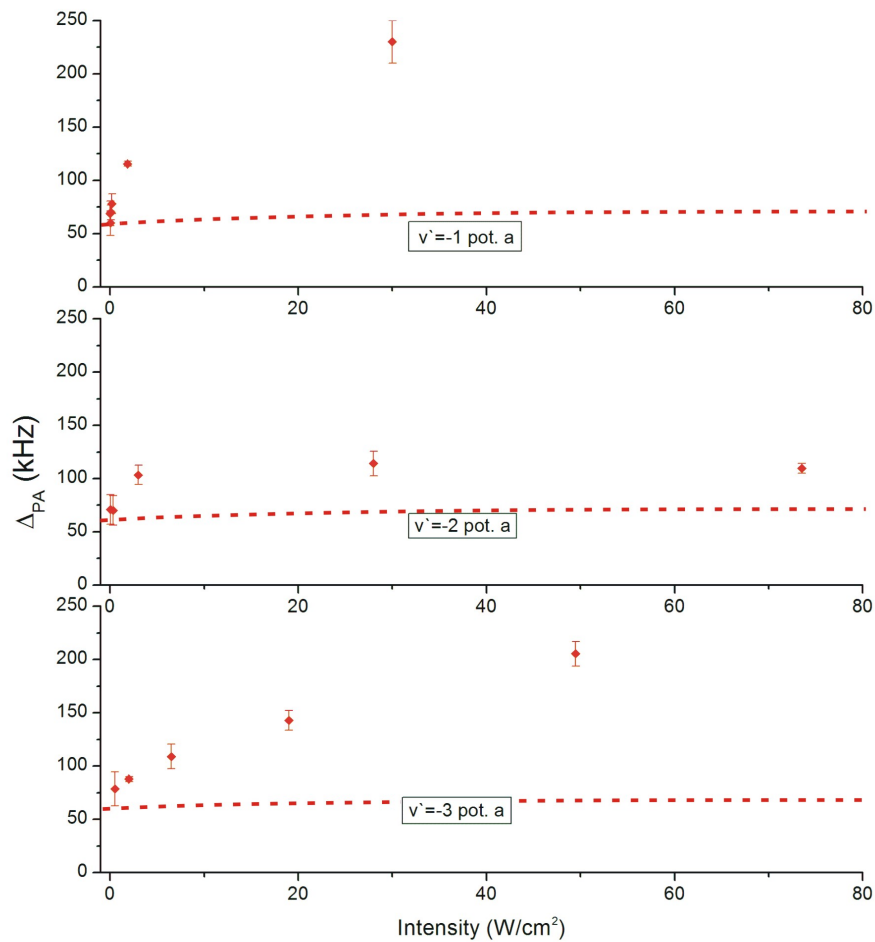


Figure 4.4: Experimentally observed FWHM  $\Delta_{PA}$  for the three most weakly bound states in potential  $a$  as function of the PA light intensity. The irradiation time was independently chosen in order to prevent a saturation of the loss signal. The temperature was  $T \approx 1 \mu K$ . The red dashed line shows the predictions given by the Bohn & Julienne model.

## 4.2 Line width discussion

Most PA studies performed so far with other elements were using spin-allowed transitions with MHz linewidth at  $\mu\text{K}$  temperatures. Also in recently realized PA measurements with alkaline earth(-like) elements Sr and Yb using a singlet-triplet transition the linewidth is much more dominated by their natural line width. Since the natural atomic line width of Ca is  $\Gamma_{atom} \approx 374 \text{ Hz}$  [61] here, other broadening mechanisms can be observed.

Several broadening effects contribute to the observed width  $\Delta_{PA}$  of a PA spectral line. Besides the affectness by the radiation intensity (power broadening) [107], these are spontaneous emission (natural line width), the center of mass motion (Doppler broadening), relative atomic motion (thermal broadening) and vapor density (pressure broadening) [108, 109] as well as coupling to other molecular states, not considered so far.

The different effects will be discussed in this section. The goal is to extract the PA light intensity dependent homogeneous broadening contribution  $\Gamma_{hom}(I)$ .

### 4.2.1 Doppler- and thermal broadening

These broadening effects, which were already discussed in chapter two, do not depend on the PA intensity. The combined FWHM corresponding to these effects at temperatures of  $T \approx 1 \mu\text{K}$  were calculated and measured to be  $\Gamma_T \approx 60 \text{ kHz}$ . Thus for high intensities ( $I > 10 \text{ W/cm}^2$ ) the width of the atom loss spectra is dominated by the presented intensity dependent effect with an unclear functional form (see fig. 4.4, 4.3) and the Doppler- and the thermal broadening cannot explain the observed spectra at high PA intensities.

### 4.2.2 Collisional broadening

At temperatures in the  $\mu\text{K}$  regime in the bosonic ensemble of  $^{40}\text{Ca}$  s-wave scattering is the dominant collision process. Therefore the scattering cross section for Ca+Ca collisions

$$\sigma_{s\text{-wave}} = \frac{8\pi a^2}{1 + a^2 k^2} \quad (4.1)$$

is given by the scattering length  $a$  and the wavevector  $\vec{k}$ . Assuming that the

scattering process  $\text{Ca}+\text{Ca}_2^2$  can be described with a scattering length  $a_{sc}$  similar to the scattering length of  $a_{sc} \approx 500 a_0$  for  $(a(\text{Ca} + \text{Ca}) = 340 - 700 a_0$  [76, 77]), a temperature of  $T \approx 1 \mu\text{K}$  and a peak density of  $n \approx 2 \cdot 10^{13} \text{ cm}^{-3}$  the collision time<sup>3</sup> is about of  $0.1 \text{ ms}$ <sup>4</sup>. The excited state can be de-excited by collisions between ground state and excited state atoms. This effects the lifetime of the excited state. The decay rate can be approximated by the inverse of the collision time scale and is even for an assumed high scattering length of several hundred  $a_0$  on the order of a few kHz.

A PA light intensity dependence for this collisional broadening could be due to a modification of the scattering length as a function of the light frequency due to OFR. The expected induced modification of the scattering length of  $\text{Ca} + \text{Ca}$  at a frequency detuning of 100 kHz at a PA intensity of  $I \approx 100 \text{ W/cm}^2$  is on the order of  $a_{opt} \approx \pm 10 a_0$  (see chapter 3). Assuming a similar change for  $\text{Ca} + \text{Ca}_2$  and as no asymmetry for high PA intensities was observed (see chapter 3), this collision broadening effect can be excluded.

### 4.2.3 Line width broadening due to coupling to other molecular states

In a molecule the modification of the wavefunction can change the width compared to the corresponding atomic transition.

For long range internuclear separation molecules, such as photoassociation excited molecules near the atomic asymptote, the dipole matrix element for the excitation was calculated from the atomic transition dipole element.

A dimer can form a super-radiant state<sup>5</sup> leading to half the amount of lifetime, corresponding to twice the natural line-width compared to the atomic state.

This however is only valid for the unperturbed bound molecular states. The lifetime of the excited molecular state can also be decreased by a perturbation from other bound molecular states, corresponding to different atomic asymptotes. Allard et al. [71] observed by fluorescence spectroscopy the coupling of the states  $a^3\Pi_1$  and

<sup>2</sup> $\text{Ca}_2$  is a dimer of a Ca atom in the ground state and a Ca atom in the excited state.

<sup>3</sup>The mean free path of the scattering particles is  $MFS = 1/(n \cdot \sigma)$ . Divided by the velocity corresponding to the kinetic energy this gives the average collision time scale.

<sup>4</sup>This describes the time scale for a ground state-ground state collision, which is expected to destroy the coherence for the excitation process. The time scale to the excited state as destruction of the population, is expected to be slower.

<sup>5</sup>In a superradiant state the decrease of the natural life time can qualitatively be understood as decay stimulated by a spontaneous emitted photon of the other dimer atom[110].

$A^1\Sigma_u^+$ , which would lead to a shortening the lifetime because of singlet admixture. A coupling to bound states of other molecular potentials is not expected since these are energetically farther away. They observed a bound vibrational state  $v_A = 11$  in the molecular potential  $A^1\Sigma_u^+$  with an energy relative to the ground state  $^1S_0 + ^1S_0$  molecule potential of  $E = 15534.4822 \text{ cm}^{-1}$ .

The anharmonicity of the molecular potential leads to a decreasing level spacing for higher energies. This results in a higher possibility to have a bound state in potential  $A$  close to the observed resonances. For a first approximation, I extrapolate for an harmonic potential - and therefore for an equidistant level spacing - the deeply bound  $A^1\Sigma_u^+$  states. A linear extrapolation based on these data would lead to the  $v_A = 18$  state in the  $A^1\Sigma_u^+$  potential with an energy relative to the ground state minimum of  $E \approx 16334.9072 \text{ cm}^{-1}$  (and thus 700 GHz off resonance), as energetically closest bound state relative to the experimentally observed PA resonances.

The assumption of an harmonic potential for this energy range however is not valid. Due to the experimentally observed spectra at temperatures of down to 400 nK at low PA intensity, we determined an upper limit for the natural line-width of  $\Gamma_{mol} \leq 10 \text{ kHz}$ .

#### 4.2.4 Light shift broadening by light field distribution

Two different phenomena, based on the light shift, are leading to a broadening. As laid out in chapter 2 both, the dipole trap laser beams and the PA inducing laser are shifting the PA resonance frequency. Since the dipole trap laser beams are focused, and the intensity of the PA spectroscopy laser is given by its beam profile, the experienced intensities depends on the position of the atoms in the dipole trap, given by the Boltzmann distribution, with an average kinetic energy of  $\frac{3}{2}k_B T$ .

The light shift due to the dipole trap for the full trap depth  $U_{max} \approx 10 \text{ } \mu\text{K}$  was measured to be on the order of 100 kHz. Due to a ratio of the average kinetic energy and the trap depth of  $\approx 1/10$  we expect the broadening effect due to a variation of the light shift to be on the order of  $\approx 10 \text{ kHz}$ .

The light shift broadening due to the PA laser can be approximated by comparing the intensity distribution to the three dimensional Boltzmann distribution of the atoms in the approximate harmonic potential of the dipole trap. The  $1/\sqrt{e}$  width  $w$  of the PA laser beam at the position of the atoms was measured<sup>6</sup> to be  $w = 50(6) \text{ } \mu\text{m}$ ,

<sup>6</sup>The determination of the width was realized by a beam profile camera.

which is about one order of magnitude larger than the width of the thermal distribution in the dipole trap. The PA spectroscopy laser light shift was up to 30 kHz for high intensity (see fig. 2.15) and the broadening due to the PA laser is on the order of a few kHz.

In total the broadening effects due to the homogeneous light shift effect can be excluded.

## 4.2.5 Energy dependent light shift

The PA light shift also depends on the energy  $\epsilon$  and thus might occur as broadening. For this type of broadening we have to consider the dependence of the light field coupling and the light shift by the kinetic energy, i.e. by the temperature. To describe the system theoretically for each channel, a pair<sup>7</sup> of energy-normalized reference functions  $f_i(R)$  and  $g_i(R)$  are given [100, 97], which satisfy the single-channel Schrödinger equation for the collisional  $\epsilon$

$$\left( -\frac{\hbar^2}{2\mu} \frac{d^2}{dR^2} + V_i(R) \right) \times \begin{Bmatrix} f_i(R) \\ g_i(R) \end{Bmatrix} = \epsilon \times \begin{Bmatrix} f_i(R) \\ g_i(R) \end{Bmatrix}. \quad (4.2)$$

Since  $f_i$  fulfills the boundary conditions for the atom pair scattering process [100, 111] it is defined as the "regular" solution, leading the FCD into the expressions 3.4, while  $g_i$  is defined to be "out of phase" with this boundary condition and thus named "irregular" solution<sup>8</sup>.

For s-wave scattering in the ground state,  $f_g(R)$  and  $g_g(R)$  for large  $R$  are in the form of [97]:

$$f_g(R) \xrightarrow{R \rightarrow \infty} \sqrt{\frac{2\mu}{\pi \hbar^2 k_r}} \sin(k_r R + \eta_g) \quad (4.3)$$

$$g_g(R) \xrightarrow{R \rightarrow \infty} -\sqrt{\frac{2\mu}{\pi \hbar^2 k_r}} \cos(k_r R + \eta_g). \quad (4.4)$$

It was shown [100], that the "regular" solution leads to the already introduced stimulated width  $\Gamma_{stim}$  (eq. 3.4), where  $f_{FCD} = \left| \int_0^\infty dR \psi_\epsilon(R) f_g(R) \right|^2$  is the overlap of the regular solution of eq. 4.2 with  $\psi_\epsilon(R)$ , as the wavefunction of the bound excited state (see chapter 3).

<sup>7</sup>In chapter 3 only the "regular" function which is of relevance for the scattering length modification was mentioned.

<sup>8</sup> $g_g$  does not fulfill the physical boundary condition  $g_g = 0$  at  $R = 0$ .

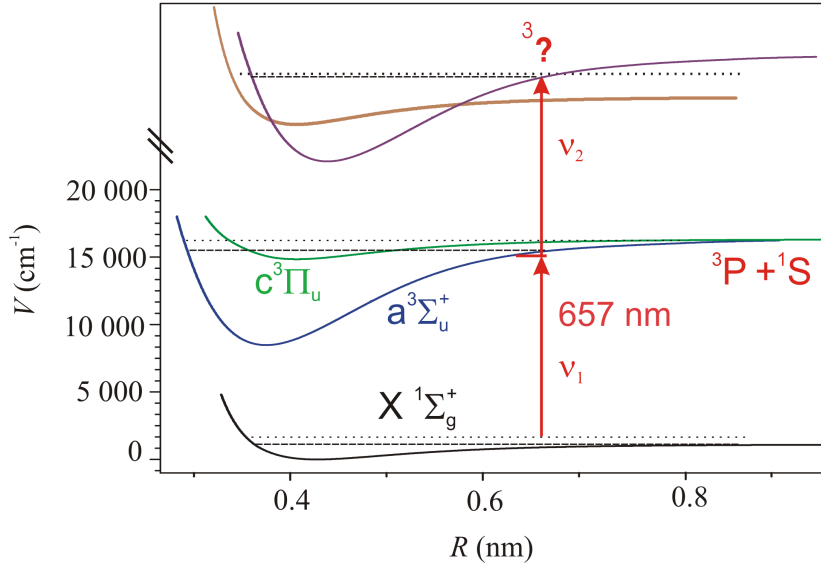


Figure 4.5: Schematic picture of a two photon excitation to higher energy bound states, leading to much higher stimulated loss rates than predicted by the model of Bohn & Julienne [44, 100], which only takes one bound state into account. In the triplet system these transitions have much stronger dipole matrix elements via a bound state in potential  $a$  or  $c$ .

The irregular solution leads to an energy shift  $\Delta E_{ge}(\epsilon, I)$  [100] in the form of [97]:

$$\Delta E_{ge}(\epsilon, I) = \Gamma_{atom} \frac{3}{4\pi} \frac{I\lambda^3}{c} f_{ROT} f_{FCD}^{\Delta E}(\epsilon), \quad (4.5)$$

with

$$f_{FCD}^{\Delta E}(\epsilon) = \int_0^\infty dR \psi_e(R) g_g(R) \int_0^R dR' \psi_e(R') f_g(R'). \quad (4.6)$$

This energy shift  $\Delta E$  depends on the intensity of the PA inducing light and the kinetic energy  $\epsilon$  and thus on the temperature  $T$ . Since the energy shift can change as a function of the temperature  $T$ , this effect can lead to a broadening of the signal width. The averaged light shift for temperatures of  $T \approx 1 \mu\text{K}$  due to the PA laser light was measured to be on the order of several tens of kHz (see fig. 2.15). Also theoretical investigations of the irregular solution for Ca in contrast to Sr only predict positive energy shifts [97]. Thus this mechanism is not expected to explain the experimentally observed broadening.

### 4.2.6 Multi-channel coupling

In the model of Bohn & Julienne [44, 100] for the stimulated width  $\Gamma_{stim}$ , only the coupling to one bound state was taken into account. The stimulated loss rate can be much higher, if the excited state couples - by a second photon - to bound states or excited state continuums of molecular potentials in the triplet system at energies of about  $E \approx 30\,000\text{ cm}^{-1}$  relative to the ground state (see fig. 4.5). The dipole matrix elements to these triplet states are several orders of magnitude larger compared to the dipole matrix element of the intercombination line. The optical length however, mostly depends on the coupling strength between the ground state and the excited bound state<sup>9</sup>. Thus the losses due to coupling to other triplet states might explain the discrepancy of the observed stimulated width and the expected modification of the scattering length for such a corresponding stimulated width.

However such a coupling to other states is not expected to have a temperature dependence. Thus this mechanism is not capable to describe the observed spectra.

#### Homogeneous PA contribution $\Gamma_{hom}$

Since the investigated broadening effects do not provide a description of the observed widths, we will now extract the homogeneous PA light dependent contribution  $\Gamma_{hom}$  to the observed spectra. For  $T \approx 1\text{ }\mu\text{K}$  the combination of the thermal and Doppler broadening leads to a line shape, which can fairly be well described by a Gaussian shape with a FWHM of  $\approx 60\text{ kHz}$ , while the sum of  $\Gamma_{mol}$  and  $\Gamma_{hom}$  leads to a Lorentzian contribution. Thus the line is assumed to have a Voigt profile consisting of a Gaussian contribution for the Doppler broadening and the thermal broadening of FWHM  $\approx 60\text{ kHz}$  and a Lorentzian contribution with a width dependence of the PA light intensity. Following the calculations of [112], the Voigt width  $\alpha_V$  can be approximated by the Gaussian width  $\alpha_G$  and the Lorentzian width  $\alpha_L$ :

$$\alpha_V(\alpha_L, \alpha_G) = (\alpha_L + \alpha_G) \cdot \left[ 1 - \alpha \left( 1 - \left( \frac{\alpha_L - \alpha_G}{\alpha_L + \alpha_G} \right)^2 - \zeta \cdot \sin\left(\pi \cdot \frac{\alpha_L - \alpha_G}{\alpha_L + \alpha_G}\right) \right) \right], \quad (4.7)$$

with  $\alpha = 0.18121$ ,  $\zeta = 0.023665 \exp\left(0.6 \cdot \frac{\alpha_L - \alpha_G}{\alpha_L + \alpha_G}\right) + 0.000418 \exp\left(-1.9 \cdot \frac{\alpha_L - \alpha_G}{\alpha_L + \alpha_G}\right)$ .

From the observed width we extract the Lorentzian contribution  $\alpha_L$  for  $\alpha_G = 60\text{ kHz}$ .

<sup>9</sup> $l_{opt}$  (eq. 3.7) was defined for a single photon process. Nevertheless the modification of the scattering behavior is expected to depend mostly on the coupling of the first stage of the excitation.

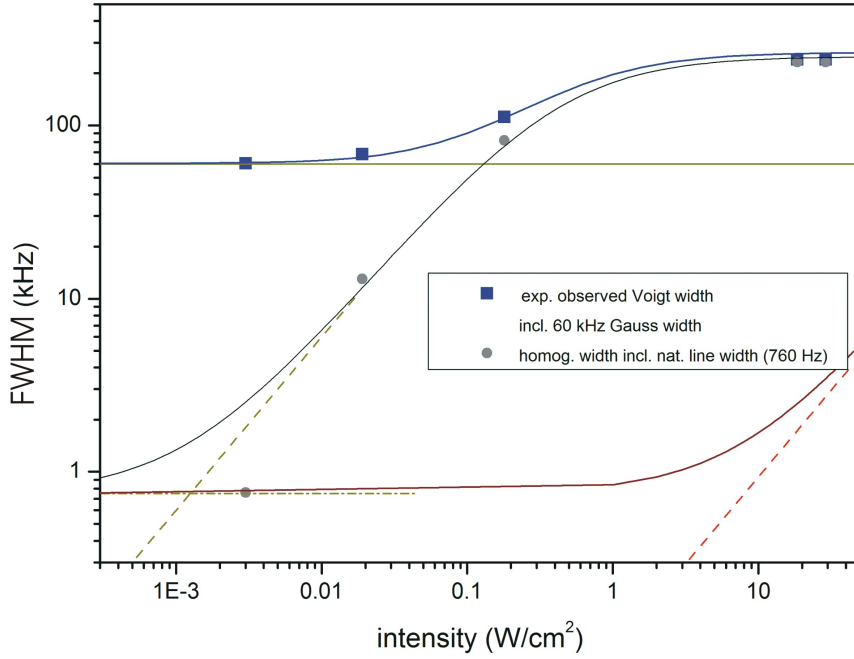


Figure 4.6: The blue squares are the experimentally derived FWHM with a phenomenological fit (blue line) [ $\text{FWHM} = 1 / ((1/600000 \cdot \text{W}/\text{cm}^2 + 748) + 4 \cdot 10^{-6}) \text{Hz}$ ]. The green line indicates the Gaussian  $\alpha_D = 60$  kHz. Assuming the blue curve to be a Voigt distribution  $\alpha_V$ , eq. 4.7 gives the Lorentzian contribution  $\alpha_L$ , which is visualized by the black curve. The red dashed line indicated the expected FWHM given by eq. 3.4 ( $a_{bg} = 390 a_0$ ). The solid red line is the sum of the predicted stimulated and the natural line width. The green dashed line is a linear fit to the black curve in the intermediate range of the intensity, where a linear dependence of the width and the intensity was experimentally observed.

In figure 4.6 we present the experimentally observed FWHM of the  $v' = -1; \Omega = 0$  resonance as function of the light intensity (blue curve), their determined Gaussian contribution (green curve) and the PA light dependent Lorentzian (black curve) contribution  $\Gamma_{hom}$  including the natural line width.

The observed  $\Gamma_{hom}$  as function of the intensity, besides the observed saturation effect for very high intensities, might be explained by much higher Franck–Condon densities, compared to the predicted densities by our coupled channel model.

Thus in the next sections we will investigate the experimentally observed loss rates and compare them to the theoretical predictions. If the experimentally observed loss rates can be explained by Franck–Condon densities - corresponding to the observed stimulated widths - this would be an indicator that the FCD predicted by our coupled channel model are wrong.

### 4.3 Experimentally observed PA-loss rate

In this section we will investigate the observed PA atom losses. The goal is, to derive from the experimental data loss rates, which are comparable to the predictions of the model of Bohn & Julienne [100], for different intensities.

The time evolution of the number of atoms  $\dot{N}$  in the center region of the trap can be expressed by

$$\dot{N} = -\alpha N - \beta N^2 - \gamma N^3 + \dot{N}_{td}(t), \quad (4.8)$$

where  $\alpha, \beta, \gamma$  are the atomic loss coefficients corresponding to background scattering, two-body and three-body loss processes and  $\dot{N}_{td}(t)$  is an additional loading term, corresponding to internal trap dynamics.

In order to analyze the photoassociation induced atom losses quantitatively we have to distinguish and discuss more detailed the relevant atom loss mechanisms corresponding to the coefficients  $\alpha, \beta$  and  $\gamma$ , which will be presented in the following.

#### 4.3.1 Three body loss processes

Due to the conservation of momentum and energy, the collision of two trapped atoms cannot lead to a loss of atoms in the absence of light. But it is possible if there are three atoms participating in the collision. This process is called three-body recombination.

In this process three atoms collide and two of them form a dimer whereas the binding energy of the created ground state molecule  $E_g$  is set free as kinetic energy. Due to momentum conservation,  $E_g/3$  is transferred to the created dimer and  $2E_g/3$  to the third collisional partner. Since the binding energy  $E_g$  is large compared to the trap depth during PA, the created molecule and the third colliding atom escape from the trap, leading to a loss of atoms. The event rate of this process is proportional to the third power of the atomic density  $n$ :

$$\dot{n} = -L_3 \cdot n^3, \quad (4.9)$$

where  $L_3$  is the three-body loss rate coefficient which scales with fourth power of the scattering length of the two-body process [98, 113]. A large scattering length

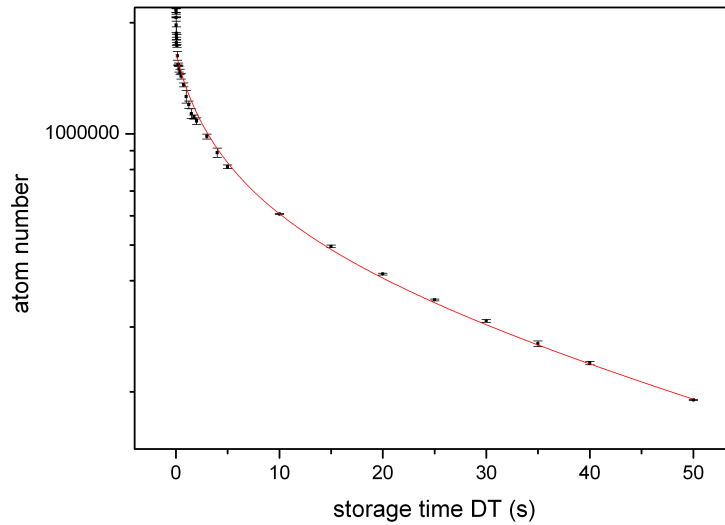


Figure 4.7: Number of atoms in the crossed dipole trap as function of the storage time. The estimated lifetime due to background gas scattering was  $\tau \approx 56$  s. The red curve shows the fitted equation 4.10.

leads to large three-body losses. Thus for Ca, where the scattering length was measured to be several hundred Bohr radii [76, 77] significant three-body losses might occur. The coefficient  $L_3$  corresponds to the loss coefficient  $\gamma$ .

For Ca this three-body loss coefficient was determined to be  $L_3 = (3.2 \pm 1.6) \cdot 10^{-27} \text{ cm}^6/\text{s}$  [76] and  $L_3 = (5.5 \pm 2.6) \cdot 10^{-27} \text{ cm}^6/\text{s}$  [77]. The peak density of the atomic ensemble during PA measurements was determined to be  $n_0 \approx 1.1 \cdot 10^{13} \text{ cm}^{-3}$ . During the investigations of the three-body losses in a deep dipole trap, these losses were only observed with a peak density around  $n_0 = 1.4 \cdot 10^{14} \text{ cm}^{-3}$ . The contribution will be discussed in the next section, also taking the linear losses (corresponding to the loss coefficient  $\alpha$ ) and trap dynamics into account.

### 4.3.2 Background gas scattering processes

The probability of an elastic scattering process of the trapped atoms with a remaining hot background gas particle is expected to be linearly proportional to the pressure  $p$  in the vacuum chamber. Thus this pressure was improved to  $p \approx 2 \cdot 10^{-10} \text{ mbar}$  in order to reduce these losses. The proportionality constant is denoted as in eq. 4.8.

In order to determine the loss rate  $\alpha$  due to background gas scattering processes we measured the number of atoms as a function of time and fitted the solu-

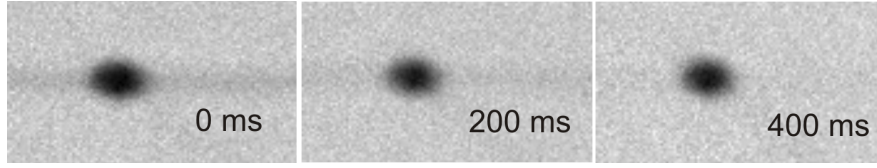


Figure 4.8: Absorption pictures of trapped atoms for several storage times after evaporation.

tion of equation  $\dot{N} = -\alpha N$ , for a certain time ( $t > 10$  s), where the atomic density is in a regime, where only background gas scattering losses occur (see figure 4.7). We observe a storage time ( $1/e$ ) of  $\tau \approx 50(5)$  s.

For a more detailed analysis the three-body losses (see above) were taken into account by fitting the solution of the differential equation  $\dot{N} = -\alpha \cdot N - \gamma \cdot N^3$ , given by equation 4.10 and shown in figure 4.7 (red curve) as function of time  $t$ .

$$N(t) = N_0 \sqrt{\frac{\alpha \cdot \exp(-2t\alpha)}{\alpha + \gamma \cdot (1 + \exp(-2t\alpha))}} \quad (4.10)$$

The lifetime in the crossed dipole trap due to background gas scattering that way determined was  $\tau \approx 56(3)$  s. The three-body loss coefficient estimated from the fit by averaging the atomic density [75, 76] is  $L_3 \approx 4 \cdot 10^{-27}$  cm<sup>6</sup>/s which is in good agreement with former measurements [76, 77].

### 4.3.3 Internal trap dynamics

Only atoms in the crossed region of the dipole trap are illuminated by the PA light. A detailed observation of the trapped atoms in the first few hundred ms after decreasing the trap depth, in order to cool by evaporation, shows remaining atoms in the "wings" of the horizontal arms of the dipole trap. The horizontal beam of the dipole trap is already applied during the MOT stages, while the tilted beam of the dipole trap is switched on after the second MOT stage and the intensity of the horizontal beam and therefore the trap depth gets ramped down. The ratio of the trap depths of the horizontal beam and the tilted beam at the end of the second MOT stage, which is the beginning of the evaporation process, is about 10:1. Storage time  $t = 0$  corresponds to the end of this evaporation process. Figure 4.8 shows absorption images of atoms in the crossed dipole trap, for several storage times right after ramping down of the dipole laser beam [62] for evaporative cooling. After a typical evaporation time of  $t_{ramp} = 600$  ms there are still atoms remaining in the horizontal

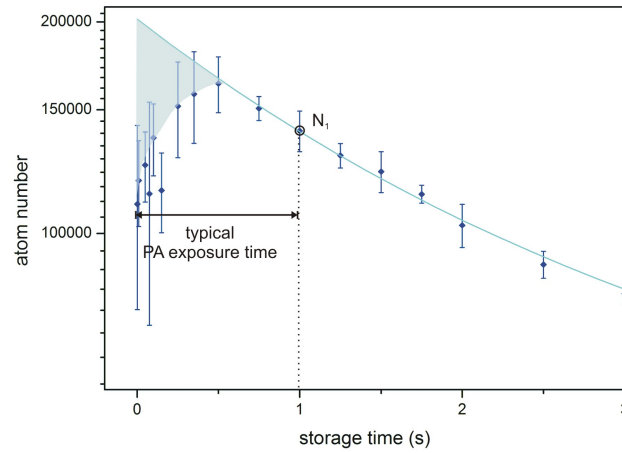


Figure 4.9: Number of trapped atoms in the crossed region of the dipole trap as a function of time after evaporation.

part, seen as faint trace of the dipole trap, not affected by the applied PA laser light. After about 400 ms additional storage time these "wing" atoms leave the horizontal arms of the dipole trap (right side of the figure).

Since the atomic density in the wings of the dipole trap is very low, no significant three-body losses are expected, being responsible for the disappearance. The life-time due to background gas collisions is orders of magnitude larger than the investigated storage time. Hence these losses do not explain the discrepancy. Furthermore this trap region is not illuminated by the PA spectroscopy laser light, which means there are also no two-body losses. The disappearance of these "wing" atoms therefore indicates an internal dynamic of atoms thermalizing with the trapped atoms at the center and get also trapped there. This effect is visible in figure 4.9, that measured the number of trapped atoms in the PA irradiated center region of the dipole trap, as a function of the storage time after evaporation.

The non-exponential decay of the atom number for larger than one second in figure 4.9 results from the three-body losses. Since not all atoms at the end of the irradiation time have been illuminated over the entire time, this leads to an underestimation of the observed loss rates, depending on the irradiation time. For measurements at low PA intensities, performed with irradiation times of several seconds, this effect can be neglected. For measurements at high PA intensities - with typical irradiation times of tens of ms - the deviation to a pure two body loss description will be discussed in the next section.

### 4.3.4 Description as pure two-body loss

The precise description, given by equation 4.8, is not capable for an analysis of the spectra. Thus we discuss in this section the suitability of the model applied for the binding energy and width investigations (chapter 2 and section 4.2), describing the losses by the solution of equation 2.3, and thus as pure two-body losses.

The typical exposure time of the PA inducing laser for high PA intensities was  $t = 30 - 50$  ms, with a typical ratio of  $N(t)_{peak}/N_1 \approx 0.3$ . A numeric calculation of eq. 4.8<sup>10</sup> leads to a deviation of  $\beta$  at the most of 20% compared to the analysis considering a pure two-body loss (eq. 2.3). For low PA intensities, the typical exposure time was  $t = 2 - 3$  s. Thus for these measurements this effect can be neglected. With respect to the uncertainty, this justifies the choice of eq. 2.3 with an approximated Voigt profile of  $\beta(\Delta)$  (see 4.1) for a description of the observed atom loss rate  $\beta$  as a two pure body loss process.

The uncertainty of the atomic loss rate  $\beta$  is given by the uncertainty of the fit to the atom loss spectra.

### 4.3.5 Estimation of $\beta_\epsilon$ for narrow natural line width

For a comparison to theoretical predictions which will be given in the next section, we have to estimate from the loss spectra giving  $\beta_{ex}$  the expected loss coefficient  $\beta_\epsilon$  corresponding to an narrow natural line-width without inhomogeneous broadening effects like Doppler- or thermal broadening (see fig. 4.10). Since for low PA light intensities the expected homogeneous line-width is very narrow due to the inhomogeneous broadening effects only a few atoms are on resonance during PA irradiation.

The loss rate for a given energy  $\beta_\epsilon$  was assumed to be  $\beta_\epsilon(I) = \frac{\alpha_V}{\alpha_L(I)} \cdot \beta_{ex}$ , where  $\beta_{ex}$  are the experimentally derived resonant loss coefficients from the fit. From figure 4.6 we get under this assumption the ratio  $\beta_{ex}/\beta_\epsilon$ , given by the ratio of the black curve - assumed to be the light intensity dependent Lorentzian shape - and the blue curve (experimental FWHM), and thus  $\frac{\alpha_V}{\alpha_L(I)}$  (compare eq. 4.7).

Three different mechanisms contribute to the uncertainty of this ratio.

<sup>10</sup>For the numeric calculation the observed loading of the "wing" atoms was described by  $N_{td} = \frac{N_w}{t_w} \exp(-\frac{t}{t_w})$ , where  $N_w$  is the number of atoms in the "wings" and  $t_w$  its loading time. The parameters were fitted to the observed time evolution given by fig. 4.9.

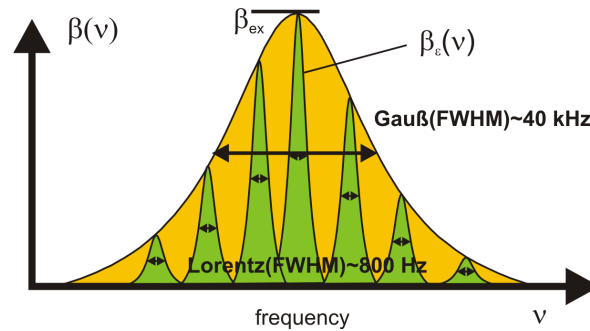


Figure 4.10: Schematic picture of the Gaussian distribution of the resonance frequency of the atoms due to their temperature (here 40 kHz for  $T=1 \mu\text{K}$ ), compared to the Lorentzian distribution of the natural line-width (here 800 Hz for low PA intensity, where no significant stimulated broadening is expected).

**Uncertainty of the correction calculation:** As ratio of the loss coefficients, we took the ratio of the FWHM Lorentzian contribution relative to the observed Voigt profile, assuming this to be a good approximation of the ratio of the plane under the functions of frequency. The high total uncertainty of the loss rate in general and this ratio in special, justifies this approximation. However this approximation leads to an uncertainty which was assumed to be 10%.

**Uncertainty of the unperturbed FWHM:** The FWHM due to thermal- and Doppler-broadening, undisturbed and un-broadened by the light intensity (see fig. 2.12), is known with an uncertainty given by the fit uncertainty and an additional uncertainty for the assumed Gaussian shape for the in fact asymmetric shape of assumed 10%.

**Uncertainty of the homogeneous power-dependent broadening:** The uncertainty of the FWHM of the Lorentzian contribution to the observable Voigt profile is further affected by the uncertainty of the formula presented in the previous section and the already mentioned uncertainty of the unbroadened FWHM. The formula (eq. 4.7) is correct to about 1% [112] and therefore can be neglected as contribution to the uncertainty. However, especially for very low PA intensities, where this ratio is large - since the ratio of the Gaussian and the Voigt width is increasing (see fig. 4.6) - the uncertainty of the Lorentzian FWHM is increasing. For very low PA intensities, I assume an uncertainty on the order of a factor of 3 for the ratio  $\alpha_L/\alpha_G$  and for high PA intensities an uncertainty of 10%.

## 4.4 Test of the theoretical model

The model of Bohn & Julienne [100] predicts PA-induced two-body loss rates  $K_{in}$  for the time evolution of the atomic density  $\dot{n}$  defined by

$$\dot{n} = -2K_{in} \cdot n^2. \quad (4.11)$$

The factor of two results from a loss of two atoms per excitation. Since the atomic density is not directly observed, I present a calculation of the average atomic density from the number of atoms in the trap, based on the trap geometry. Further we have to distinguish the contribution of the PA process from other loss processes, contributing to the experimentally observed losses. The goal of this section is, to derive a loss rate  $K_{in}^{(ex)}$  from the experimentally observed atomic loss rates  $\beta_{\epsilon}$ , comparable to  $K_{in}$  from the model.

### 4.4.1 Ratio between atom number $N$ and density $n$

In thermal equilibrium, the density distribution in a harmonic trap, is Gaussian with rms-widths  $r_{x,y,z} = \frac{1}{\omega_i} \sqrt{\frac{k_B T}{m}}$ , with the oscillator frequency  $\omega_{x,y,z}$ . This allows to express the average atomic density  $\bar{\rho}$  by

$$\bar{\rho} = \int \int \int_{\mathbb{R}^3} \frac{\rho(\vec{r})^2}{N} d\vec{r}^3 = \frac{N}{8\pi^{3/2} r_x r_y r_z}. \quad (4.12)$$

The ratio of  $\beta_{\epsilon}/K_{\epsilon}$  can be calculated from the trap parameters described in [62] by averaging the atomic density. We obtain the relation

$$K_{\epsilon} = \frac{\beta_{\epsilon}}{\left(\frac{m\omega_m^2}{2\pi k_B T}\right)^{3/2} / \sqrt{8}}, \quad (4.13)$$

where  $\omega_m = (\omega_x \cdot \omega_y \cdot \omega_z)^{1/3}$  is the geometric mean trap frequency. The trap geometry of the crossed dipole trap is a horizontal beam with a waist of  $w_1 \approx 37.5 \mu\text{m}$  and a tilted beam with a waist of  $42 \mu\text{m}$ . The angle between both beams is  $\approx 54$  degree (51 degree in the horizontal axis and 20 degree in the vertical axis). Since the tilted laser beam is 4 mm off focus<sup>11</sup>, the beam radius at the position of the horizontal beam is  $w_2 \approx 77 \mu\text{m}$ . From this trap geometry, the geometric mean trap frequency can be derived as function of the beam powers [62].

<sup>11</sup>This alignment results from an optimization of the number of trapped atoms.

The uncertainty due to the calculation of  $K_{\epsilon}$ , based on the atomic loss rate  $\beta_{\epsilon}$ , is given by several contributions:

The uncertainty of the assumed constant ratio of the density and atom number was assumed to be 10 %. More crucial is the calculation of the average atom density based on the dipole trap geometry (equation 4.13).

Three different values in this equation contribute to the uncertainty: Loss rate  $\beta_{\epsilon}$ , geometric mean trap frequency  $\omega_m$  and temperature  $T$ . The uncertainty of  $\beta_{\epsilon}$  (see previous section) was due to the fit and the assumption for the density dependence on the atom number 10-15 %, depending on the quality of the fit. According to time-of-flight measurements the uncertainty in temperature was determined to be 10 % (see chapter 2). The uncertainty of the mean trap frequency  $\omega_m$  is given by the uncertainty of the light intensity of the crossed dipole trap and the assumption for the calculation of its geometry. Since the uncertainty of the power of the dipole trap beam is less than 1 % and the waist of the beams is on the order of  $w = 37.5 \mu\text{m}$  the uncertainty of the light intensity of the crossed dipole trap is mostly depending on the uncertainty of the trap beam alignment. The dipole trap was aligned that way, that the tilted beam was adjusted to the horizontal beam, with respect to the number of trapped atoms. The uncertainty of this alignment was estimated to be on the order of  $50 \mu\text{m}$ . Since the tilted beam was typically a few mm off focus the beam radius at the position of the atoms was calculated to be  $w \approx 77 \mu\text{m}$ , leading to an assumed uncertainty in the dipole trap intensity of 30%. The uncertainty of the calculation of the mean trap frequency by trigonometry was determined to be on the order of only 1% by comparison to exact calculations [62]. Thus the uncertainty of the dipole trap intensity is the dominant contribution.

The resulting uncertainty of  $\beta/K(\omega_m)$  was calculated by the propagation of uncertainty (see eq. 4.13) and is shown in figure 4.11.

#### 4.4.2 PA contribution to the two-body losses

As we will see in the following particularly, we have to take two different phenomena into account for a comparison of  $K_{\epsilon}$  to the predicted rates  $K_{in}$ : Firstly we will discuss the possibility for a PA excitation process to occur a loss of atoms. Secondly the contribution of PA-losses to the experimentally observable two body losses.

**Photoassociation induced losses** occur once the atoms are excited to a bound molecular state. Two different processes lead to a loss of the observable trapped atoms. The excited molecule can de-excite by spontaneous emission of a photon in the ground state continuum, or in a bound state in the ground state molecular potential.

The Franck–Condon density gives the probability of a decay to a ground state kinetic energy. During PA irradiation the dipole trap was typically about  $T \approx 10 \mu\text{K}$  deep. Calculations for the six experimentally observed PA lines show, that the probability for a spontaneous decay back to a trappable thermal energy is neglectable (see fig. 3.4). Thus we assume a loss of trapped atoms for each spontaneous decay process of the excited dimer back into the ground state continuum.

The dimer can also decay into bound vibrational states of the molecular ground state. The possibilities to decay in the bound states of the ground state molecular potential are given by the Franck–Condon factors. Since we expect for long range bound states an almost similar dipole moment, compared to the atomic transition, we expect to be able to recapture at least the weak bound molecular ground states by the dipole trap. The most weakly bound molecular ground state is expected<sup>12</sup> to have a maximum binding energy  $E \approx h \cdot 5 \text{ MHz}$  (see appendix), small compared to the natural linewidth  $\Gamma \approx 34 \text{ MHz}$  of the atomic ( $^1S_0 - ^1P_1$ ) 423 nm line. Therefore, it could get photodissociated by our detection device laser beam. It was calculated, that a decay<sup>13</sup> into the most weakly bound molecular state can be neglected due to its relative probability, for the experimentally investigated molecular states (See table B.1 exemplary for the  $v' = -1; \Omega = 1$  state). More deeply bound states are not resonant to our detection device laser beam (compare expected binding energies given in table B.1) and would therefore also be observed as loss of trapped atoms. Therefore, we assume, that every decay into the molecular ground state molecule results in a loss of atoms.

Thus, we expect that every PA excitation process leads to an observable loss of atoms, no matter if it decays into the continuum or the ground state molecular potential.

---

<sup>12</sup>According to the measured background scattering length [77] and the expected  $C_6$  coefficient predictions for the binding energies are given in [114].

<sup>13</sup>The Franck–Condon factors have been calculated by Prof. Eberhard Tiemann.

**The PA contribution to the two body losses** has to be distinguished from a different two body loss processes in the presence of light: the Gallagher-Pritchard losses [103] (see chapter 3). Since we now distinguish two different two-body losses we expand equation 4.11 to:

$$\dot{n} = -2 \underbrace{(K_{PA} + K_{GP})}_{K_\epsilon} \cdot n^2, \quad (4.14)$$

where  $K_{GP}$  gives the Gallagher–Pritchard losses and  $K_{PA}$  the photoassociation induced losses. Gallagher-Pritchard losses were determined (chapter 3) to induce losses several orders of magnitude smaller than the PA induced losses and are thus neglectable.

Thus we expect that every PA process leads to an observable loss and that all observed losses are due to PA ( $K_\epsilon = K_{PA} = K_{in}^{(ex)}$ ).

### 4.4.3 Comparison of the experimentally observed loss rates and the theoretical predictions

The estimated loss rates  $K_{in}$  are compared to the theoretical predictions given by Bohn & Julienne in figure 4.11. The loss rates predicted by the model of Bohn & Julienne, based on the FCDs, given by our coupled channel model, are in fair agreement to the experimental results for low PA intensities. Thus we expect that the FCDs and therefore also the optical length, predicted by our model, are correct. However, for high PA intensities the experimental results differ significantly from the predictions.

In the model of Bohn & Julienne, the width is derived from Fermi's golden rule, assuming large width of constant density of states. This is not fulfilled here.

It was shown, that the continuous transition between the Weisskopf-Wigner exponential irreversible decay from a bound state into a continuum and the Rabi oscillation can be understood by a simple model [115]. Choosing a two level system as the other limiting case, the excitation probability scales linearly with the light intensity at low intensities. For higher intensities, the effect of stimulated emission has to be taken into account. The excitation probability  $\rho_{ee}$  can be expressed by

$$\rho_{ee} = \frac{1}{2} \frac{s_0}{1 + s_0 + (2\Delta/\Gamma_{mol})^2}, \quad (4.15)$$

with natural line width  $\Gamma_{mol}$ , light field frequency detuning  $\Delta$  and saturation

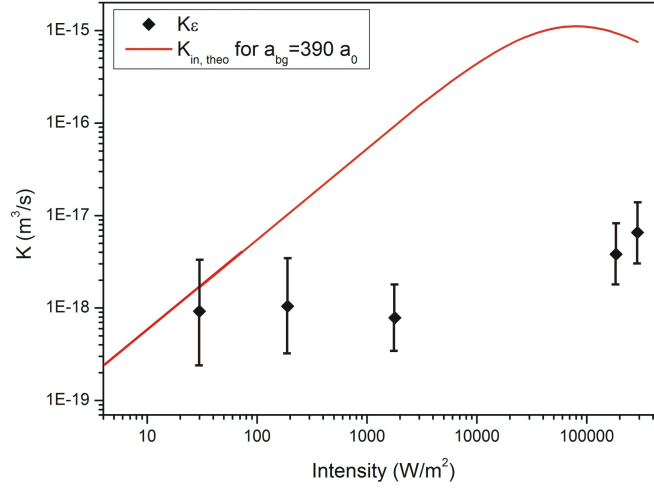


Figure 4.11: The red curve shows the inelastic two-body loss rate, given by the theoretical model for the  $v' = -1; \Omega = 1$  state, as a function of the irradiation intensity. The data for the model base on the FCD, derived from the coupled channel model, with a background scattering length of  $a_{bg} = 390 a_0$ . The black full diamonds show the experimentally derived loss rates, corrected for the most dominant thermal kinetic energy  $K_\epsilon$ .

parameter  $s_0 = I/I_{sat}$ , where  $I_{sat}$  is given by  $I_{sat} = hc\pi \frac{\Gamma_{mol}}{3\lambda^3}$ . For the atomic transition on the intercombination line ( $\Gamma_{atom} \approx 374$  Hz) this is  $I_{sat} \approx 6.5 \mu\text{W}/\text{cm}^2$  [95]. Therefore this leads to a Lorentzian line shape with a power broadened line width of  $\Gamma_{mol sat} = \Gamma_{mol} \cdot \sqrt{1 + s_0}$  and the excitation probability in a continuous wave light field saturates at  $1/2$  which might be an explanation for the observed constant loss rates  $K_{in}^{ex}$ . Equation 4.15 shows that the power broadened line width is expected to scale with the square root of the intensity, which fits better to the observed line widths (fig. 4.4 and 4.3), compared to the predicted linear dependence (eq. 3.4).

For typical high PA intensities of  $I = 70 \text{ W}/\text{cm}^2$ , this would lead for the atomic transition to  $s_0 \approx 10^4$  and thus  $\Gamma_{mol sat} \approx 75$  kHz. From the experimental point of view, we can only set an upper limit to  $\Gamma_{mol} < 10$  kHz. Thus this Ansatz as 2-level model with natural linewidths on the order of 2-3 kHz can explain the observed amount of broadening and the dependence on the intensity ( $\Delta_{PA} \propto \sqrt{I}$ ). However, the observed dependence on the temperature is not explainable by this simple model. But this is an indicator that the model for high intensities has to be enhanced to a dressed state model where the light field interaction is not only considered perturbatively.



# Chapter 5

## Conclusions and outlook

In the first part of this thesis, several milestones in the field of photoassociation were achieved and presented: The previously unknown binding energies of the three most weakly bound states in the two accessible molecular potentials,  $a\ 1_u$  and  $c\ 0_u^+$ , have been measured. We have achieved extremely low uncertainties – a few kHz over a range of tens of GHz – that are unprecedented for PA spectroscopy. Moreover, the ultra-narrow line width of the corresponding transition enables the investigation of an asymmetric line shape due to thermal broadening [63] by an enhanced line shape model [89]. Finally, a high accuracy determination of the gyromagnetic ratio was performed for each of these states, by measurements of the Zeeman splittings. These measurements reveal the change of the angular momentum coupling behavior in a molecule as a function of the internuclear separation. They allow a clear identification of the bound states to the corresponding molecular potentials.

We found that a detailed modeling of the corresponding long range molecular potentials by a coupled channel model requires both the exact binding energies and the measured gyromagnetic ratios. This led to the first experimental derivation of long range potential values for these molecules, and we found good agreement with theoretical *ab initio* calculations [70, 63].

Proceeding with the derived molecular models, in this thesis, for the first time quantitative predictions for coupling strengths and thus – by applying a theoretical model [100] – for PA losses and possible scattering length modifications by optical Feshbach resonances (OFR) in calcium were given. Our conclusions from these investigations include: The unique properties of calcium are expected to allow much larger PA intensities, compared to other alkaline earth(-like) elements in which OFR has been performed so far [99, 60] and which have been limited by density-dependent

losses, explainable as Gallagher–Pritchard losses. High intensities are predicted to lead to a larger ratio between the scattering length modification and the corresponding losses, making calcium – due to its binding energies and narrow lines – a suitable candidate for OFR.

A detailed discussion of the line shape and a quantitative analysis of the observed losses, prove the correctness of the coupled channel model and its predictions for the optical length and the applicability in the Bohn & Julienne model at low intensities.

As first improvement, with the accurate molecular potentials now available, the coupled channel model can be enhanced by increasing the accuracy of the PA spectroscopy and also by performing PA spectroscopy for more deeply bound states. The accuracy can be improved significantly by operating at lower dipole trap depths and thus at lower temperatures, since this results in smaller Doppler broadening, smaller thermal shifts, as well as smaller shifts arising from the light field of the dipole trap. The smaller signal to noise ratio due to smaller number of trapped atoms has to be compensated by statistics. For measurements of the  $\Omega = 1$  states, the  $M = 0$  state can be investigated at lower magnetic fields leading to a smaller quadratic Zeeman effect contributing to the measurement uncertainty. Also, measurements at even higher intensities are of interest, since the predicted optical length – which is proportional to the intensity – is expected to be correct and the unexpected broadening was observed to saturate at high intensities.

A second improvement of the model can be achieved by a more accurate determination of the background scattering length, since the scattering length modification by OFR depends crucially on this value. A high-accuracy two-photon spectroscopy laser system can be used for spectroscopy of the ground state molecular potential. Measurements of the most weakly bound state in the ground state molecular potential will improve the knowledge of the background scattering length by at least one order of magnitude, to first order limited only by the uncertainty of our knowledge of the  $C_6$  coefficient of the ground state molecular potential. Measurements of more deeply bound states will allow a modeling of this potential and therefore an experimental determination of the  $C_6$  coefficient, leading to further improvement of the accuracy of the background scattering length determination. For these investigations, the coupled channel model that was started in the content of this work, allows precise predictions of the Franck–Condon factors of the observed excited, bound vibrational states and the bound states in the ground state molecular

potential with  $J = 0, 2$ , which are accessible via two-photon processes.

Another application of two-photon photoassociation is the generation of ultra-cold molecules by *stimulated Raman adiabatic passage* (STIRAP). This method has been proven to be very efficient in a BEC [116], and it would give access to cold chemistry experiments.

A two-photon spectroscopy laser system was set up, in the course of this thesis and first experiments on two-color spectroscopy have been performed. These Bragg spectroscopy measurements demonstrate the potential of the system to observe narrow lines by two-photon processes. The achieved accuracy was high enough to resolve even asymmetries in the trap geometry due to gravity (see appendix).

Using the theoretical predictions given by the theoretical model, first investigations of optically induced scattering length modification in calcium have been performed by two-color spectroscopy of the phase of the ground state scattering wavefunction. However, the results of these investigations indicate that the existing models, describing the losses and scattering length modification by the interaction of light [100], do not provide a valid description of the large light-induced widths for high irradiation intensities in calcium. An investigation of the observed line shapes at high intensities indicates that applying Fermi's golden rule, on which this model is based, is not valid for the ultra-narrow system of Calcium. First calculations indicate that rather a description as two-level system might be more adequate. The unexpected broadening effect for high intensities has prevented an observation of OFR by the applied two-color detection scheme.

Let us consider alternative ideas for OFR determination:

Since the resolution of the spectroscopy of the ground state scattering wavefunction is limited by the unexpected intensity-dependent broadening, a proposal for an alternative determination of a light-induced change of the phase of the ground state scattering wavefunction was developed. It relies on PA spectroscopy at the  $^1S_0 + ^1P_1$  asymptote. Here, for PA spectroscopy near the  $^1P_1$  asymptote, the reflexion approximation is much better an assumption due to the strong dipole moment, i.e. each PA resonance at the  $^1S_0 + ^1P_1$  asymptote probes the wavefunction overlap for a well defined small range of internuclear separation around the Condon point. Furthermore the strong  $C_3$  coefficient leads to a large number of resonances close to the atomic resonance due to the molecular potential shape. Thus for measurements of a change of the phase of the ground state scattering wavefunction, several PA resonances and their amplitude can be taken into account.

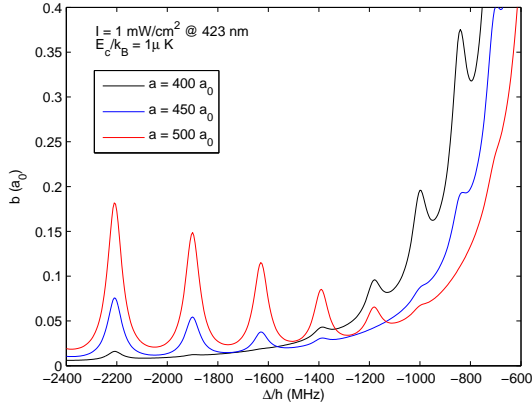


Figure 5.1: Complex scattering length  $b$ , which is directly correlated to the loss rate as a function of the binding energy  $\Delta$ , calculated for scattering lengths of  $400 a_0$  (black line),  $450 a_0$  (blue line) and  $500 a_0$  (red line)<sup>1</sup>. A modification of the scattering length shows the different internuclear separation of the node.

$-C_3/R^3$ . With  $C_3 = 0.52 \cdot 10^3 (\text{nm})^3 \text{cm}^{-1}$ , the corresponding binding energy is  $E_B(R = 20 \text{ nm})/h \approx 2 \text{ GHz}$ . PA measurements near this atomic asymptote have already been performed at temperatures in the mK range [117], where the overlap of the  $J = 1, 3, 5$  rotational states prevents a clear observation of the single resonances close to the atomic asymptote. By performing PA spectroscopy at  $\mu\text{K}$ -temperatures, where only s-wave scattering occurs, the single PA resonances ( $\Gamma_{mol} \approx 70 \text{ MHz}$ ) are expected to be resolved easily. Figure 5.1 shows calculations<sup>1</sup> of the photoassociation spectra near this internuclear separation for a weak irradiation intensity of  $I = 1 \text{ mW/cm}^2$  and a thermal energy of  $E_c = 1 \mu\text{K} \cdot k_B$ . These calculations indicate, that an optically induced scattering length modification of a few ten Bohr radii can be detected by measurements of the distribution of the loss rate amplitudes for the different resonances. Assuming a signal-to-noise ratio of 20, this method is expected to be sensitive enough to resolve even a scattering length modification of only a few Bohr radii. This detection scheme requires an additional 423 nm spectroscopy laser system.

The overlap of the wavefunctions depends most crucially on the change of the phase around the nodes of the wavefunction; thus this range of internuclear separations provides maximum sensitivity for the determination of an optically induced scattering length modification by observation of a change in the amplitudes of the loss spectra. As a first order approximation, we expect a node at an internuclear separation on the order of the background scattering length ( $a_{bg} \approx 390 a_0$ ). Since the molecular potential near the atomic asymptote is dominated by the dipole–dipole interaction, it can be described by  $V =$

<sup>1</sup>Private communication Mateusz Borkowski, Instytut Fizyki, Uniwersytet Mikołaja Kopernika, Toruń.

The highly accurate two-photon spectroscopy laser system for investigations of the ground state molecular potential developed in this work can also be used as a detection device for OFR [62] by measuring the energy shift of the most weakly bound resonance in the ground state molecular potential, which is directly correlated to the scattering length by the  $C_6$  coefficient of the ground state molecular potential [114].

Another, highly attractive tool for determination of OFR would be the creation of a BEC. Several methods have already been realized, such as investigations of the mean-field expansion of the BEC [60] or – as a more accurate method – diffraction from a standing wave [60]. A standing wave of the optical Feshbach laser induces a periodic phase shift of the wavefunction of the BEC via a change of the mean field energy by a modification of the scattering length. By releasing the atoms from the trap [29] the phase shift transforms into a separation of the atomic ensemble into several momentum components, leading to a resolvable distribution in space after some time-of-flight. The existing CCD system is, due to its geometry and since it is primarily adjusted to also investigate the MOT, not optimal for this determination method of device. A second camera system with a vertical adjustment and thus an orthogonal geometry to the standing wave would provide maximum sensitivity. Furthermore such an additional camera provides several improvements. Used only for the observation of the atoms in the dipole trap, it allows a larger magnification than the current system (1:1) and thus an improved atom number resolution. Moreover the vertical adjustment gives access to time-of-flight measurements on longer time scales. This in turn improves the accuracy of the temperature determination.

Beyond an alternative tool for OFR investigations, a BEC is also one of the most interesting application for OFR. Due to its large background scattering length, the lifetime of a Ca-BEC is limited mostly by three-body losses [77] as a function of the scattering length. The possibility of modifying the scattering length without significant PA induced losses will enable a significant increase of the BEC's lifetime.

So far, only the isotope  $^{40}\text{Ca}$  has been condensed [77]. Other bosonic isotopes cannot be trapped the same way with the required phase space density since their natural abundancies are more than one order of magnitude smaller than that of  $^{40}\text{Ca}$  (e.g.  $^{44}\text{Ca}$  - 2.09%). This leads to correspondingly smaller loading rates for the first stage of magneto-optical trapping from an atomic beam. Here we present a novel trapping technique for calcium.

As a first step towards condensation of rare bosonic isotopes in Ca, in the content of this work, it was demonstrated that (see appendix) several  $10^8$  atoms can be trapped magnetically in the quadrupole field of the MOT in the meta stable  $^3P_2$  state. The extremely long life time of this state can be used to overcome the limitation in the number of trapped atoms due to a small loading rate for isotopes with small natural abundances. We successfully repumped these atoms via the  $4s4d\ ^3D_2$  state into the ground state and re-traped them in a MOT operating on the intercombination line. The atom numbers achieved in these first experiment are expected to allow condensation (of the atoms) by further evaporative cooling in the crossed dipole trap in future experiments. Furthermore, this scheme will allow trapping and investigation of the fermionic isotope  $^{43}\text{Ca}$  (natural abundance  $\approx 0.14\%$ ).

In conclusion to wrap up, the achieved milestones in PA spectroscopy presented in this thesis, the theoretical understanding of the molecular potentials  $a$  and  $c$ , and also the understanding of high intensity PA spectroscopy and OFR in calcium has been improved. This paves the way towards OFR based applications in the quantum degenerate regime by breaking ground to novel experiments in the fields of cold chemistry (e.g. the creation of ground state molecules by two photon processes), high precision measurements of the background scattering length and modeling of the ground state molecular potential (e.g. via two-photon PA), highly accurate measurements and visualizations of scattering length modifications (e.g. PA at the  $^1P_1$  asymptote), and condensation of rare isotopes (e.g. via magnetic storing in the metastable  $^3P_2$  state). For all these experiments, the technical basis has already been realized.

# Appendix A

## Enhanced magnetical trapping of Calcium

Experiments towards quantum degeneracy in calcium have been so far limited to the only relatively abundant isotope  $^{40}\text{Ca}$  [77]. The required phase-space density for a Bose–Einstein condensation has not been achieved for other isotopes yet.

The other stable bosonic isotopes of Ca apart from  $^{40}\text{Ca}$ , with a natural occurrence at least on the order of a percent ( $^{42}\text{Ca}$ ,  $^{44}\text{Ca}$ ), also have a high background scattering length leading to large three-body losses. Optical Feshbach resonances could be applied to modify the scattering length and to overcome this limitation. They also could be used to increase the scattering length of isotope mixtures with relative small background scattering length in order to generate stable BECs.

Here an enhanced trapping mechanism is utilized, to overcome the low loading rate of a MOT from an atomic beam for isotopes with low natural abundance.

We trap atoms accumulating in the meta-stable  $^3P_2$  state (lifetime  $\approx 2 h$  [118]), leaking from the excited state  $^1P_1$  of the MOT (see fig. A.1). Because of its magnetic moment, the metastable  $^3P_2$  state can be magnetically trapped in the MOT quadrupole field as previously demonstrated with alkaline earth atoms [83, 84, 85, 119, 120]. Here at the end of the MOT phase these atoms are pumped back via the  $4s4d\ ^3D_2$  level to the atomic ground state and into the cooling cycle in order to boost the atom number and density of the MOT. This boost of the atom number leading to higher atomic densities, is also a proof of principle to trap a remarkable number of atoms magnetically. Due to the long life time of the  $^3P_2$  state, the number of trapped atoms in this state is only limited by scattering induced losses. Thus a low loading rate due to a low natural appearance can be compensated by a longer loading time.

Using a detailed rate equations model, we find good agreement with our experimentally observed loading rates and atom number in the dark state. This result also confirms the branching ratio and decay rates from the  $4s4p\ ^1P_1$  [121] and  $4s3d\ ^1D_2$  [122, 123, 124, 125].

## A.1 Experimental setup

The experimental setup is similar to the one presented in chapter 2 besides an extra grating-stabilized diode laser<sup>1</sup> for repumping operating at a wavelength of  $\lambda = 445$  nm. The frequency of this laser can be lock-in stabilized to the eigenfrequency of a reference resonator identical to that one presented in chapter 2. However, for the performance of the measurements presented here the laser was only stabilized by its internal grating cavity and the absolute frequency was measured by a wave meter<sup>2</sup>. The laser light was irradiated to the atoms after focusing by a lens.

## A.2 Storage in the $^3P_2$ state

The  $^3P_2$ -state is populated from the excited  $^1P_1$  state of the 423 nm cooling transition that decays via the  $^1D_2$  state into the triplet system.

We typically observe efficient repumping, over a frequency range of  $\approx 10$  GHz at a maximum intensity of  $I = 10$  mW.

To estimate the efficiency of the repumping we consider possible decay channels from the  $^3D_2$  state. The main decay is back to the  $^3P_2$  state and to the  $^3P_1$  state which exclusively decays with a rate  $2300\text{ s}^{-1}$  to the ground state (see fig. A.1). Other loss channels via the  $4p3d\ ^3F_2$  and the  $4s3d\ ^3D_1$  states, or via the  $5p4s\ ^3P_{1/2}$  states (not shown in fig. A.1) into the metastable state  $^3P_0$  can be neglected because of their small relative decay rates ( $\gamma(4s4d\ ^3D_2 \rightarrow 5p4s\ ^3P) \approx 8 \cdot 10^4\text{ s}^{-1}$ ) and ( $\gamma(4s4d\ ^3D_2 \rightarrow 4p4d\ ^3F) \approx 1.6 \cdot 10^4\text{ s}^{-1}$ ) [126] compared to  $\gamma(4s4d\ ^3D_2 \rightarrow 4s4p\ ^3P_1) \approx 6 \cdot 10^7\text{ s}^{-1}$ . Off resonant excitation to the  $4s4d\ ^3D_1$  state, from where the atoms could decay with a high possibility directly into the metastable  $^3P_0$  state, where they would be lost, can be neglected due to the fact that the  $^3D_1$  resonance frequency is more than 100 GHz off the  $^3D_2$  resonance.

<sup>1</sup>Toptica DL100

<sup>2</sup>High finesse WS-6

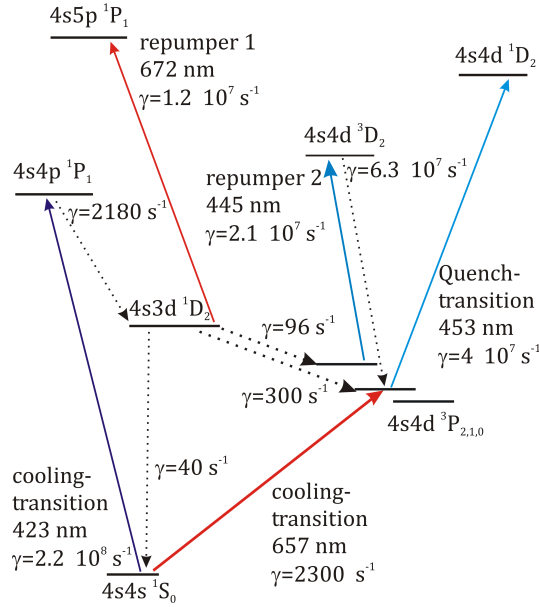


Figure A.1: Simplified energy level diagram for  $^{40}\text{Ca}$  including the natural lifetimes, showing the main cooling transitions (423 nm, and 657 nm), the quench transition for the second state of magneto-optical trapping (453 nm), decay channels via the  $^1D_2$  state into the meta-stable triplet states ( $^3P_2$  and  $^3P_1$ ), and the two repumping transitions 1 and 2 (672 nm and 445 nm)

Atoms in the  $^3P_2$  state get repumped in the  $4s4d\ ^3D_2$  state and atoms in the  $^3P_1$  state decay fast ( $\gamma \approx 2300\ \text{s}^{-1}$ ) into the ground state of the first stage MOT  $4s4p\ ^1S_0$ . Thus we expect that nearly 100% of the magnetically trapped atoms reappear in the MOT. Spatial overlap between repumper laser and magnetic trap is on the order of 50%.

Figure A.2 shows the loading curve of the atoms recaptured in the first stage MOT from the magnetically trapped  $^3P_2$  state. To detect only atoms that were magnetically trapped we first switch off the 423 nm MOT lasers, keep the quadrupole field on and wait for 100 ms to give the un-trapped atoms time to leave the trapping volume. Then the 423 nm MOT lasers, the 445 nm repumper and the 672 nm repumper are turned on.

The curve can be described by the loading the MOT from a reservoir of magnetically trapped atoms with rate coefficient  $\gamma_r$  and the lifetime of the first stage MOT, corresponding to a loss rate coefficient  $\gamma_{\text{MOT}}$ :

$$N_{\text{MOT}}(t) = N_0 e^{(-\gamma_{\text{MOT}}t)} \cdot (1 - e^{-\gamma_r t}) \quad (\text{A.1})$$

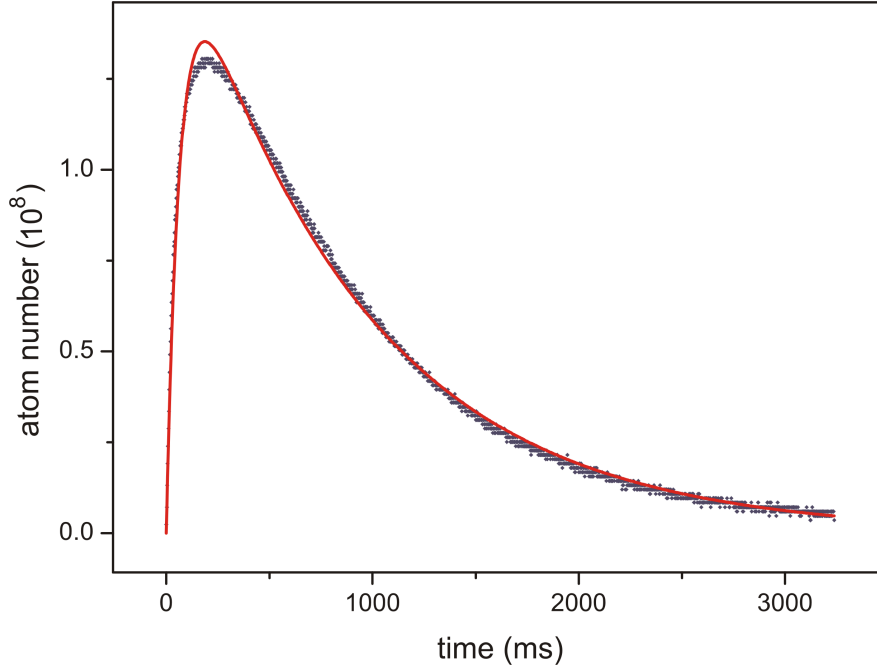


Figure A.2: The blue dots show the number of atoms repumped out of the  $^3P_2$  state and recaptured in the 423 nm MOT, as measured by the MOT fluorescence. The red curve shows the theoretical expectation of Eq. A.1.

where  $N_0$  denotes the initial number of atoms in the magnetic trap.

The fit to our experimental curve gives a life time of the first stage MOT  $\tau = 1/\gamma_{\text{MOT}} \approx 890$  ms, a repump rate coefficient  $\gamma_r \approx 14$  s $^{-1}$  and an initial atom number after one second loading time of  $N_0 \approx 1.8 \cdot 10^8$ .

The initial atom number  $N_0$  is about 40% bigger than the peak value.

To investigate the loading rate from the 423 nm MOT to the magnetic trap we vary the time the MOT is operating before the magnetically trapped atoms are detected (Fig A.3) with and without the 672 nm repump laser. The loading rate extracted from the initial slope of the experimental data (after one second, when the MOT has reached its steady state) is  $\dot{N}_0 \approx 1.8 \cdot 10^8$  s $^{-1}$  (672 nm repumper not in use) and  $\approx 1.2 \cdot 10^8$  s $^{-1}$  (672 nm repumper is used).

Even with the 672 nm repump laser  $0.8 \cdot 10^8$  atoms per second appear in magnetically trappable Zeeman-sublevels  $m_J = 1, 2$  of the  $^3P_2$  state because the larger branching ratio from the  $^1D_2$  state is compensated by the larger number of atoms in the MOT. As the 672 nm repumper increases the number of atoms in the MOT by a factor of three, a repump rate of the 672 nm repumper on the order of 1800 s $^{-1}$  would explain the observed data.

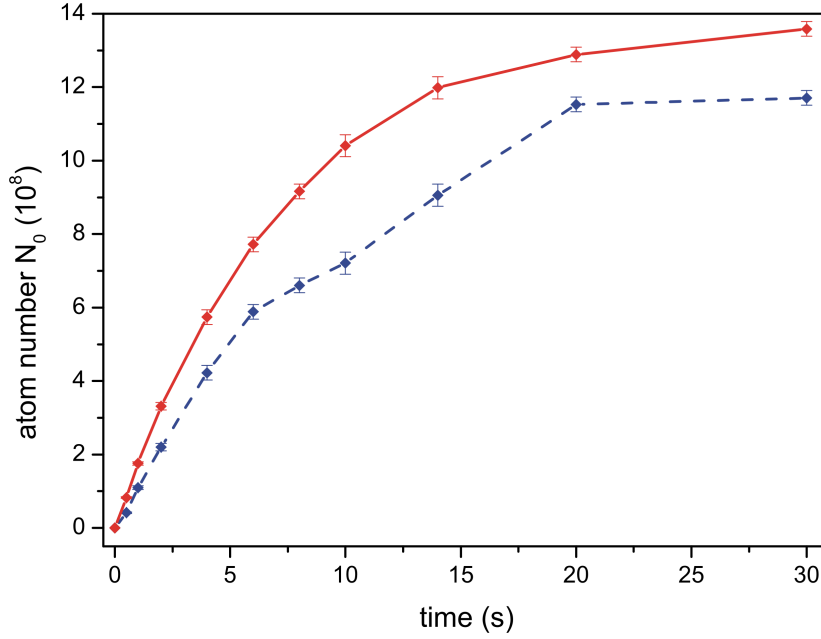


Figure A.3: Number of atoms stored in the  $^3P_2$  state as a function of the loading time from the first stage MOT without 657 nm repumper (red symbols connected by the solid line) and with 672 nm repumper (blue symbols connected by the dashed line). The uncertainty bars depict the statistical uncertainty from typically 6 measurements.

### A.3 Modeling the loading

Next we compare the measured loading rate into the magnetic trap with the value expected from available spontaneous decay rates of the involved transitions. In our model we use rate equations for transitions between individual Zeeman sub-levels of the intermediate atomic states using the relevant Clebsch-Gordon coefficients, as only the  $m_J = 1, 2$  sub-levels of the  $^3P_2$  state can be magnetically trapped.

The first step involves calculation of the populations in the Zeeman sub-levels of the  $^1P_1$  state. At the atomic position we use the magnetic field direction as quantization axis.

In equilibrium the fraction of atoms in a certain Zeeman level of the excited state  $4s4s\ ^1P_1$  of the first stage MOT is given by

$$\rho_{ee} = \frac{s}{2(1 + s_t + (2\Delta/\Gamma)^2)} \quad (\text{A.2})$$

with saturation parameter  $s = I/I_{\text{sat}}$  and  $I_{\text{sat}} = hc\pi\Gamma/3\lambda^3 = 59.9 \text{ mW/cm}^2$ , detuning  $\Delta$ , saturation coefficient due to all lasers  $s_t$  and natural decay rate  $\Gamma = 34 \text{ MHz}$ .

We assume a Zeeman splitting, given by the average magnetic field in the MOT volume and neglect Doppler shifts. The magnetic field gradient of 2.55 mT/cm along the weak axis and a  $1/\sqrt{e}$  radius of the the MOT is  $\approx 0.9$  mm, corresponding to a most probable radius of 1.4 mm leads to an average Zeeman splitting of  $\approx 3.5$  MHz.

We have a detuning of our MOT beams  $\Delta \approx -42$  MHz from the atomic resonance, and a total beam intensity at the position of the MOT of  $I = 10 \text{ mW} \cdot \text{cm}^{-2}$ , which is nearly constant over the MOT size.

From Eq. A.2 we obtain the relative distribution of the  $m_J$  magnetic sub-levels of 38% , 33% and 29% for the  $m_J = -1, 0, +1$  sub-levels, respectively, and a total excitation probability of  $\approx 1.2\%$ .

Next we calculate the population in the  $^1D_2$  state given by the equilibrium between decay rate out of the  $^1D_2$  state (without 672 nm repumper) of  $\gamma_{\text{sum}} = \gamma(^1S_0) + \gamma(^3P_1) + \gamma(^3P_2) \approx 446 \text{ s}^{-1}$  and feeding by decay rate from the upper  $^1P_1$  state of  $\gamma_0 \approx 2180 \text{ s}^{-1}$

Finally the decay into the trappable states are calculated. With a spontaneous emission decay rate  $4s4p \ ^1P_1 \rightarrow 4s3d \ ^1D_2$  of  $\gamma_1 \approx 2180 \text{ s}^{-1}$  [121] the population rate of the magnetic sub-levels  $4s3d \ ^1D_2, m_J = 0, +1, +2$  state can be calculated with the relevant Clebsch-Gordon coefficients. Collision induced decay in the  $^1D_2$  state due the lifetime of this state on the order of ms were assumed to be negligible with respect to the relatively low atom number [127]. Two-photon ionization via the  $5f4p \ ^1F_3$  state [128, 129] is not taken into account due to the fact that the 423 nm cooling laser is about 20 THz off resonance.

Due to the fact, that the  $4s4p \ ^3P_2$  state is metastable, and a loss by spontaneous emission decay can be neglected (lifetime of the  $^3P_2$  state  $\tau \approx 2$  hours [130]), the spontaneous decay rate  $\gamma(^3P_2 \rightarrow ^1S_0)$  can be assumed to be equal to zero. With respect to this circumstance we assume, that the loading rate of the magnetic trap for the trappable  $m_J = +1$ -sub-level of the  $^3P_2$  state in the magnetic field of the MOT is given by

$$\begin{aligned}
& \dot{N}({}^3P_{2,m=+1}) \\
&= N({}^1D_{2,m=0}) \cdot \gamma_2 \cdot c^2({}^1D_{2,m=0} \rightarrow {}^3P_{2,m=+1}) \\
&+ N({}^1D_{2,m=+1}) \cdot \gamma_2 \cdot c^2({}^1D_{2,m=+1} \rightarrow {}^3P_{2,m=+1}) \\
&+ N({}^1D_{2,m=+2}) \cdot \gamma_2 \cdot c^2({}^1D_{2,m=+2} \rightarrow {}^3P_{2,m=+1}) \\
&\approx 5.1 \cdot 10^8 \text{ s}^{-1},
\end{aligned} \tag{A.3}$$

with  $c$  as the relevant Clebsch-Gordan coefficients and  $\gamma_2$  as the  ${}^1D_2 \rightarrow {}^1S_0$  decay rate [83]. The average atom number in the  ${}^1D_2$  state in equilibrium is given by the solution of

$$N({}^1D_2) \cdot \gamma_{sum} = \dot{N}({}^1D_2), \tag{A.4}$$

with  $\dot{N}({}^1D_2) = N({}^1P_1) \cdot c^2 \gamma({}^1P_1 \rightarrow {}^1D_2)$  for each  $m_J$  sub-level.

Analogous calculations for the loading rate of the magnetic trap for the trapable  $m_J = 2$  sub-level gives  $\dot{N}({}^3P_{2,m_J=2}) \approx 5.3 \cdot 10^8 \text{ s}^{-1}$ .

This gives us the total loading rate of atoms trapped in the magnetic field of the MOT:

$$\dot{N}({}^3P_{m=1,2}) = \dot{N}({}^3P_{m=2}) + \dot{N}({}^3P_{m=1}) \approx 10^9 \text{ s}^{-1}.$$

## A.4 Lifetime of the magnetic trap

By varying the storage time in the magnetic trap until recapturing, we are able to measure the lifetime of the  ${}^3P_2$  state in the magnetic trap, which is shown in figure A.4. In the first 4 seconds the loss rate is increased by multi-body losses. Without loading the number of atoms in the magnetic trap decreases over time (Fig. A.4). We model the loss of atoms by the differential equation

$$\dot{N} = -N \cdot \alpha - \beta \cdot N^2, \tag{A.5}$$

with  $\alpha$  as the loss rate due to collisions with hot background gas and  $\beta$  as coefficient for inelastic two-body collisions. From the observed atom number we

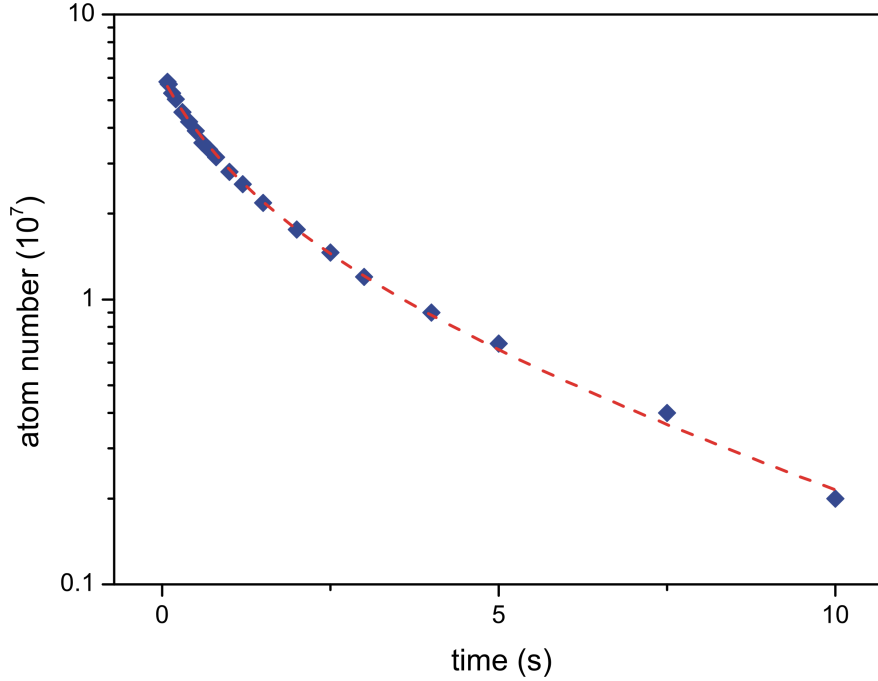


Figure A.4: Number of atoms stored in the  $^3P_2$  state depending on the storage time. The red curve shows a fit of a exponential decay after the first five seconds.

estimate the  $1/e$ -lifetime to be  $\tau \approx 4.2$  s.

This gives us a calculated loss ratio after the first 100 ms of  $N(100)/N(0) \approx 80\%$  for one second storage time in the  $^3P_2$  state. The theoretical expected loading rate at the beginning of the repump process therefore is  $10^9 \text{ s}^{-1} \cdot 0.8 \approx 8 \cdot 10^8$  atoms/s.

With respect to the fact, that the theoretically calculated loading rate of the  $^3P_2$  state has a linear dependence on the number of atoms stored in the first stage MOT, we can calculate the expected number of atoms stored in the  $^3P_2$  state after one second of loading by multiply the loading rate of  $8 \cdot 10^8$ /s with the ratio  $[\int_0^1 dt \dot{N}_{MOT}(t)]/N_{MOT}(t) \approx 83\%$ . This gives us an expected atom number at the beginning of the repump process of about  $N_{0,theo} \approx 6.6 \cdot 10^8$  atoms.

The observed ratio between the predictions and the experimental observations on the order of 30% ( $N_{0,fit}/N_{0,theo} = 1.8/6.6$ ) might be explained by the beam diameter of our repump laser, measured to be on the order of 0.3 mm, to be compared to the average distance of the atoms to the trap center in the magnetic trap on the order of  $0.6 \text{ mm}^3$ .

<sup>3</sup>The field gradient is 2.55 mT/cm and the temperature in the magnetic trap was assumed to be  $T \approx 3$  mK.

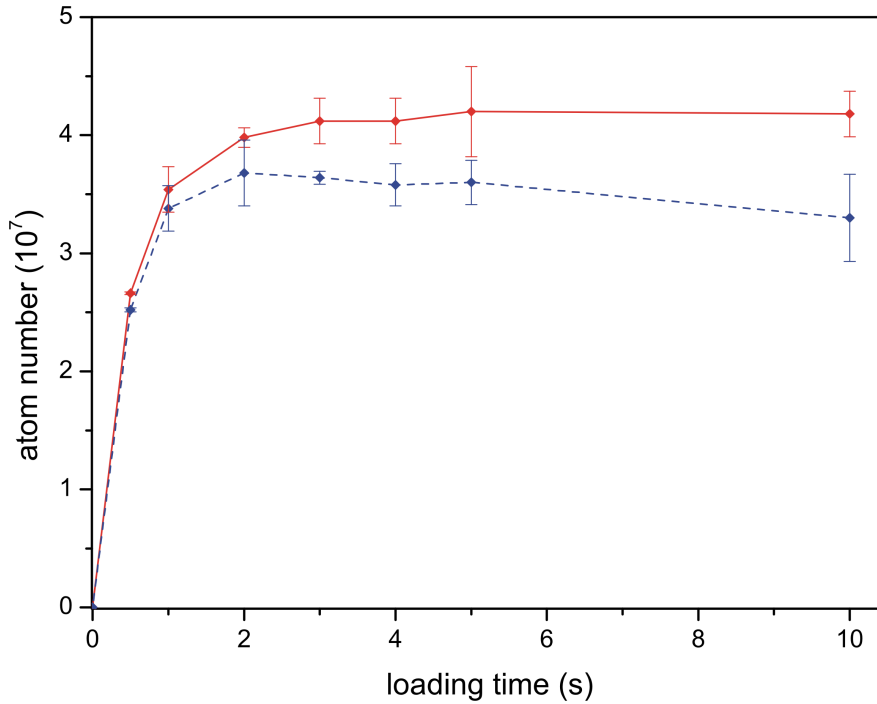


Figure A.5: Number of atoms in the second stage MOT after 350 ms. The red line shows the number of atoms with the 445 nm repump pulse, the blue dashed line shows the number of atoms without the 445 nm repump pulse.

## A.5 MOT improvements

The atoms trapped in the  $^3P_2$  state can be used to increase the number of atoms in the first stage MOT temporarily. For this the first stage MOT gets loaded for several seconds in order to give the atoms time to decay into the  $^3P_2$  state.

The atoms stored in the  $^3P_2$  state get repumped by the 445 nm repump laser system in the cooling cycle of the first stage MOT, and increase the total number of atoms temporarily, until the atom number approaches an equilibrium between the loading rate and loss mechanisms. These are mainly due to re-absorption at high density. The equilibrium after switching on the 445 nm laser is higher than before due to a higher loading rate by repumping atoms from the  $^3P_2$  state continuously.

This temporary boost of the number of atoms was used to increase the transfer efficiency from the first to the second stage MOT. For this the transfer is induced right at the time of maximum atom number in the first stage MOT due to the repumped  $^3P_2$  stage atoms. Figure A.5 shows the number of atoms in the second stage MOT after 350 ms for several storage times in the first stage MOT with and without a 445 nm repump pulse.

The temporary boost of the number of atoms in the first stage MOT results in a higher number of atoms, transferred into the second stage MOT, and increases for longer loading times of the first stage MOT, due to a longer time given to the atoms to decay via the  $^1D_2$  into the  $^3P_2$  state.

The loss of atoms in the second stage MOT, without repumping at 445 nm for long times due to a loss of atoms in the first stage MOT, for long times, caused by scattering, with an increasing number of atoms, trapped magnetically in the  $^3P_2$  state.

By accepting a loading time of 5 seconds the atom number in the second stage MOT was increased by  $\approx 20\%$ .

## A.6 Conclusion

By storing atoms magnetically in the  $^3P_2$  state, it is possible to increase the atom number, and as well the density in the first and second stage MOT, by another 20%. If one can accept a loading time of 5 s (compare fig. A.3) a significantly higher atom number and density in the final dipole trap can be achieved. This is interesting for a number of measurements where a maximum of atom density is necessary, such as measurements of three-body losses in a BEC [77, 62] or weak photo association transitions [63].

The mechanism of magnetically trapping atoms in the  $^3P_2$  state could also be used to trap rare isotopes and was already applied to Sr [120]. For rare Calcium isotopes, like  $^{44}\text{Ca}$  (2.09%) or the fermionic isotope  $^{43}\text{Ca}$  (0.14%) a smaller loading rate caused by the low abundancy of these isotopes in the atomic beam can be balanced by an increased loading time due to the long lifetime of the  $^3P_2$  state ( $\approx 2$  h).

# Appendix B

## Multi color spectroscopy

In chapter 2, I presented photoassociation spectroscopy with single photons. The measurements of the phase modification of the ground state scattering presented in chapter 3, used two spectroscopy lasers for a single photon excitation each. Besides these single photon processes also multi-photon transitions can be used for photoassociation. In this chapter I will discuss the use of two of these processes for a future high accuracy determination of the background scattering length and will also present first tests of the experimental setup to prove the suitability of the laser system to observe two-photon processes with high accuracy by Bragg spectroscopy.

### B.1 Two photon photoassociation spectroscopy

Since the scattering length depends crucially on the binding energy of the most weakly bound state in the ground state molecular potential, the background scattering length can be determined by two-color PA spectroscopy of the most weakly bound states in the ground state molecular potential. The scheme of this excitation is shown in figure B.1. Depending on the  $C_6$  coefficient of the ground state molecular potential ab initio calculation allow predictions for the scattering length [114]. The accuracy of this experimental determination of the scattering length is expected to be at the least one order of magnitude higher compared to previous experimental determinations [76].

In table B.1 the binding energies relative<sup>1</sup> to the  $^1S_0 + ^1S_0$  atomic asymptote are given with a total angular momentum of  $J = 0, 2$  that can be accessed by a two-

---

<sup>1</sup>Calculated by Prof. Eberhard Tiemann.

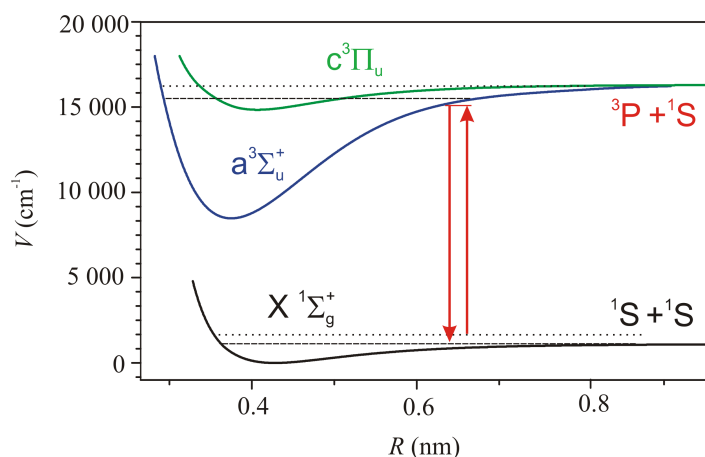


Figure B.1: Molecular potential scheme for a two photon transition into a bound state in the ground state molecular potential  $^1\Sigma_g^+$  via a virtual state close to a bound state in one of the excited molecular potentials  $a$  and  $c$ .

photon process. The probability in which bound molecular ground state the excited molecule decays, is given by the Franck–Condon factors of the wavefunction of both bound molecular states. The Franck–Condon factors in table B.1 derived from the coupled channel model are exemplary given for the  $v' = -1; \Omega = 1$  state<sup>2</sup>.

state	binding energy	FCF
$v$   $J$	( $\text{cm}^{-1}$ )	( $1/\text{cm}^{-1}$ )
40   0	-0.00003	0.0045
39   2	-0.0324721	
39   0	-0.04516	0.54
38   2	-0.2726834	
38   0	-0.29632	0.0038
37   2	-0.9003459	
37   0	-0.93456	0.00022
36   0	-2.14116	0.000016
35   0	-4.09246	0.000013

Table B.1: Franck–Condon factors calculated for the ground state molecular states  $v = 35 - v = 40$  and the excited  $v' = -1; \Omega = 1$  bound state. Furthermore the binding energies of the corresponding molecular ground states relative to the atomic  $^1S_0$  state is given as well as their total angular momentum  $J$ .

Experimentally two processes can be used to observe the bound states in the ground state molecular potential: Autler–Townes or Raman spectroscopy. Both techniques have already been performed for alkaline earth(-like) elements  $^{88}\text{Sr}$  [131] and

<sup>2</sup>Calculated by Prof. Eberhard Tiemann.

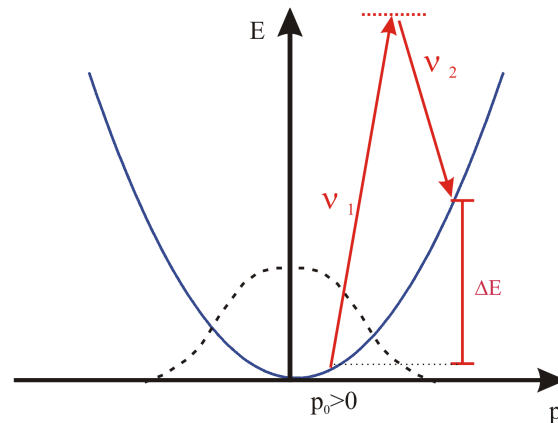


Figure B.2: Schematic picture of the transfer of momentum and energy to the atoms by a two-photon process. The blue line indicates the kinetic energy  $E$  of the atoms as function of their momentum  $p$ . The dashed line indicates the thermal momenta distribution of the atomic cloud. As an example  $p_0$  is the initial momentum of the atom.  $\nu_1$  is the energy of the absorbed photon of laser 1,  $\nu_2$  the energy of the stimulated emitted photon of the second spectroscopy laser with a difference energy of  $\Delta E$ .

six different types of isotopes of Yb [132]. The knowledge of the Franck–Condon factors allows a goal orientated spectroscopy, since the coupling strength of the two-photon process can now be calculated.

## B.2 Bragg spectroscopy

The capability of the two-photon laser system was tested by Bragg spectroscopy of the atoms in the crossed dipole trap. Applying the spectroscopy laser beams in anti-parallel configuration we can heat the atomic ensemble by inducing a double photon recoil. The process is schematically shown in figure B.2.

The experimental setup is similar to the one presented in chapter 2 and 3 for the measurements of the optical Feshbach resonances. Two spectroscopy lasers with a maximum intensity of up to  $I = 150 \text{ W/cm}^2$ , can be used to irradiate the atoms with a frequency detuning of up to 40 GHz, relative to the atomic  $^3P_1$  asymptote and up to 1 GHz<sup>3</sup> relative to each other.

Since we are interested in the application of energies on the order of the photon recoil one laser light frequency is fixed and the other is varied shot by shot

<sup>3</sup>The limitation is currently due to the photo diode. For investigations of bound states in the  $X$  potential besides the  $v = 40 \ J = 0$  state the beat lock would require a faster photo diode.

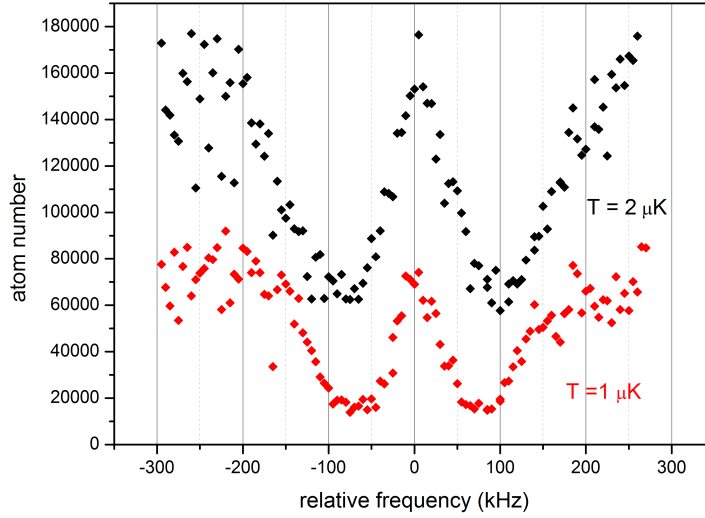


Figure B.3: Number of trapped atoms as a function of the light frequency difference of the two spectroscopy lasers.

in the kHz-range. If the relative frequency fulfills the law of energy conservation broadened by the thermal distribution of the atomic ensemble the recoil, due to the absorption of the applied photons increases the kinetic energy and heats therefore the atomic cloud in the trap. The higher kinetic energy leads to an evaporation loss process of atoms from the trap over time. This loss of atoms as function of the relative light field frequency (relative energy of the photons) can be measured by our absorption imaging as atom number detection device.

In figure B.3 such a measurement is shown. The initial temperature of the atomic ensemble was  $T \approx 1 \mu\text{K}$  at a trap depth of  $U_0 \approx 10 \mu\text{K}$  and  $T \approx 2 \mu\text{K}$ .

The recoil induced heating process was resolvable by the distribution in space of the atomic cloud after a time delay. Figure B.4 shows the width - which is correlated to the temperature - of the atomic cloud in the horizontal axis after a time-of-flight of  $\tau = 100 \mu\text{s}$ , as a function of the relative frequency of the applied spectroscopy lasers. Since the weak beam of the crossed dipole trap is tilted, corresponding to the horizontal axis, this results in a different trap depth along this axis due to gravitation. Thus, the asymmetry in the trap depth and therefore in the necessary kinetic energy, which has to be applied in order to overcome the trap potential, has a dependency on the direction. The two spectroscopy lasers, are almost parallel and anti-parallel to this tilted beam. Therefore since  $\nu_1 > \nu_2$  and  $\nu_2 > \nu_1$  result

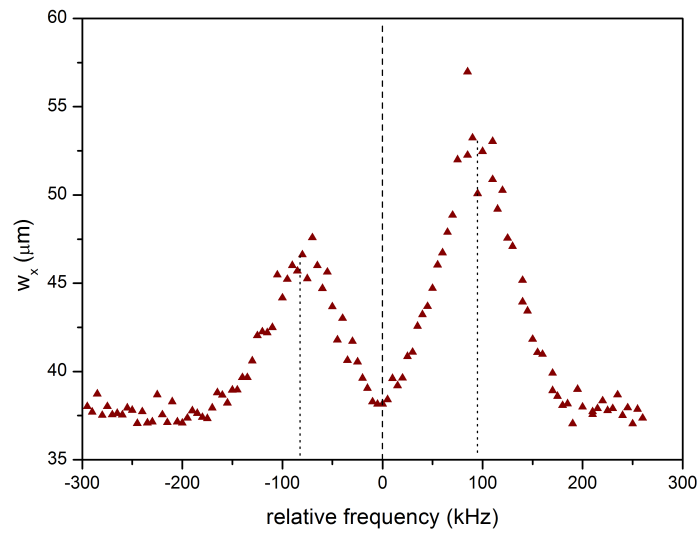


Figure B.4: Vertical distribution  $w_x$  of the atomic cloud after  $t = 100 \mu\text{s}$  time-of-flight as a function of the relative light frequency of the two spectroscopy lasers.

in different directions in space of the applied photon momenta along this axis the asymmetry of the kinetic energy of in the trap remaining atoms as well as the asymmetry of the difference energy at which a maximum of losses is applied indicate the asymmetry in the trap geometry.

The presented Bragg spectroscopy allows an investigation of the depth and also the geometry of the crossed dipole trap. Further it proves the capability of the experimental setup to perform high accuracy multi-photon spectroscopy, paving the way towards two-photon PA of the ground state continuum.



# Bibliography

- [1] Long A.A. (Ed.) (1999) The Cambridge Companion to Early Greek Philosophy. Cambridge University Press
- [2] wikipedia, retrieved 12th may 2014
- [3] Fritzsch H. (2004) Elementarteilchen: Bausteine der Materie. C.H.Beck
- [4] Hecht E., Zajac A. (1980) Optics. Addison-Wesley, Reading MA, Amsterdam, London, 6 edition
- [5] Durant W. (1956) Das Vermächtnis des Ostens - Eine Kulturgeschichte Asiens
- [6] Peter Precht F.P.B. (1999) Metzler Philosophie Lexikon. Begriffe und Definitionen. J.B. Metzler
- [7] Newton I. (1687) Philosophiae naturalis principia mathematica
- [8] Rutherford E. (1911) The scattering of  $\alpha$  and  $\beta$  particles by matter and the structure of the atom. Philosophical Magazine. **21**, 669–688
- [9] Gell-Mann M. (1964) A schematic model of baryons and mesons. Phys. Lett. **8**, 214–215
- [10] Donoghue J.F. (1994) Dynamics of the Standard Model. Cambridge University Press
- [11] Randerson J. (30th June 2008) Father of the 'god particle'. The Guardian
- [12] Higgs P. (1964) Broken symmetries, massless particles and gauge fields. Physics Letters. **12**, 132–133
- [13] CERN (2012) CERN experiments observe particle consistent with long-sought Higgs boson. CERN press release. **17.12**, 1

- [14] Baird F.E. (1961) From Plato to Derrida. Upper Saddle River, New Jersey: Pearson Prentice Hall
- [15] Maxwell J.C. (1865) A dynamical theory of the electromagnetic field. Phil. Trans. R. Soc. Lond. **155**, 459–512
- [16] Michelson A.A., Morley E.M. (1887) On the relative motion of the earth and the luminiferous ether. American Journal of Science - Third Series. **XXXIV**(203), 333–345
- [17] Einstein A. (1905) Zur Elektrodynamik bewegter Körper. Annalen der Physik. **17**, 891–921
- [18] Cahan D. (1993) Hermann von Helmholtz and the Foundations of Nineteenth-Century Science. University of California Press
- [19] Gordon J.P., Zeiger H.J., Townes C.H. (1955) The maser-new type of microwave amplifier, frequency standard, and spectrometer. Phys. Rev. **99**, 1264–1274
- [20] Schawlow A.L., Townes C.H. (1958) Infrared and optical masers. Phys. Rev. **112**, 1940–1949
- [21] Ashkin A. (2006) Optical trapping and manipulation of neutral particles using lasers. World Scientific
- [22] Hänsch T.W., Schawlow A.L. (1975) Cooling of gases by laser radiation. Opt. Commun. **13**, 68–69
- [23] Wineland D.J., Itano W.M. (1979) Laser cooling of atoms. Phys. Rev. A. **20**, 1521–1540
- [24] Einstein A. (1925) Quantentheorie des einatomigen idealen Gases. Zweite Abhandlung. Sitzungsberichte der Preussischen Akademie der Wissenschaften. **1**, 3–14
- [25] Falke S., Schnatz H., Vellore Winfred J.S.R., Middelman T., Vogt S., Weyers S., Lipphardt B., Grosche G., Riehle F., Sterr U., Lisdat C. (2011) The <sup>87</sup>Sr optical frequency standard at PTB. Metrologia. **48**, 399–407

- [26] Lemke N.D., Ludlow A.D., Barber Z.W., Fortier T.M., Diddams S.A., Jiang Y., Jefferts S.R., Heavner T.P., Parker T.E., Oates C.W. (2009) Spin-1/2 optical lattice clock. *Phys. Rev. Lett.* **103**, 063001–1–4
- [27] Feshbach H. (1958) Unified theory of nuclear reactions. *Annals of Physics.* **5**(4), 357–390
- [28] Fano U. (1935) On the absorption spectrum of noble gases at the arc spectrum limit. *Nuovo Cimento.* **12**, 154–161. engl. translation in: *J. Res. Natl. Inst. Stand. Technol.* **110**, 583–587 (2005)
- [29] Yamazaki R., Taie S., Sugawa S., Takahashi Y. (2010) Submicron scale spatial modulation of an interatomic interaction in a Bose-Einstein condensate. *Phys. Rev. Lett.* **105**, 050405–1–4
- [30] Regal C.A., Ticknor C., Bohn J.L., Jin D.S. (2003) Creation of ultracold molecules from a Fermi gas of atoms. *Nature.* **424**, 47–50
- [31] Bartenstein M., Altmeyer A., Riedl S., Jochim S., Chin C., Hecker Denschlag J., Grimm R. (2004) Collective excitations of a degenerate gas at the BEC-BCS crossover. *Phys. Rev. Lett.* **92**, 203201–1–4
- [32] Kraemer T., Mark M., Waldburger P., Danzl J.G., Chin C., Engeser B., Lange A.D., Pilch K., Jaakkola A., Nägerl H.C., Grimm R. (2006) Evidence for Efimov quantum states in an ultracold gas of caesium atoms. *Nature.* **440**, 315–318
- [33] Tiesinga E., Moerdijk A.J., Verhaar B.J., Stoof H.T.C. (1992) Conditions for Bose-Einstein condensation in magnetically trapped atomic cesium. *Phys. Rev. A.* **46**, R1167–R1170
- [34] Tiesinga E., Verhaar B.J., Stoof H.T.C. (1993) Threshold and resonance phenomena in ultracold ground-state collisions. *Phys. Rev. A.* **47**, 4114–4122
- [35] Moerdijk A.J., Verhaar B.J., Axelsson A. (1995) Resonances in ultracold collisions of  ${}^6\text{Li}$ ,  ${}^7\text{Li}$ , and  ${}^{23}\text{Na}$ . *Phys. Rev. A.* **51**, 4852–4861
- [36] Vogels J.M., Tsai C.C., Freeland R.S., Kokkelmans S.J.J.M.F., Verhaar B.J., Heinzen D.J. (1997) Prediction of Feshbach resonances in collisions of ultracold rubidium atoms. *Phys. Rev. A.* **56**, R1067–R1070

- [37] Boesten H.M.J.M., Vogels J.M., Tempelaars J.G.C., Verhaar B.J. (1996) Properties of cold collisions of  $^{39}\text{K}$  atoms and of  $^{41}\text{K}$  atoms in relation to Bose-Einstein condensation. *Phys. Rev. A.* **54**, R3726–R3729
- [38] Moerdijk A.J., Verhaar B.J., Nagtegaal T.M. (1996) Collisions of dressed ground-state atoms. *Phys. Rev. A.* **53**, 4343–4351
- [39] Inouye S., Andrews M.R., Stenger J., Miesner H.J., Stamper-Kurn D.M., Ketterle W. (1998) Observation of Feshbach resonances in a Bose-Einstein condensate. *Nature.* **192**, 151–154
- [40] van Abeelen F.A., Heinzen D.J., Verhaar B.J. (1998) Photoassociation as a probe of Feshbach resonances in cold-atom scattering. *Phys. Rev. A.* **57**, R4102–R4105
- [41] Thorsheim H.R., Weiner J., Julienne P.S. (1987) Laser-induced photoassociation of ultracold sodium atoms. *Phys. Rev. Lett.* **58**, 2420–2423
- [42] Fatemi F.K., Jones K.M., Lett P.D. (2000) Observation of optically induced Feshbach resonances in collisions of cold atoms. *Phys. Rev. Lett.* **85**, 4462–4465
- [43] Fedichev P.O., Kagan Y., Shlyapnikov G.V., Walraven J.T.M. (1996) Influence of nearly resonant light on the scattering length in low-temperature atomic gases. *Phys. Rev. Lett.* **77**(14), 2913–2916
- [44] Bohn J.L., Julienne P.S. (1997) Prospects for influencing scattering lengths with far-off-resonant light. *Phys. Rev. A.* **56**, 1486–1491
- [45] Steinmeyer G., Sutter D.H., Gallmann L., Matuschek N., Keller U. (1999) Frontiers in ultrashort pulse generation: Pushing the limits in linear and nonlinear optics. *Science.* **286**, 1507–1512
- [46] Theis M., Thalhammer G., Winkler K., Hellwig M., Ruff G., Grimm R., Hecker Denschlag J. (2004) Tuning the scattering length with an optically induced Feshbach resonance. *Phys. Rev. Lett.* **93**, 123001
- [47] Ciuryło R., Tiesinga E., Julienne P.S. (2005) Optical tuning of the scattering length of cold alkaline-earth-metal atoms. *Phys. Rev. A.* **71**, 030701–1–4

- [48] Rosenband T., Hume D.B., Schmidt P.O., Chou C.W., Brusch A., Lorini L., Os-  
kay W.H., Drullinger R.E., Fortier T.M., Stalnaker J.E., Diddams S.A., Swann  
W.C., Newbury N.R., Itano W.M., Wineland D.J., Bergquist J.C. (2008) Fre-  
quency ratio of  $\text{Al}^+$  and  $\text{Hg}^+$  single-ion optical clocks; metrology at the 17th  
decimal place. *Science*. **319**, 1808–1812
- [49] Margolis H.S., Barwood G.P., Huang G., Klein H.A., Lea S.N., Szymaniec K.,  
Gill P. (2004) Hertz-level measurement of the optical clock frequency in a  
single  $^{88}\text{Sr}^+$  ion. *Science*. **306**, 1355–1358
- [50] Schneider T., Peik E., Tamm C. (2005) Sub-Hertz optical frequency compar-  
isons between two trapped  $^{171}\text{Yb}$  ions. *Phys. Rev. Lett.* **94**, 230801–1–4
- [51] Swallows M.D., Bishof M., Lin Y., Blatt S., Martin M.J., Rey A.M., Ye J. (2011)  
Suppression of collisional shifts in a strongly interacting lattice clock. *Science*.  
**331**, 1043–1046
- [52] Campbell G.K., Boyd M.M., Thomsen J.W., Martin M.J., Blatt S., Swallows  
M.D., Nicholson T.L., Fortier T., Oates C.W., Diddams S.A., Lemke N.D.,  
Naidon P., Julienne P., Ye J., Ludlow A.D. (2009) Probing interactions between  
ultracold fermions. *Science*. **324**, 360–363
- [53] Chou C.W., Hume D.B., Thorpe M.J., Wineland D.J., Rosenband T. (2011)  
Quantum coherence between two atoms beyond  $q = 10^{15}$ . *Phys. Rev. Lett.*  
**106**(16), 160801
- [54] Lorini L., Ashby N., Brusch A., Diddams S., Drullinger R., Fortier E.E.T., Hast-  
ings P., Heavner T., Hume D., Itano W., Jefferts S., Newbury N., Parker T.,  
Rosenband T., Stalnaker J., Swann W., Wineland D., Bergquist J. (2008) Recent  
atomic clock comparisons at nist. *Eur. Phys. J. Special Topics*. **163**, 19–35
- [55] Szymaniec K., Chałupczak W., Tiesinga E., Williams C.J., Weyers S., Wynands  
R. (2007) Cancellation of the collisional frequency shift in caesium fountain  
clocks. *Phys. Rev. Lett.* **98**, 153002–1–4
- [56] Yamazaki R., Taie S., Sugawa S., Enomoto K., Takahashi Y. (2013) Observation  
of a p-wave optical Feshbach resonance. *Phys. Rev. A*. **87**, 010704
- [57] Enomoto K., Kasa K., Kitagawa M., Takahashi Y. (2008) Optical Feshbach  
resonance using the intercombination transition. *Phys. Rev. Lett.* **101**, 203201

- [58] Zelevinsky T., Boyd M.M., Ludlow A.D., Ido T., Ye J., Ciuryło R., Naidon P., Julienne P.S. (2006) Narrow line photoassociation in an optical lattice. *Phys. Rev. Lett.* **96**, 203201
- [59] Blatt S. (2011) Ultracold Collisions and Fundamental Physics with Strontium. PhD thesis, University of Colorado
- [60] Yan M., DeSalvo B.J., Ramachandhran B., Pu H., Killian T.C. (2013) Controlling condensate collapse and expansion with an optical Feshbach resonance. *Phys. Rev. Lett.* **110**, 123201
- [61] Degenhardt C., Stoehr H., Lisdat C., Wilpers G., Schnatz H., Lipphardt B., Nazarova T., Pottie P.E., Sterr U., Helmcke J., Riehle F. (2005) Calcium optical frequency standard with ultracold atoms: Approaching  $10^{-15}$  relative uncertainty. *Phys. Rev. A.* **72**, 062111–1–17
- [62] Appel O. (2013) Bose-Einstein Condensation and Narrow-Line Photoassociation Spectroscopy of Calcium. PhD thesis, Fakultät für Mathematik und Physik der Gottfried Wilhelm Leibniz Universität Hannover. 08/2013 eingereichte Version
- [63] Ciuryło R., Tiesinga E., Kotochigova S., Julienne P.S. (2004) Photoassociation spectroscopy of cold alkaline-earth-metal atoms near the intercombination line. *Phys. Rev. A.* **70**, 062710–1–14
- [64] Boisseau C., Audouard E., Vigué J., Julienne P.S. (2000) Reflection approximation in photoassociation spectroscopy. *Phys. Rev. A.* **62**, 052705–1–10
- [65] R. J. Le Roy Bernstein (1970) *J. Chem. Phys.* **52**, 3869
- [66] Raab P., Friedrich H. (2008) Quantization function for deep potentials with attractive tails. *Phys. Rev. A.* **78**, 022707
- [67] R.J. Le Roy Bernstein (1980)
- [68] Herzberg G. (1950) *Molecular Spectra and Molecular Structure: I. Spectra of Diatomic Molecules.* D. van Nostrand company, Inc., Toronto, New York, London, 2nd edition
- [69] Born M., Oppenheimer R. (1927) Zur Quantentheorie der Molekeln. *Annalen der Physik.* **20**(84), 457–484

- [70] Mitroy J., Zhang J.Y. (2008) Properties and long range interactions of the calcium atom. *J. Chem. Phys.* **128**, 134305
- [71] Allard O., Falke S., Pashov A., Dulieu O., Knöckel H., Tiemann E. (2005) Study of coupled states for the  $(4s^2)^1S + (4s4p)^3P$  asymptote of  $\text{Ca}_2^*$ . *Eur. Phys. J. D.* **35**, 483–497
- [72] Wilpers G. (2002) Ein Optisches Frequenznormal mit kalten und ultrakalten Atomen. PTB-Bericht PTB-Opt-66 (ISBN 3-89701-892-6), Physikalisch-Technische Bundesanstalt, Braunschweig. Dissertation, University of Hannover
- [73] Wilpers G., Binnewies T., Degenhardt C., Sterr U., Helmcke J., Riehle F. (2001) An optical frequency standard with cold calcium atoms. *Annales Françaises des Microtechniques et de Chronométrie.* **50**, 15–27
- [74] Degenhardt C. (2004) Freie und gespeicherte Calcium-Atome für ein optisches Frequenznormal. PhD thesis, Universität Hannover, Welfengarten 1. online available at <http://www.tib.uni-hannover.de>
- [75] Vogt F., Grain C., Nazarova T., Sterr U., Riehle F., Lisdat C., Tiemann E. (2007) Determination of the calcium ground state scattering length by photoassociation spectroscopy at large detunings. *Eur. Phys. J. D.* **44**, 73–79
- [76] Vogt F. (2009) Creation of cold and dense ensembles of calcium atoms. PhD thesis, Gottfried Wilhelm Leibniz Universität Hannover. Online available at <http://www.tib.uni-hannover.de>
- [77] Kraft S., Vogt F., Appel O., Riehle F., Sterr U. (2009) Bose-Einstein condensation of alkaline earth atoms:  $^{40}\text{Ca}$ . *Phys. Rev. Lett.* **103**, 130401
- [78] Meschede D. (1999) *Optik, Licht und Laser*. Teubner Studienbücher
- [79] Nazarova T. (2007) Towards the Quantum Noise Limit in Ramsey-Bordé Atom Interferometry. PhD thesis, Fakultät für Mathematik und Physik der Gottfried Wilhelm Leibniz Universität Hannover. Online available at <http://www.tib.uni-hannover.de>
- [80] Walker T., Sesko D., Wieman C. (1990) Collective behavior of optically trapped neutral atoms. *Phys. Rev. Lett.* **64**, 408–411

- [81] Prentiss M., Cable A., Bjorkholm J.E., Chu S., Raab E.L., Pritchard D.E. (1988) Atomic-density-dependent losses in an optical trap. *Opt. Lett.* **13**(6), 452–454
- [82] Ketterle W., Davis K.B., Joffe M.A., Martin A., Pritchard D.E. (1993) High densities of cold atoms in a dark spontaneous-force optical trap. *Phys. Rev. Lett.* **70**, 2253–2256
- [83] Loftus T., Bochinski J.R., Mossberg T.W. (2002) Magnetic trapping of ytterbium and the alkaline-earth metals. *Phys. Rev. A.* **66**, 013411
- [84] Nagel S.B., Simien C.E., Laha S., Gupta P., Ashoka V.S., Killian T.C. (2003) Magnetic trapping of metastable  $^3P_2$  atomic strontium. *Phys. Rev. A.* **67**(1), 011401
- [85] Yasuda M., Katori H. (2004) Lifetime measurement of the  $^3P_2$  metastable state of strontium atoms. *Phys. Rev. Lett.* **92**(15), 153004
- [86] Stoehr H. (2004) Diodenlaser mit Hertz-Linienbreite für ein optisches Calcium-Frequenznormal. PhD thesis, Universität Hannover, Universität Hannover. in German, urn:nbn:de:gbv:089-4850973620
- [87] Dubé P., Madej A., Bernard J., Marmet L., Shiner A. (2009) A narrow linewidth and frequency-stable probe laser source for the  $^{88}\text{Sr}^+$  single ion optical frequency standard. *Appl. Phys. B.* **95**, 43–54
- [88] Comparat D. (2004) Improved LeRoy–Bernstein near-dissociation expansion formula, and prospect for photoassociation spectroscopy. *J. Chem. Phys.* **120**, 1318–1329
- [89] Jones K.M., Lett P.D., Tiesinga E., Julienne P.S. (1999) Fitting line shapes in photoassociation spectroscopy of ultracold atoms: A useful approximation. *Phys. Rev. A.* **61**, 012501–1–11
- [90] Kahmann M., Tiemann E., Appel O., Sterr U., Riehle F. (2014) Photoassociation spectroscopy of  $^{40}\text{Ca}$  measured with kilohertz accuracy near the  $^3P_1+^1S_0$  asymptote and its Zeeman effect. *Phys. Rev. A.* **89**, 023413
- [91] Weidemüller M., Zimmermann C. *Cold Atoms and Molecules*

- [92] Brown J.M., Carrington A. (2003) Rotational Spectroscopy of Diatomic Molecules. Cambridge University Press
- [93] Beverini N., Maccioni E., Strumia F. (1998)  $g_J$  factor of neutral calcium  $^3P$  metastable levels. J. Opt. Soc. Am. B. **15**, 2206–2209
- [94] Kato S., Yamazaki R., Shibata K., Yamamoto R., Yamada H., Takahashi Y. (2012) Observation of long-lived van der Waals molecules in an optical lattice. Phys. Rev. A. **86**, 043411
- [95] Metcalf H.J., van der Straten P. (1999) Laser Cooling and Trapping. Springer, New York, Berlin, Heidelberg
- [96] Köhler T., Góral K., Julienne P.S. (2006) Production of cold molecules via magnetically tunable Feshbach resonances. Rev. Mod. Phys. **78**, 1311–1361
- [97] Ciuryło R., Tiesinga E., Julienne P.S. (2006) Stationary phase approximation for the strength of optical Feshbach resonances. Phys. Rev. A. **74**, 022710
- [98] Fedichev P.O., Reynolds M.W., Shlyapnikov G.V. (1996) Three-body recombination of ultracold atoms to a weakly bound  $s$  level. Phys. Rev. Lett. **77**, 2921–2924
- [99] Enomoto K., Kitagawa M., Tojo S., Takahashi Y. (2008) Hyperfine-structure-induced purely long-range molecules. Phys. Rev. Lett. **100**, 123001–1–4
- [100] Bohn J.L., Julienne P.S. (1999) Semianalytic theory of laser-assisted resonant cold collisions. Phys. Rev. A. **60**, 414–425
- [101] Napolitano R., Weiner J., Williams C.J., Julienne P.S. (1994) Line shapes of high resolution photoassociation spectra of optically cooled atoms. Phys. Rev. Lett. **73**, 1352–1355
- [102] Allard O. (2004) Long-Range Interactions in the Calcium Dimer studied by Molecular Spectroscopy. PhD thesis, Universität Hannover, Welfengarten 1. online available at <http://www.tib.uni-hannover.de>
- [103] Gallagher A., Pritchard D.E. (1989) Exoergic collisions of cold  $\text{Na}^*$ -Na. Phys. Rev. Lett. **63**, 957–960

- [104] Blatt S., Nicholson T.L., Bloom B.J., Williams J.R., Thomsen J.W., Julienne P.S., Ye J. (2011) Measurement of optical Feshbach resonances in an ideal gas. *Phys. Rev. Lett.* **107**, 073202
- [105] Julienne P.S. (1996) Cold binary atomic collisions in a light field. *J. Res. Natl. Inst. Stand. Technol.* **101**, 487–503
- [106] Degenhardt C., Nazarova T., Lisdat C., Stoehr H., Sterr U., Riehle F. (2005) Influence of chirped excitation pulses in an optical clock with ultracold calcium atoms. *IEEE Trans. Instrum. Meas.* **54**, 771–775
- [107] Citron M.L., Gray H.R., Gabel C.W., Stroud, Jr. C.R. (1977) Experimental study of power broadening in a two-level atom. *Phys. Rev. A.* **16**, 1507–1512
- [108] Breene R.G. (1961) *The Shift and Shape of Spectral Lines*. Pergamon Press, Oxford, New York
- [109] Breene R.G. (1981) *Theories of Spectral Line Shape*. Wiley, New York
- [110] Dicke R.H. (1954) Coherence in spontaneous radiation processes. *Phys. Rev.* **93**, 99–110
- [111] Mies F.H. (1984) A multichannel quantum defect analysis of diatomic predissociation and inelastic atomic scattering. *J. Chem. Phys.* **80**(6), 2514–2525
- [112] Olivero J.J., Longbothum R.L. (1977) Empirical fits to the Voigt line width: A brief review. *J. Quant. Spectrosc. Radiat. Transfer.* **17**, 233–236
- [113] Nielsen E., Macek J.H. (1999) Low-energy recombination of identical bosons by three-body collisions. *Phys. Rev. Lett.* **83**(8), 1566–1569
- [114] Allard O., Samuelis C., Pashov A., Knöckel H., Tiemann E. (2003) Experimental study of the  $\text{Ca}_2$   $^1\text{S} + ^1\text{S}$  asymptote. *Eur. Phys. J. D.* **26**, 155–164
- [115] Cohen-Tannoudji C., Avan P. (1977) Discrete state coupled to a continuum, continuous transition between the Weisskopf–Wigner exponential decay and the Rabi oscillation. *Colloques Internationaux du C. N. R. S.* **273**, 93–106
- [116] Mackie M., Javanainen J. (2000) Role of Bose enhancement in photoassociation. *J. Mod. Opt.* **47**, 2645–2652

- [117] Zinner G., Binnewies T., Riehle F., Tiemann E. (2000) Photoassociation of cold Ca atoms. *Phys. Rev. Lett.* **85**, 2292–2295
- [118] Porsev S.G., Rakhlina Y.G., Kozlov M.G. (1999) Calculation of hyperfine structure constants for ytterbium. *J. Phys. B: At. Mol. Phys.* **32**, 1113–1120
- [119] Hansen D.P., Mohr J.R., Hemmerich A. (2003) Magnetic trapping of metastable calcium atoms. *Phys. Rev. A.* **67**(2), 021401
- [120] Stellmer S., Tey M.K., Huang B., Grimm R., Schreck F. (2009) Bose-Einstein condensation of Strontium. *Phys. Rev. Lett.* **103**, 200401
- [121] Beverini N., Giammanco F., Maccioni E., Strumia F., Vissani G. (1989) Measurement of the calcium  $^1P_1$ - $^1D_2$  transition rate in a laser-cooled atomic beam. *J. Opt. Soc. Am. B.* **6**, 2188–2193
- [122] Pasternack L., Silver D.M., Yarkony D.R., Dagdigian P.J. (1980) Experimental and theoretical study of the Ca I  $4s3d\ ^1D-4s^2\ ^1S$  and  $4s4p\ ^3P_1-4s^2\ ^1S$  forbidden transitions. *J. Phys. B: At. Mol. Phys.* **13**, 2231–2241
- [123] Drozdowski R., Kwela J., Walkiewicz M. (1993) Lifetimes of the  $4s4p\ ^3P_1$  and  $4s4p\ ^1D_2$  states of Ca I. *Z. Phys. D.* **27**, 321–324
- [124] Porsev S.G., Kozlov M.G., Rakhlina Y.G., Derevianko A. (2001) Many-body calculations of electric-dipole amplitudes for transitions between low-lying levels of Mg, Ca, Sr. *Phys. Rev. A.* **64**, 012508–1–7
- [125] Froese Fischer C., Tachiev G. (2003) Allowed and spin-forbidden electric dipole transitions in Ca I. *Phys. Rev. A.* **68**
- [126] Kurucz R.L., Bell B. (1995) Atomic line data, Kurucz CD-ROM No. 23. Cambridge Mass.: Smithsonian Astrophysical Observatory. typing error of  $A(4s5s\ ^3S - 4s4p\ ^3P)$  has been corrected from the original data
- [127] Cavasso Filho R.L., da Cruz F.C. (2003) A technique to observe “negligible” collision trap losses. *Annals of Optics.* **5**
- [128] Daily J.E., Gommers R., Cummings E.A., Durfee D.S., Bergeson S.D. (2005) Two-photon photoionization of the Ca  $4s3d\ ^1d_2$  level in an optical dipole trap. *Phys. Rev. A.* **71**, 043406–1–5

- 
- [129] Cavasso Filho R.L., Magno W.C., Manoel D.A., Scalabrin A., Pereira D., Cruz F.C. (2003) Deceleration, trapping, and two-photon cooling of calcium atoms. *J. Opt. Soc. Am. B.* **20**, 994–1002
- [130] Derevianko A. (2001) Feasibility of cooling and trapping metastable alkaline-earth atoms. *Phys. Rev. Lett.* **87**, 023002–1–4
- [131] Martinez de Escobar Y.N., Mickelson P.G., Pellegrini P., Nagel S.B., Traverso A., Yan M., Côté R., Killian T.C. (2008) Two-photon photoassociative spectroscopy of ultracold  $^{88}\text{Sr}$ . *Phys. Rev. A.* **78**, 062708
- [132] Kitagawa M., Enomoto K., Kasa K., Takahashi Y., Ciuryło R., Naidon P., Julienne P.S. (2008) Two-color photoassociation spectroscopy of ytterbium atoms and the precise determinations of s-wave scattering lengths. *Phys. Rev. A.* **77**, 012719

# Publications

## Conference contributions

- Max Kahmann, Evgenij Pachomow, Eberhard Tiemann, Uwe Sterr and Fritz Riehle  
*Ultra stable laser system for two color photoassociation of Ca*  
Deutsche physikalische Gesellschaft Frühjahrstagung, Berlin (poster) 2014
- Evgenij Pachomow, Max Kahmann, Uwe Sterr, Fritz Riehle and Eberhard Tiemann  
*Towards optical Feshbach resonances with  $^{40}\text{Ca}$*   
Deutsche physikalische Gesellschaft Frühjahrstagung, Berlin (talk) 2014
- Evgenij Pachomow, Max Kahmann, Uwe Sterr, Fritz Riehle and Eberhard Tiemann  
*Narrow line photoassociation in Calcium and its application for Rabi oscillations between atomic and molecular condensates* Research training group 1729 workshop, Lüneburg
- Max Kahmann, Eberhard Tiemann, Evgenij Pachomow, Uwe Sterr and Fritz Riehle  
*Photoassociation spectroscopy of ultracold  $^{40}\text{Ca}$  near the  $^1S_0 + ^3P_1$  asymptote*  
Division seminar University of Torun (talk) 2014

- Max Kahmann, Eberhard Tiemann, Evgenij Pachomow, Uwe Sterr and Fritz Riehle  
*Optical Feshbach resonances in  $^{40}\text{Ca}$*   
Group meeting university of Torun (talk) 2014
- Evgenij Pachomow, Max Kahmann, Eberhard Tiemann, Uwe Sterr and Fritz Riehle  
*Applications of optical Feshbach resonances in  $^{40}\text{Ca}$*   
Division PhD meeting PTB, Braunschweig (talk) 2014
- Max Kahmann, Eberhard Tiemann, Evgenij Pachomow, Uwe Sterr and Fritz Riehle  
*Photoassociation spectroscopy towards optical Feshbach resonances in  $^{40}\text{Ca}$*   
Division PhD meeting PTB, Braunschweig (talk) 2014
- Max Kahmann, Eberhard Tiemann, Evgenij Pachomow, Uwe Sterr and Fritz Riehle  
*Photoassociation spectroscopy at the  $^1S_0 + ^3P_1$  asymptote in  $^{40}\text{Ca}$*   
Division PhD meeting PTB, Braunschweig (poster) 2014
- Evgenij Pachomow, Max Kahmann, Uwe Sterr, Fritz Riehle and Eberhard Tiemann  
*Towards optical Feshbach resonances with  $^{40}\text{Ca}$*   
Research training group 1729 seminar, Hannover (talk) 2013
- Max Kahmann, Evgenij Pachomow, Eberhard Tiemann, Fritz Riehle and Uwe Sterr  
*Optical Feshbach Resonances with Calcium at the  $^1S_0 + ^3P_1$  Asymptote*  
Research training group 1729 workshop, Visselhövede (poster) 2013
- Evgenij Pachomow, Max Kahmann, Eberhard Tiemann, Fritz Riehle and Uwe Sterr  
*Photoassociation of Ultracold Calcium at the  $^1S_0 + ^3P_1$  Asymptote*  
Research training group 1729 workshop, Visselhövede (poster) 2013
- Max Kahmann, Oliver Appel, Evgenij Pachomow, Fritz Riehle and Uwe Sterr  
*Enhanced magneto-optical trapping by storing atoms in a dark triplet*  
Research training group 1729 workshop, Goslar (talk) 2013

- Max Kahmann, Oliver Appel, Eberhard Tiemann, Fritz Riehle and Uwe Sterr  
*Photoassociation near the intercombination line of  $^{40}\text{Ca}$*   
Deutsche physikalische Gesellschaft Frühjahrstagung, Hannover (talk) 2013
- Max Kahmann, Oliver Appel, Eberhard Tiemann, Fritz Riehle and Uwe Sterr  
*Photoassociation near the intercombination line of  $^{40}\text{Ca}$*   
Group seminar, Hannover (talk) 2013
- Uwe Sterr, Max Kahmann, Oliver Appel, Eberhard Tiemann and Fritz Riehle  
*Photoassociation of Ultracold Calcium at the  $^1S_0 + ^3P_1$  Asymptote*  
International Conference on Laser Spectroscopy, Berkeley (poster) 2013
- Fritz Riehle, Max Kahmann, Oliver Appel, Uwe Sterr and Eberhard Tiemann  
*Photoassociation of Ultracold Calcium at the  $^1S_0 + ^3P_1$  Asymptote*  
Modern Problems of Laser Physics, Novosibirsk (talk) 2013
- Evgenij Pachomow, Max Kahmann, Oliver Appel, Fritz Riehle, Uwe Sterr and Eberhard Tiemann  
*Photoassociation of Ultracold Calcium at the  $^1S_0 + ^3P_1$  Asymptote*  
Young atom opticians conference, Birmingham (poster) 2013
- Max Kahmann, Oliver Appel, Evgenij Pachomow, Fritz Riehle and Uwe Sterr  
*Optical Feshbach Resonances with  $^{40}\text{Ca}$*   
Atomic physics seminar, Oberjoch (talk) 2013
- Max Kahmann, Oliver Appel, Evgenij Pachomow, Fritz Riehle and Uwe Sterr  
*Optical Feshbach Resonances with  $^{40}\text{Ca}$*   
Optical clock seminar, Braunschweig (talk) 2013
- Max Kahmann, Oliver Appel, Sebastian Kraft, Dennis Le Plat, Fritz Riehle and Uwe Sterr  
*Enhanced Loading for Ultracold Calcium Atoms and Photoassociation at the  $^1S_0 + ^3P_1$  Asymptote*  
Deutsche physikalische Gesellschaft Frühjahrstagung, Stuttgart (poster) 2012
- Max Kahmann, Oliver Appel, Fritz Riehle and Uwe Sterr  
*Optical Feshbach Resonances with  $^{40}\text{Ca}$*   
Research training group 1729 seminar, Hannover (talk) 2012

- Max Kahmann, Oliver Appel, Sebastian Kraft, Fritz Riehle and Uwe Sterr  
*Photoassociation with  $^{40}\text{Ca}$*   
Atomic physics seminar, Oberjoch (talk) 2012
- Max Kahmann, Oliver Appel, Fritz Riehle and Uwe Sterr  
*Photoassociation of Ultracold Calcium at the  $^1S_0 + ^3P_1$  Asymptote*  
National institute of Information and Communications Technology, Tokio (poster) 2012
- Max Kahmann, Oliver Appel, Stephan Schulz, Sebastian Kraft, Fritz Riehle and Uwe Sterr  
*Investigation of light-assisted collisions of  $^{40}\text{Ca}$*   
Young atom opticians conference, Hannover (poster) 2011
- Max Kahmann, Oliver Appel, Stephan Schulz, Sebastian Kraft, Fritz Riehle and Uwe Sterr  
*Investigation of light-assisted collisions of  $^{40}\text{Ca}$*   
School of advanced science Sao Paulo (poster) 2011
- Oliver Appel, Max Kahmann, Stephan Schulz, Sebastian Kraft, Fritz Riehle and Uwe Sterr  
*Investigation of light-assisted collisions of  $^{40}\text{Ca}$*   
Deutsche physikalische Gesellschaft school Bad Honnef (poster) 2011
- Oliver Appel, Max Kahmann, Stephan Schulz, Sebastian Kraft, Fritz Riehle and Uwe Sterr  
*Investigation of light-assisted collisions of  $^{40}\text{Ca}$*   
Deutsche physikalische Gesellschaft Frühjahrstagung, Dresden (poster) 2011
- Sebastian Kraft, Oliver Appel, Max Kahmann, Stephan Schulz, Fritz Riehle and Uwe Sterr  
*Investigation of light-assisted collisions of  $^{40}\text{Ca}$*   
International Conference on Laser Spectroscopy, Hannover (poster) 2011
- Max Kahmann, Sebastian Kraft, Oliver Appel, Stephan Schulz, Fritz Riehle and Uwe Sterr  
*Using the metastable  $^3P_0$ -state in a BEC of  $^{40}\text{Ca}$*   
École de physique, Les Houches (poster) 2010

- Sebastian Kraft, Felix Vogt, Oliver Appel, Stephan Schulz, Max Kahmann, Uwe Sterr and Fritz Riehle  
*A Bose-Einstein condensate of Calcium*  
International Conference on Laser Spectroscopy, Cairns (poster) 2010
- Helge Hattermann, Florian Jessen, Brian Kasch, Daniel Cano, Max Kahmann, Dieter Koelle, Reinhold Kleiner and József Fortágh  
*Cold atoms near superconductors*  
Deutsche physikalische Gesellschaft Frühjahrstagung, Hannover (talk) 2010
- Florian Jessen, Daniel Cano, Helge Hattermann, Max Kahmann, Dieter Koelle, Reinhold Kleiner and József Fortágh  
*Ultracold Atoms near Superconductors*  
Deutsche physikalische Gesellschaft Frühjahrstagung, Hannover (poster) 2010
- Helge Hattermann, Daniel Cano, Brian Kasch, Florian Jessen, Max Kahmann, Dieter Koelle, Reinhold Kleiner and József Fortágh  
*Ultra-Cold Atoms in Superconducting Microtraps*  
Deutsche physikalische Gesellschaft Frühjahrstagung, Hamburg (talk) 2009
- Florian Jessen, Daniel Cano, Helge Hattermann, Max Kahmann, Dieter Koelle, Reinhold Kleiner and József Fortágh  
*Superconducting Microtraps for Cold Atom Experiments*  
Deutsche physikalische Gesellschaft Frühjahrstagung, Hamburg (poster) 2009

## Referred publications

- Max Kahmann, Eberhard Tiemann, Oliver Appel, Uwe Sterr and Fritz Riehle  
*Photoassociation of  $^{40}\text{Ca}$  near the  $^3P_1 + ^1S_0$  asymptote with kHz uncertainty and its Zeeman effect*  
Phys. Rev. A (2014)

## Not yet published

- Max Kahmann and Uwe Sterr  
*Enhanced magneto-optical trapping of  $^{40}\text{Ca}$*   
To be published (article) 2014
- Max Kahmann, Eberhard Tiemann, Oliver Appel, Uwe Sterr, and Fritz Riehle  
*Nonlinear Zeeman effect in photoassociation spectra of  $^{40}\text{Ca}$  near the  $^3P_1 + ^1S_0$  asymptote*  
To be published (article) 2014





# Danksagung

An dieser Stelle möchte ich all Jenen danken, welche mich bei dieser Arbeit unterstützt haben:

Den Herren Prof. (h.c.) Dr. habil. Fritz Riehle und Dr. Uwe Sterr möchte ich für die Unterstützung und Betreuung von Seiten der PTB in Braunschweig danken. Herrn Dr. Uwe Sterr insbesondere dafür, dass er sich stets Zeit nahm, die er eigentlich gar nicht hatte und Herrn Dr. Fritz Riehle für die konstruktiven Besprechungen inklusive unterhaltsamer Frotzeleien.

Herrn Prof. Dr. Eberhard Tiemann danke ich für die Betreuung von Seiten der Universität Hannover als mein Doktorvater. Die Gespräche mit ihm waren stets sehr lehrreich und angenehm. Auch möchte ich ihm für die theoretische Unterstützung durch seine Modelle und Simulationen danken, welche diese Arbeit und die gemeinsame Publikation in dieser Form überhaupt erst ermöglichten.

Herrn Dr. habil. Carsten Klempt danke ich für seine Betreuung im Rahmen seiner Eigenschaft als mein Mentor im Zuge des Graduiertenkollegs. Seine unabhängigen Einschätzungen von Ausserhalb waren mir stets willkommen.

Herrn Dr. Oliver Appel danke ich für die Einarbeitung in das Labor, die erfolgreiche Zusammenarbeit in selbigem und kurzweilige Momente beim Sport und auf den virtuellen Schlachtfeldern.

Den übrigen Wissenschaftlern, die sich während meiner Zeit in Braunschweig in das Kalziumexperiment einbrachten: Herrn Dr. Sebastian Kraft, Herrn Dr. Stefan Schulz, Herrn Dr. Felix Vogt sowie meinem Nachfolger Herrn Dipl. Phys. Evgenij Pachomov, dem ich das Kalziumexperiment anempfehle und weiterhin viel Erfolg wünsche.

Meinen promovierenden Mitstreitern, Herrn Dipl. Phys. Stefan Vogt, Herrn Dr. Christian Hagemann, Herrn M.Eng. Sebastian Häffner, Herrn Dipl. Phys. Ali Al-Masoudi und Herrn Dr. Thomas Middelman für konstruktive Gespräche im Club der Denker, sowie regelmäßigen Austausch wissenschaftlicher und privater Natur.

Meinem braunschweiger Molekülkompetenzteam Herrn Dr. habil. Christian Lisdat und Herrn Dr. Stephan Falke. Herrn Dr. Lisdat darüber hinaus für das Bergsteigen in der Schweiz und Herrn Dr. Falke für die Beantwortung aller Fragen jenseits des Horizontes meiner Besoldungsstufe nachdem dem Kalziumexperiment die Post-Docs verlustig gingen.

Allen aktiven und ehemaligen Wissenschaftlichen Mitarbeitern der Arbeitsgruppen 4.31, 4.32 und 4.33, Frau Dr. Gesine Grosche, Herrn Dr. Harald Schnatz, Herrn Dr. Christian Grebing, Herrn Dr. Stefan Raupach, Herrn Dr. Thomas Legero und Herrn Dr. Thomas Kessler für hilfreiche Gespräche, ein nettes Arbeitsklima und Kuchen. Herr Dr. Sören Darscha im Besonderen für sein penibles Korrekturlesen, das der Arbeit den letzten Schliff gab.

Den Herren Klemens Budin, Jörn Falke und Andre Uhde für ihre Unterstützung in allen technischen Fragen und Arbeiten sowie nette Gespräche. Herrn Budin insbesondere für die Kafferunden mit Frau Izabela Batus und den Herren Falke und Uhde insbesondere für die gelungenen Doktorhüte.

Den Herrn Dipl. Ing. Andreas Koczvara und Herrn Dipl. Ing. Matthias Misera sowie Frau Marion Wengel für die rat- und tatkräftige Unterstützung in allen Fragen der Elektronik.

Pan Prof. Dr. Roman Ciurylo i Pan Fiz. Dipl. Mateusz Borkowski chciał bym podziękować za gościnność moja w Toruniu i owocne rozmowy. Szczególnie dziękuje panu Mateuszowi Borkowski za wsparcie mojej pracy przez jego teoretyczne rachunki.

Frau Birgit Voss und Frau Herrmann für ihre Unterstützung aller Formalien innerhalb der PTB inklusive Goldeinkäufe.

Frau Saskia Henninger und Frau Ohlendorf für ihre formale Unterstützung von Seiten der QUEST Leibniz Forschungsschule und des Graduiertenkollegs.

Herrn Markus Bergthaler für seine sprachliche Unterstützung beim schreiben der Einleitung.

Meiner Cousine Frau Hendrike Racky nebst Familie für die netten Besuche in Kassel, die untrennbar mit meiner Braunschweiger Zeit und damit meiner Doktorarbeit Verbunden sind.

Jedem der erwartet hätte erwähnt zu werden, sich bisher nicht gefunden hat und dem damit diese Zeile gewidmet ist.

Meinen Eltern für die Ermöglichung meines Studiums und die Unterstützung in jedweder Hinsicht während der Promotion.

Meiner Partnerin Jenny Mucha für ihre Unterstützung während des obligatorischen Doktorandenkollers und dem Wahnsinn der Bewerbungsphase, ihr Mitleiden und Mitfreuen und ihre liebenswerte Art.

Diese Arbeit wurde gefördert durch QUEST (Quantum engineering for space- and time-research) und RTG 1729 (Fundamentals and applications of ultra-cold matter).